6. Reynolds momentum flux and kinetic energy

6.1 Introduction

In turbulent flows the Reynolds momentum flux distribution gives important information on the momentum and mass transfers and, thus, on the sediment transport process. A further important element, in the analysis on flow characteristics inside the scour hole, is the distribution of the turbulent energy budget of flow. In fact, as it is known, the potential energy of flow is converted into flow kinetic energy and the kinetic energy is converted into turbulent kinetic energy. The energy conversion and exchange at different channel sections are strictly related to sediment erosion, transport and deposition processes.In order to analyze the distributions of the Reynolds momentum flux and of the turbulent kinetic energy inside the scour hole, developed in the examined case, the instantaneous turbulent fluctuation components have been estimated, in each measurement point, as deviations from the corresponding time-averaged velocity component:

$$u_i'(t) = u_i(t) - U_i \,,\ i = x,\, y,\, z\,; \tag{6.1}$$

6.2 Reynolds momentum flux

Then the components of the Reynolds momentum flux $\overline{u_i'u_j'}$ have been estimated as:

$$\overline{u_i'u_j'} = \overline{u_i'(t)\,u_j'(t)} = \frac{1}{T}\sum_{t=1}^{T}\left[u_i'(t)\ u_j'(t)\right];\quad i, j = x, y, z \tag{6.2}$$

where T is the measurement time length.

– *Reynolds momentum flux* $\overline{u_x'u_x'}$

The contour plots of the Reynolds momentum flux $\overline{u_x'u_x'}$ in each considered sections inside the scour hole are reported in Figure 6.1. At section X0 (see Figure 6.1a) high

values of $\overline{u_x' u_x'}$ occur near the bed at the channel axis (Y = 20cm). At section X5 $\overline{u_x' u_x'}$ increases in value in the right bank region. At section X10 it begins to increase at the left bank region. In sections X15 and X20 high values of $\overline{u_x' u_x'}$ are found in the near bank regions (up to 0.2m^2/s^2). For X > X25 (Figure 6.1b) $\overline{u_x' u_x'}$ starts to decrease in the left and right bank regions, but it increases at the channel axis. For X30 < X < X50 (Figure 6.1c), the Reynolds momentum flux assumes very high values (up to 2.2m^2/s^2) at the channel axis (Y = 20cm). The horizontal contour maps of the Reynolds momentum flux component $\overline{u_x' u_x'}$ for different values of Z are also reported in Figure 6.2. These distributions confirm that high values of $\overline{u_x' u_x'}$ are near the bed inside the scour hole; for X > X30 the highest values of $\overline{u_x' u_x'}$ are found at the central region (18cm < Y < 28cm). Figure 6.3 reports the longitudinal contour maps of the Reynolds momentum flux component $\overline{u_x' u_x'}$. Near the banks (Y < 18cm and Y > 28cm) it can be observed that inside the scour hole (X < X30), $\overline{u_x' u_x'}$ assumes high values near the bed. For X > X30, where deposition occurs, high values of $\overline{u_x' u_x'}$ occur in whole water depth. Thus, as Figure 6.3a shows (at Y = 5 cm), the higher values of the momentum flux moves from the bed, inside the scour hole, towards the free surface, downstream of the scour hole. In Figure 6.3b it can be observed that approaching to the channel axis, for 18cm < Y < 22cm (see Figures 6.3c-d), high values of $\overline{u_x' u_x'}$ are found also near the bed, downstream of the deposition zone (X >X40). Moreover, the high values observed near the bed downstream of the deposition zone (X >X40) are greater than those observed into the scour hole (X < X30). Moving toward the left bank (28cm < Y < 36cm) the pattern of the Reynolds momentum flux is similar to that observed near the right bank (Y < 14cm, see Figures 6.3a-b).

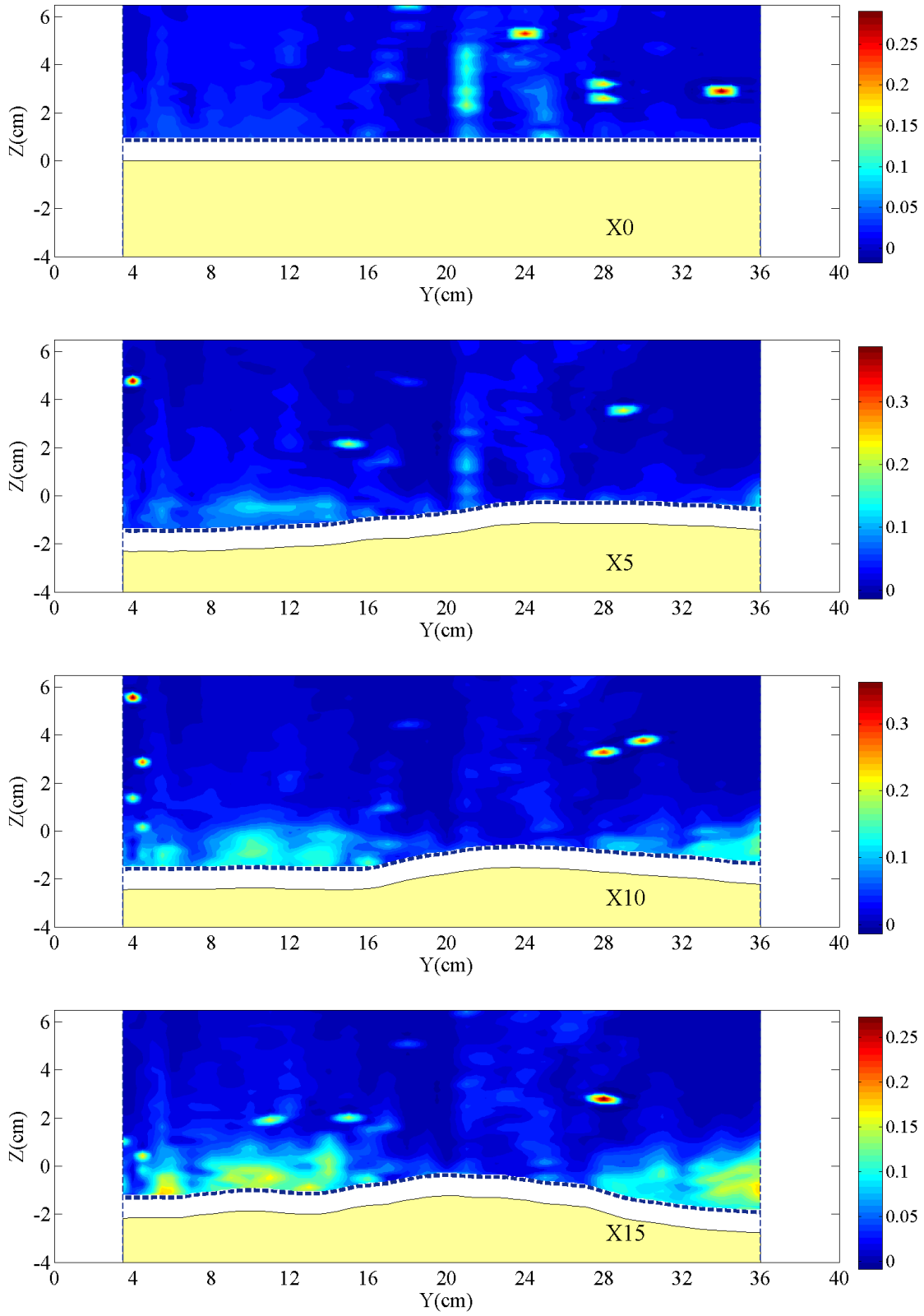

Figure 6.1 – Contour maps of $\overline{u'_x u'_x}$ (m^2/s^2): a) X0 < X < X15.

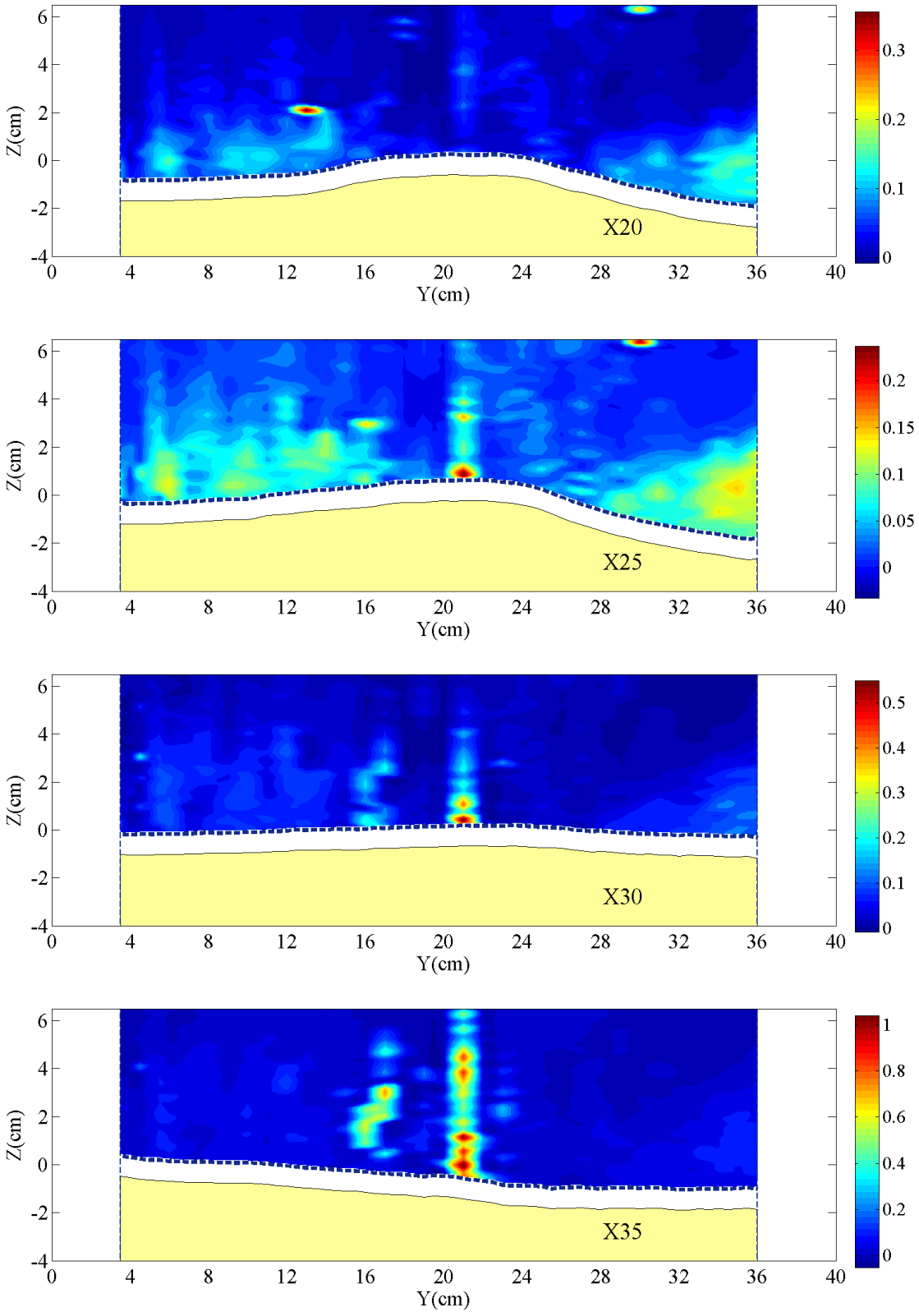

Figure 6.1 – Contour maps of $\overline{u_x' u_x'}$ (m^2/s^2): b) X20 < X < X35.

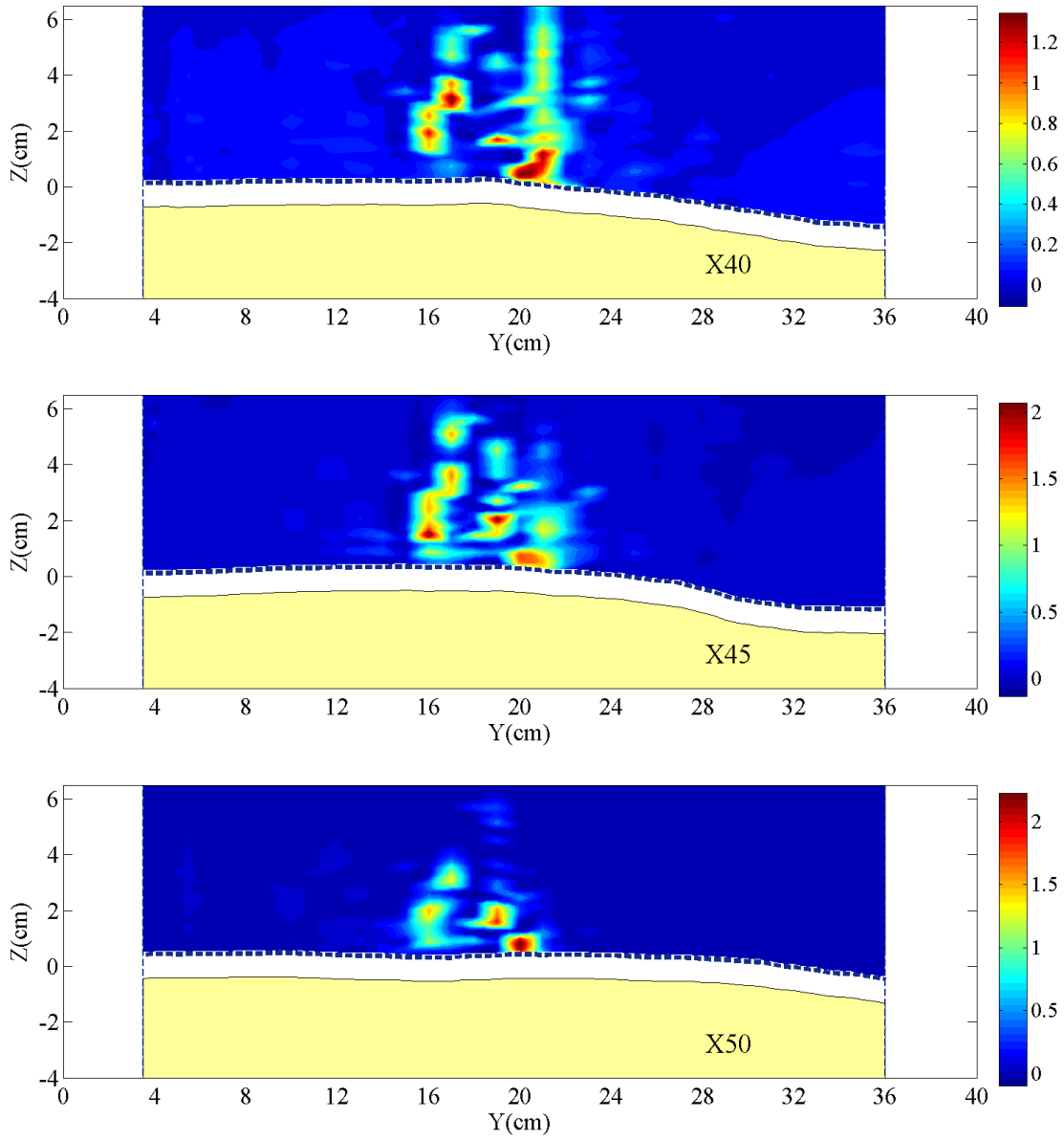

Figure 6.1 – Contour maps of $\overline{u_x' u_x'}$ (m^2/s^2): c) X40 < X < X50.

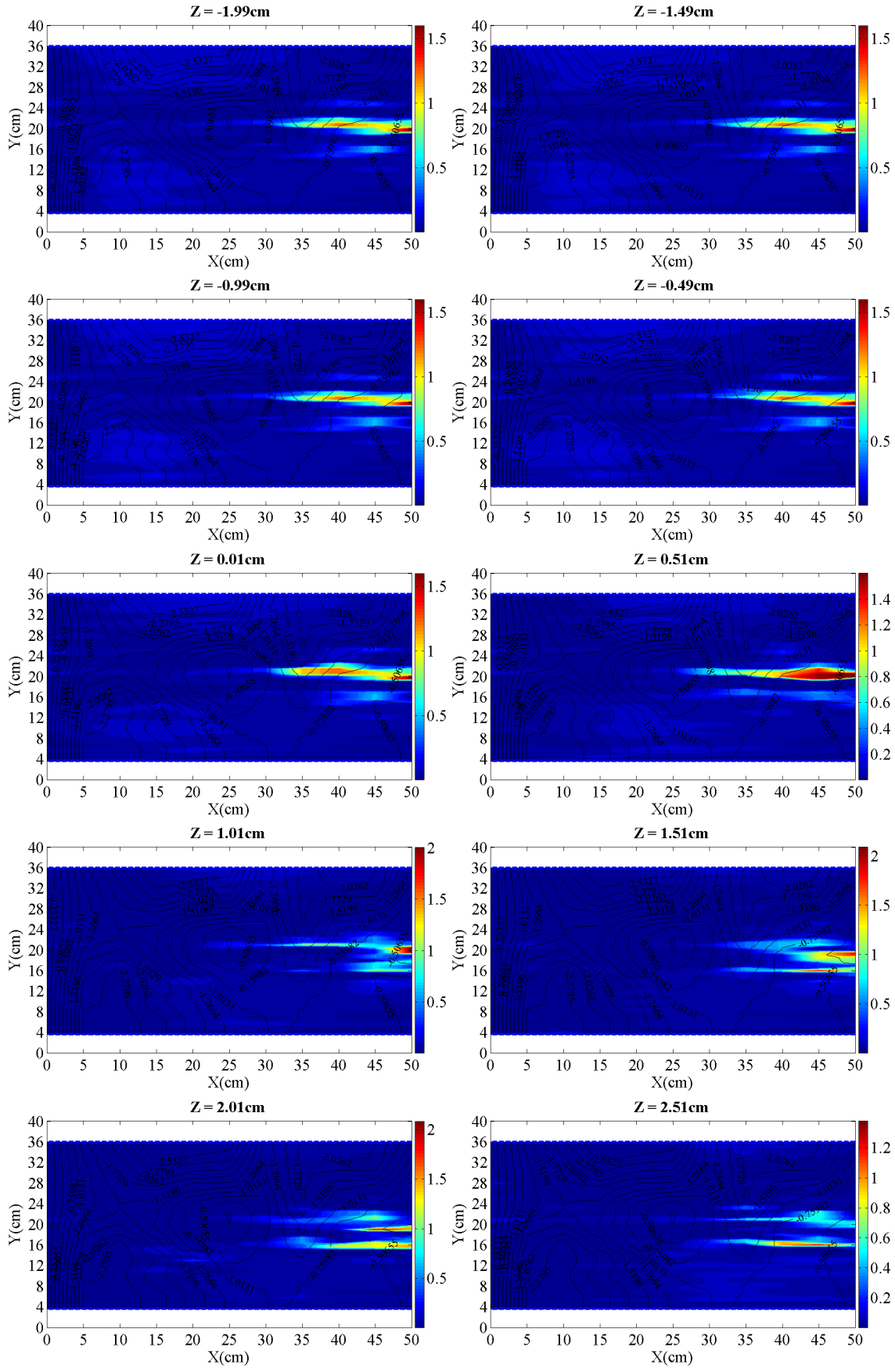

Figure 6.2 – Horizontal contour maps of $\overline{u_x' u_x'}$ (m^2/s^2): a) -1.99cm < Z < 2.51cm.

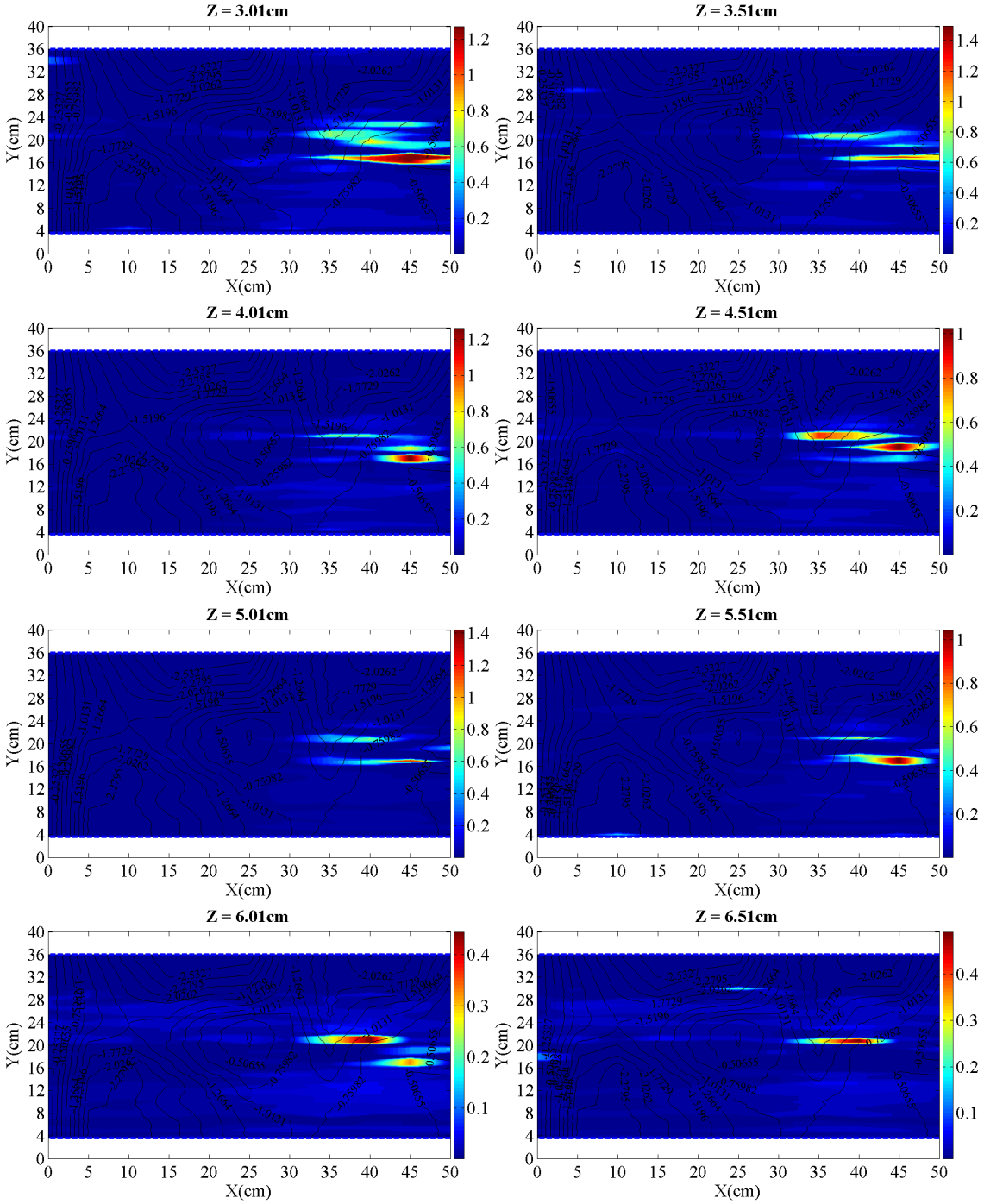

Figure 6.2 – Horizontal contour maps of $\overline{u_x' u_x'}$ (m^2/s^2): b) 3.01cm < Z < 6.51cm.

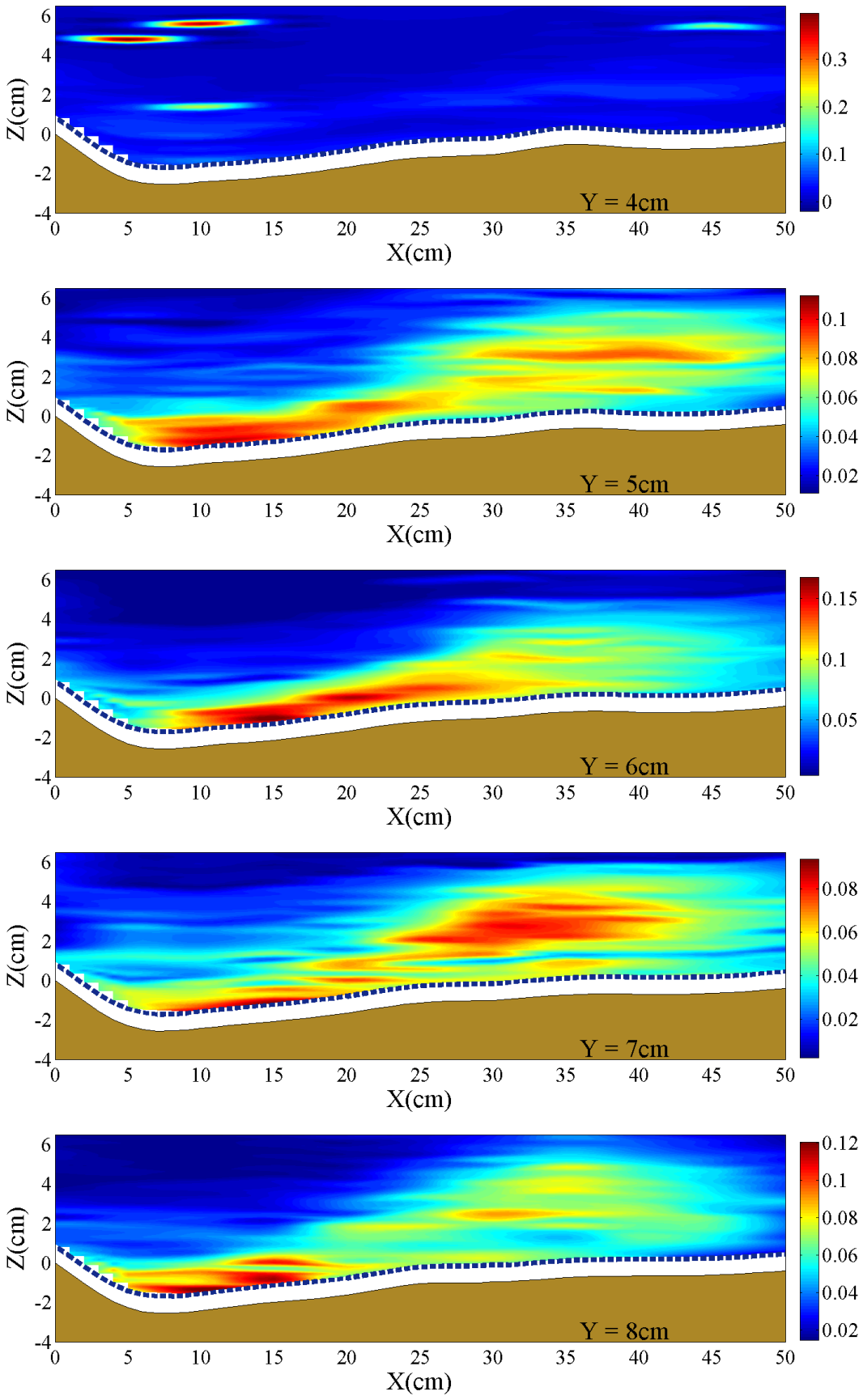

Figure 6.3 – Longitudinal contour maps of $\overline{u_x' u_x'}$ (m^2/s^2): a) 4cm < Y < 8cm.

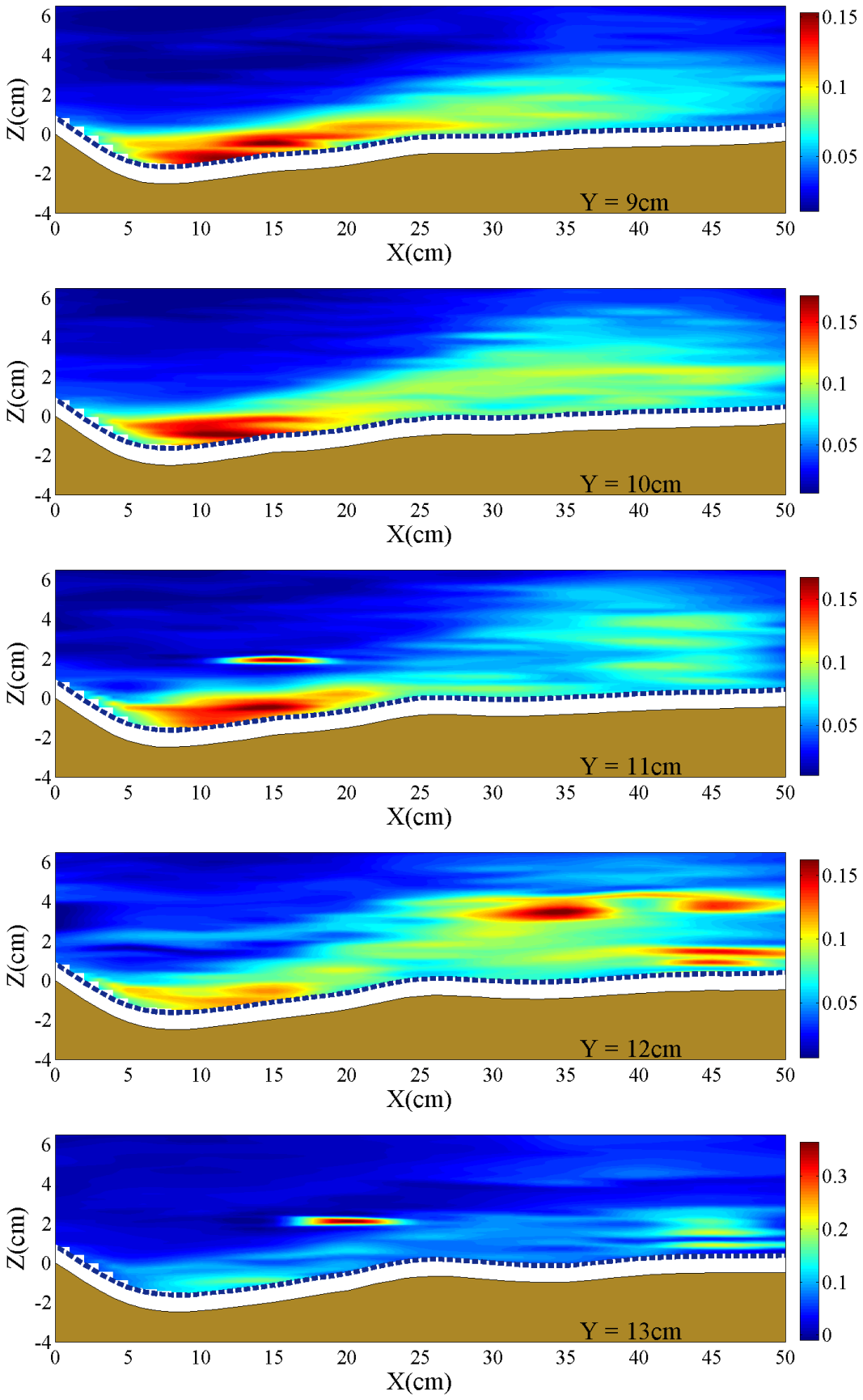

Figure 6.3 – Longitudinal contour maps of $\overline{u_x' u_x'}$ (m^2/s^2): b) 9cm < Y < 13cm.

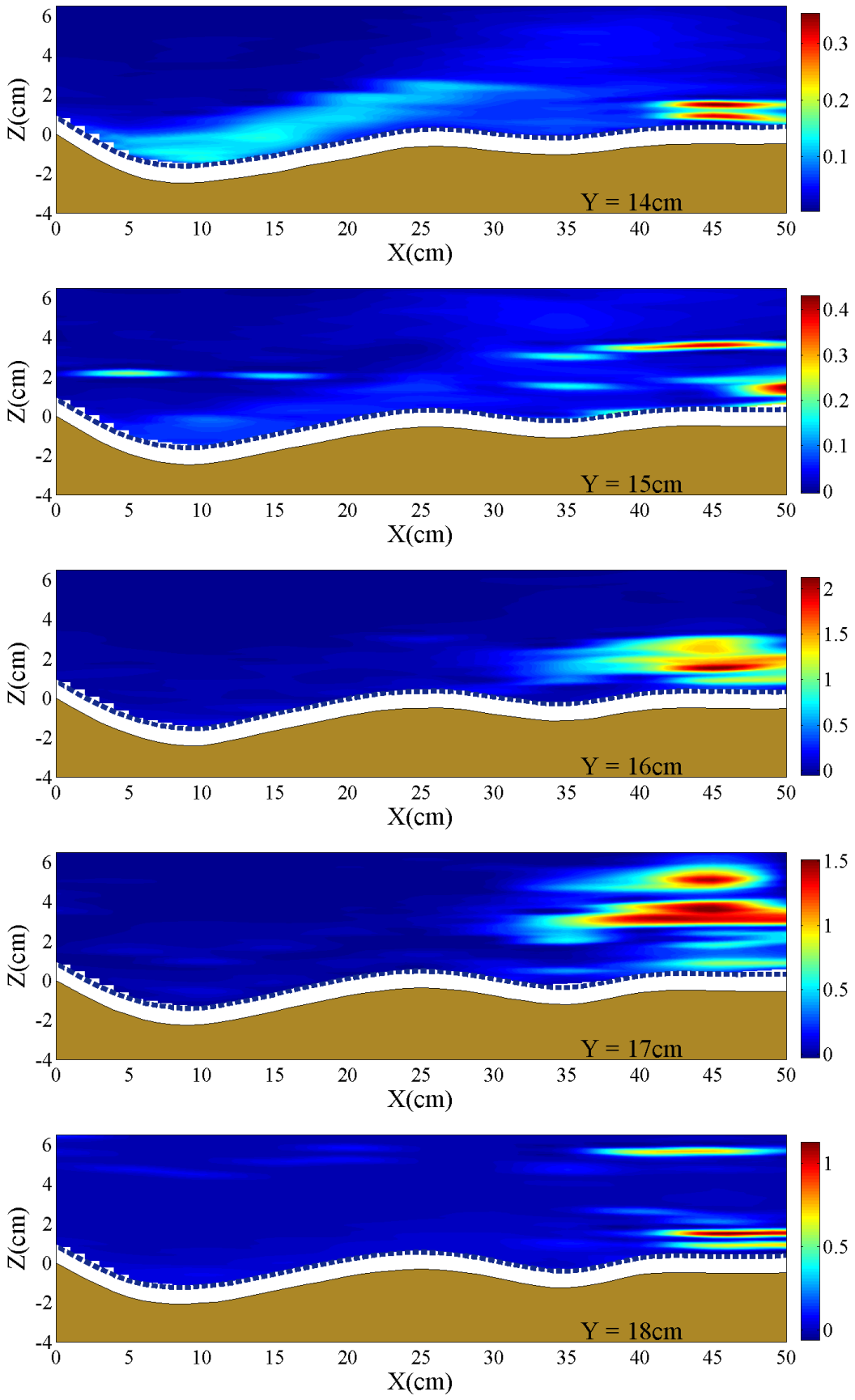

Figure 6.3 – Longitudinal contour maps of $\overline{u_x' u_x'}$ (m^2/s^2): c) 14cm < Y < 18cm.

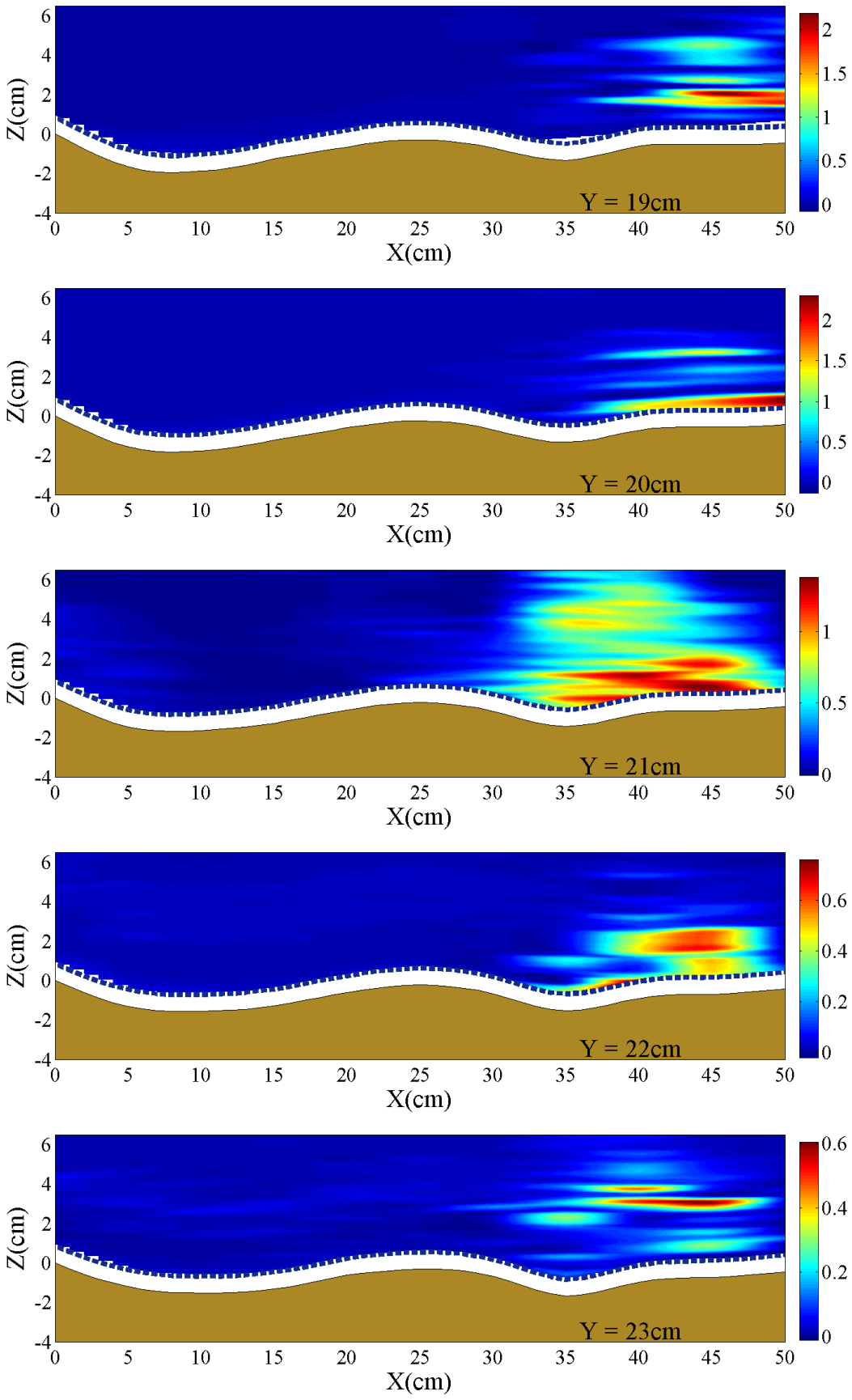

Figure 6.3 – Longitudinal contour maps of $\overline{u_x' u_x'}$ (m^2/s^2): d) 19cm < Y < 23cm.

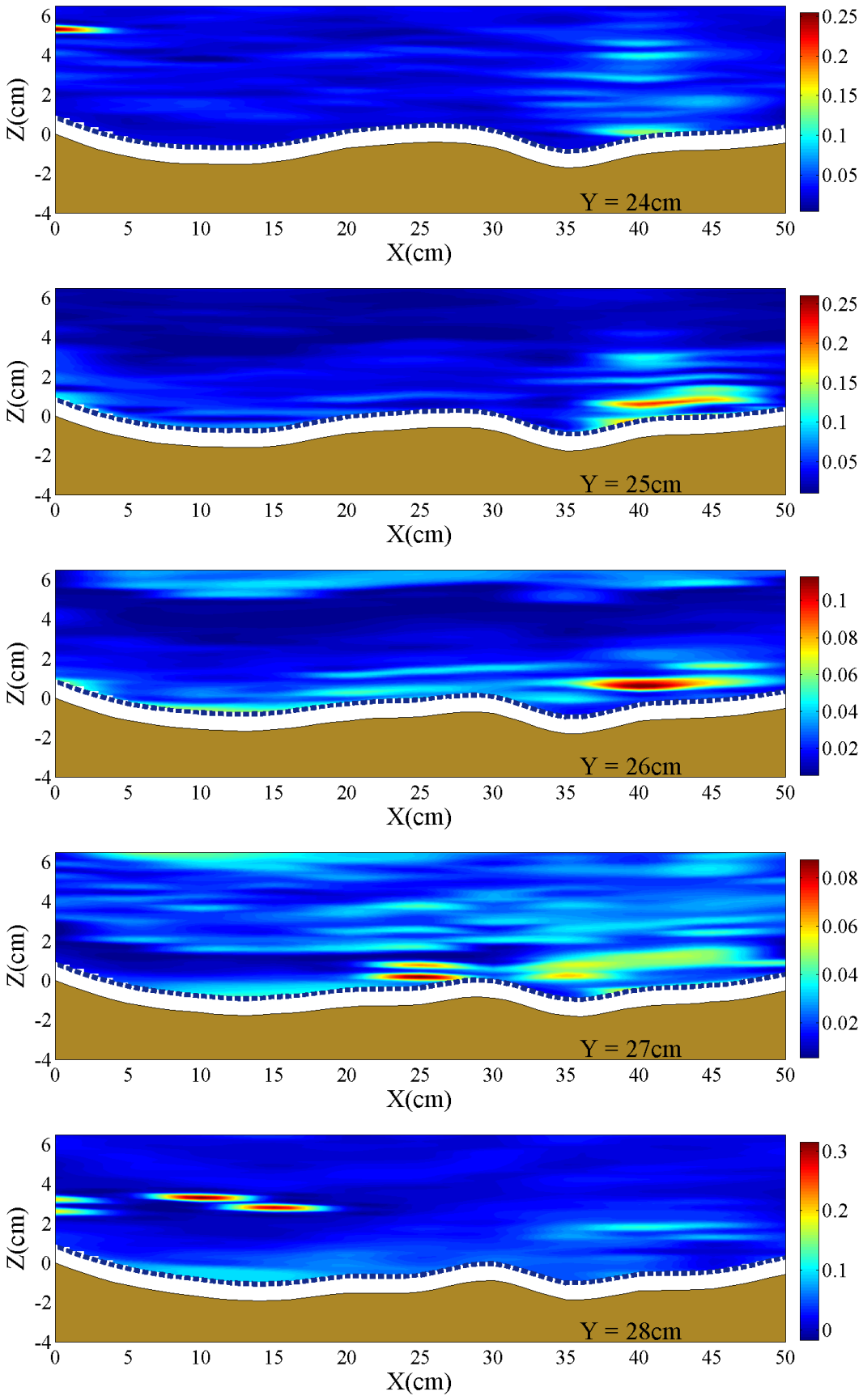

Figure 6.3 – Longitudinal contour maps of $\overline{u_x' u_x'}$ (m^2/s^2): e) 24cm < Y < 28cm.

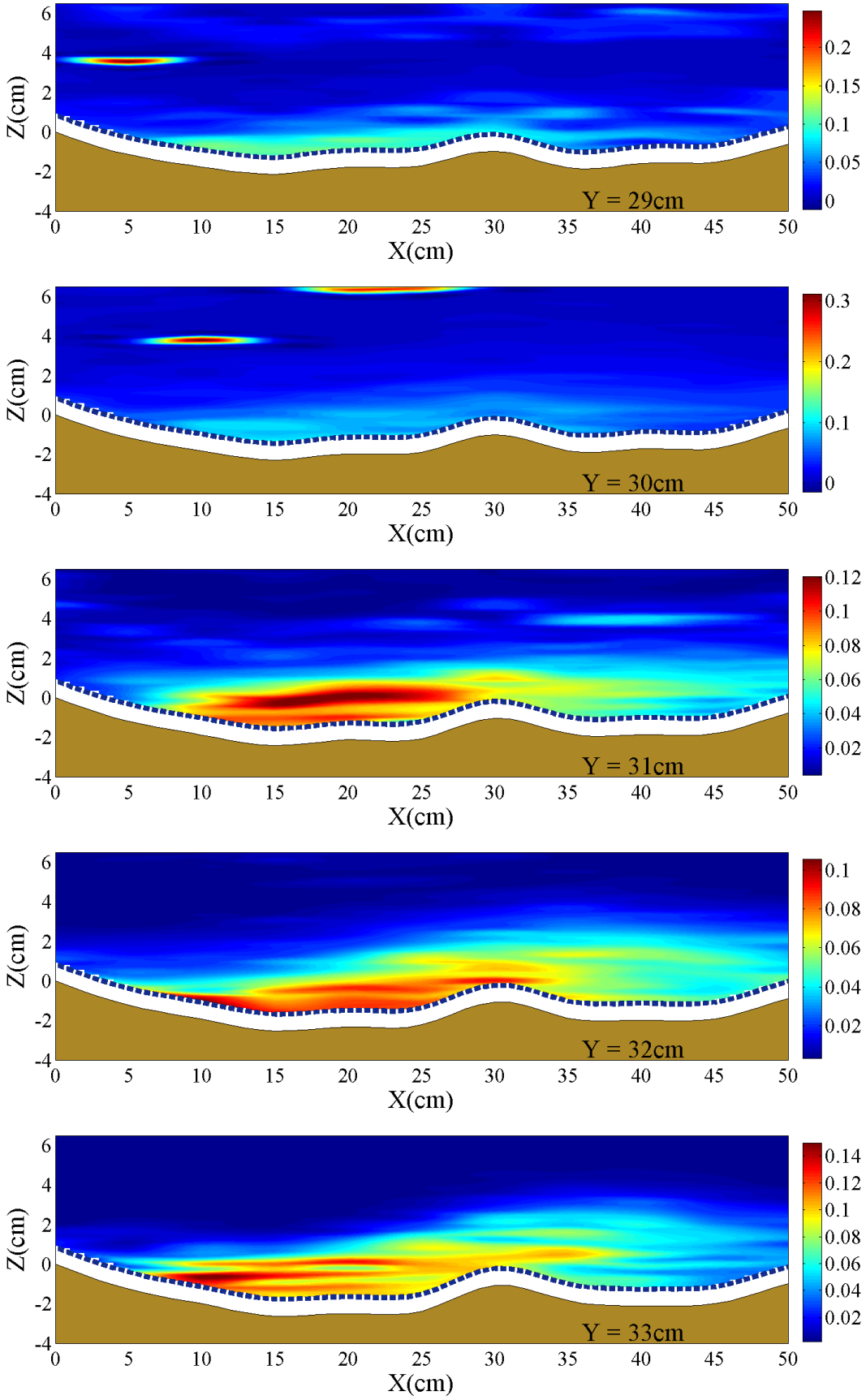

Figure 6.3 – Longitudinal contour maps of $\overline{u_x' u_x'}$ (m^2/s^2): f) 29cm < Y < 33cm.

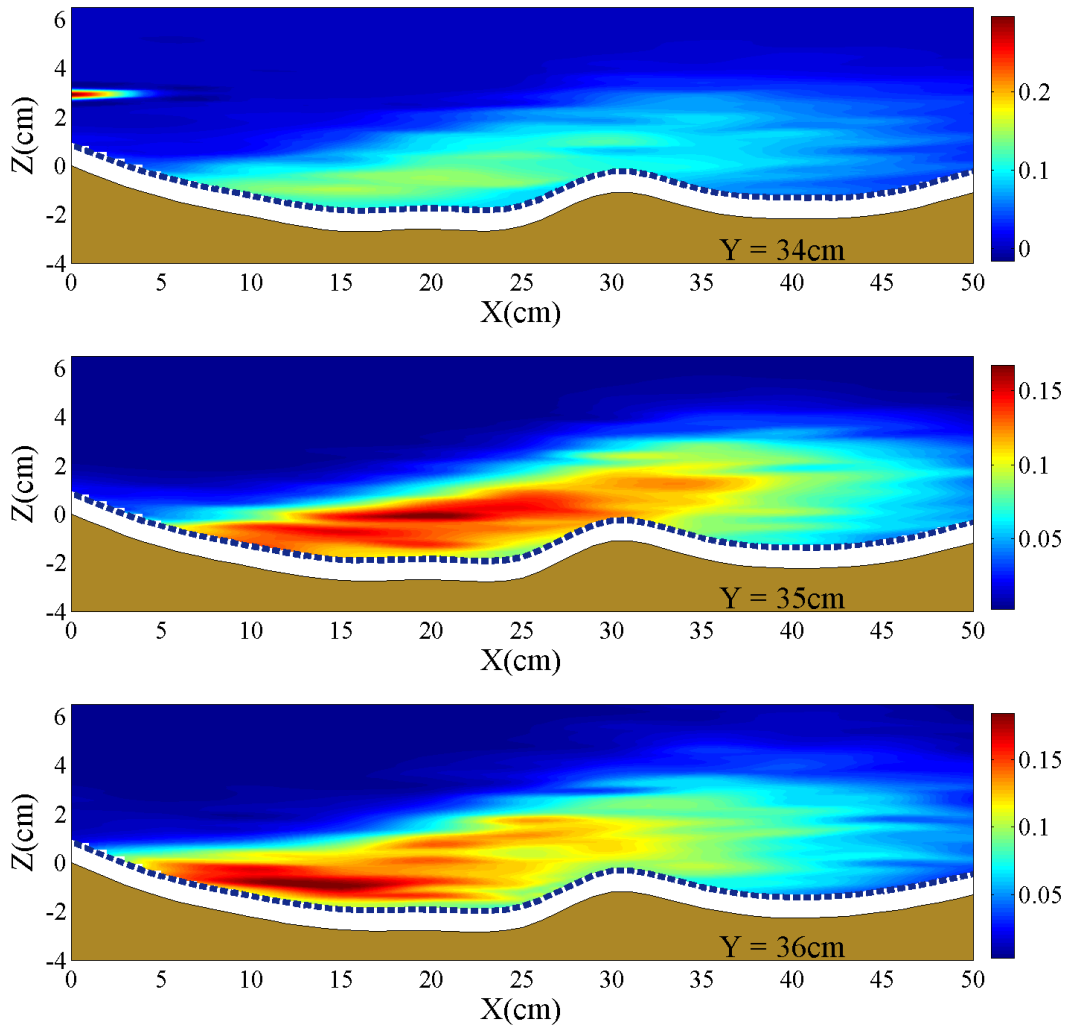

Figure 6.3 – Longitudinal contour maps of $\overline{u'_x u'_x}$ (m^2/s^2): g) 34cm < Y < 36cm.

- *Reynolds momentum flux* $\overline{u'_y u'_y}$

Figure 6.4 reports the contour maps of the Reynolds momentum flux component $\overline{u'_y u'_y}$ in each of the examined sections. In Figure 6.4a it can be observed that for X ≤ X15, $\overline{u'_y u'_y}$ assumes high values near the free surface and in the left bank region. Particularly, in sections X0 and X10 the highest value of $\overline{u'_y u'_y}$ is of about $0.3 m^2/s^2$, but in section X15 the values are one order of magnitude smaller ($0.06 m^2/s^2$). Moving downstream (at section X35, see Figure 6.4b) the high value of $\overline{u'_y u'_y}$ moves toward the central region (15cm < Y

< 25cm). At sections X40 and X45 (see Figure 6.4c) there are no evident peak values of the momentum flux component $\overline{u'_y u'_y}$, but high values of $\overline{u'_y u'_y}$ (of ~$1 \cdot 10^{-3}$ m^2/s^2) occur near the bed for almost the whole section. At section X50 the higher value of $\overline{u'_y u'_y}$ seems to move towards the left bank region (Y > 25cm).

In Figure 6.5 the horizontal distribution of $\overline{u'_y u'_y}$ confirms the velocity pattern previously examined. In particular, it can be observed that, near the bed (Z < 1cm see Figure 5.21a) the highest values of $\overline{u'_y u'_y}$ occur for X < 35cm, in the near-bank regions (4cm < Y < 18cm and 28cm <Y < 36cm); for X > X40 the highest values of momentum flux are found in the central region. From Figure 6.5b it can be observed that $\overline{u'_y u'_y}$ assumes high values near the free surface, for X < X15, and close to the left bank, for Y < 25cm.

The longitudinal distributions of the Reynolds momentum flux component $\overline{u'_y u'_y}$, shown in Figure 6.6, highlight that, generally, the momentum flux $\overline{u'_y u'_y}$ assumes high values both near the bed and near the free surface. For Y < 18cm, the higher values of $\overline{u'_y u'_y}$ (~$2.3 \cdot 10^{-3}$ m^2/s^2) are found near the bed especially for X0 < X < X10 and near the free surface especially for X25 < X < X35. The region with high values of $\overline{u'_y u'_y}$ increases its dimension moving towards the channel axis (see Figures 6.6b-d), assuming its greatest dimension and intensity ($5 \cdot 10^{-3}$ m^2/s^2) at Y = 16 cm. Furthermore, into the central region, high values of $\overline{u'_y u'_y}$ occur in the scour hole at section X10. For Y > 24cm (see Figures 6.6e-g), $\overline{u'_y u'_y}$ assumes high values in the scour hole for X < X5. In particular, the highest value of momentum flux occurs at Y = 27 cm (~$4 \cdot 10^{-1}$ m^2/s^2).

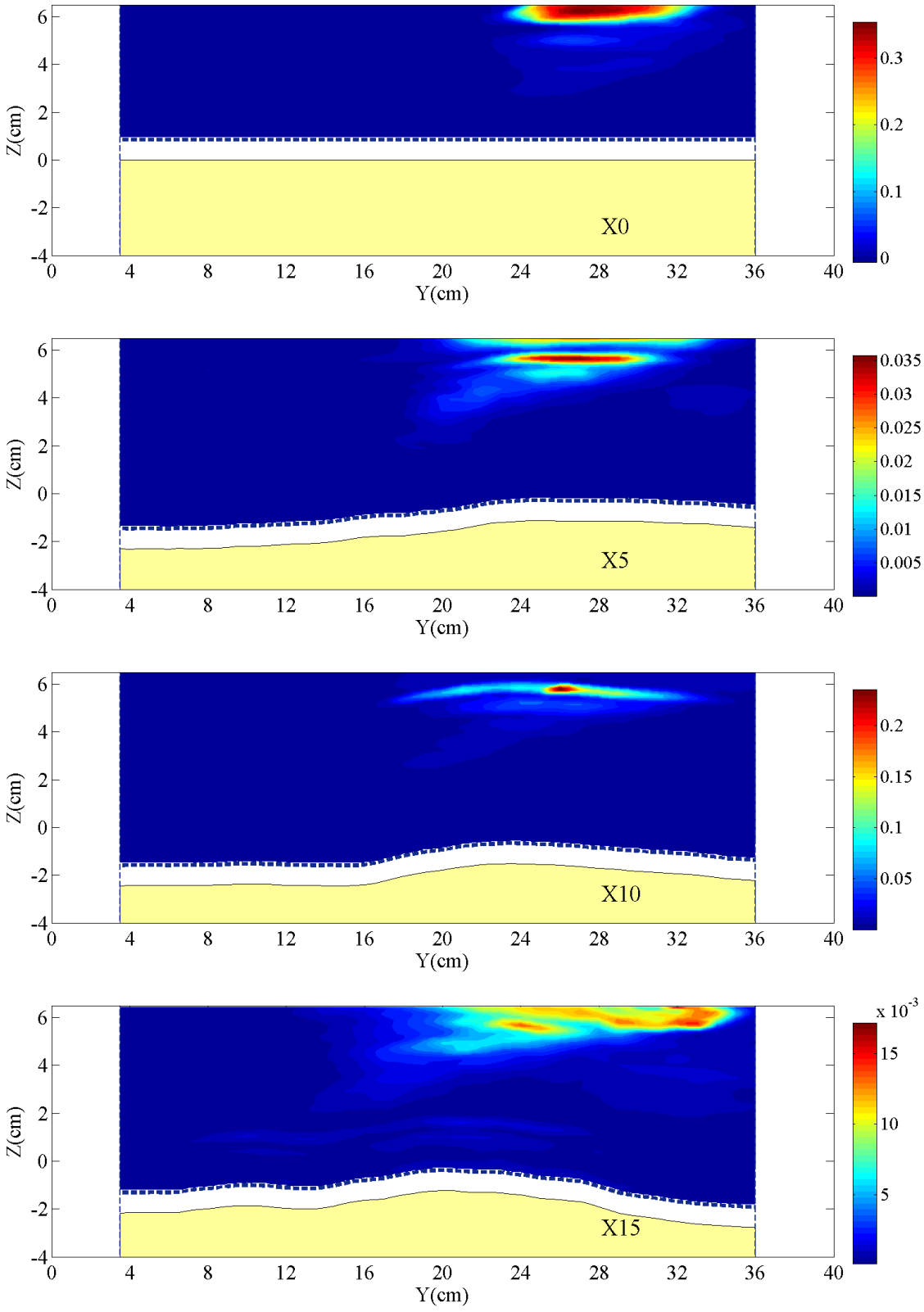

Figure 6.4 – Contour maps of $\overline{u'_y u'_y}$ (m^2/s^2): a) X0 < X < X15.

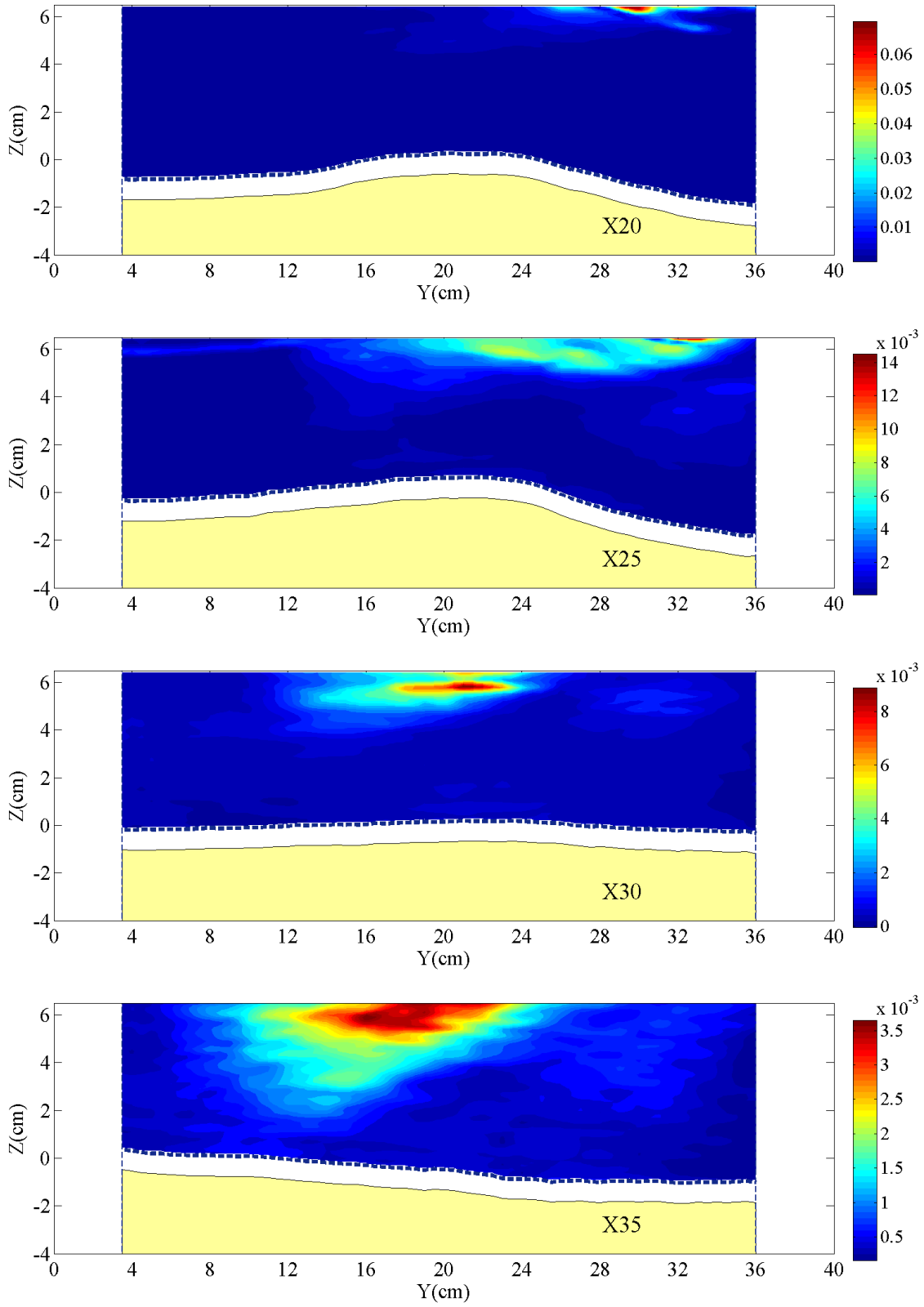

Figure 6.4 – Contour maps of $\overline{u'_y u'_y}$ (m^2/s^2): b) X20 < X < X35.

.

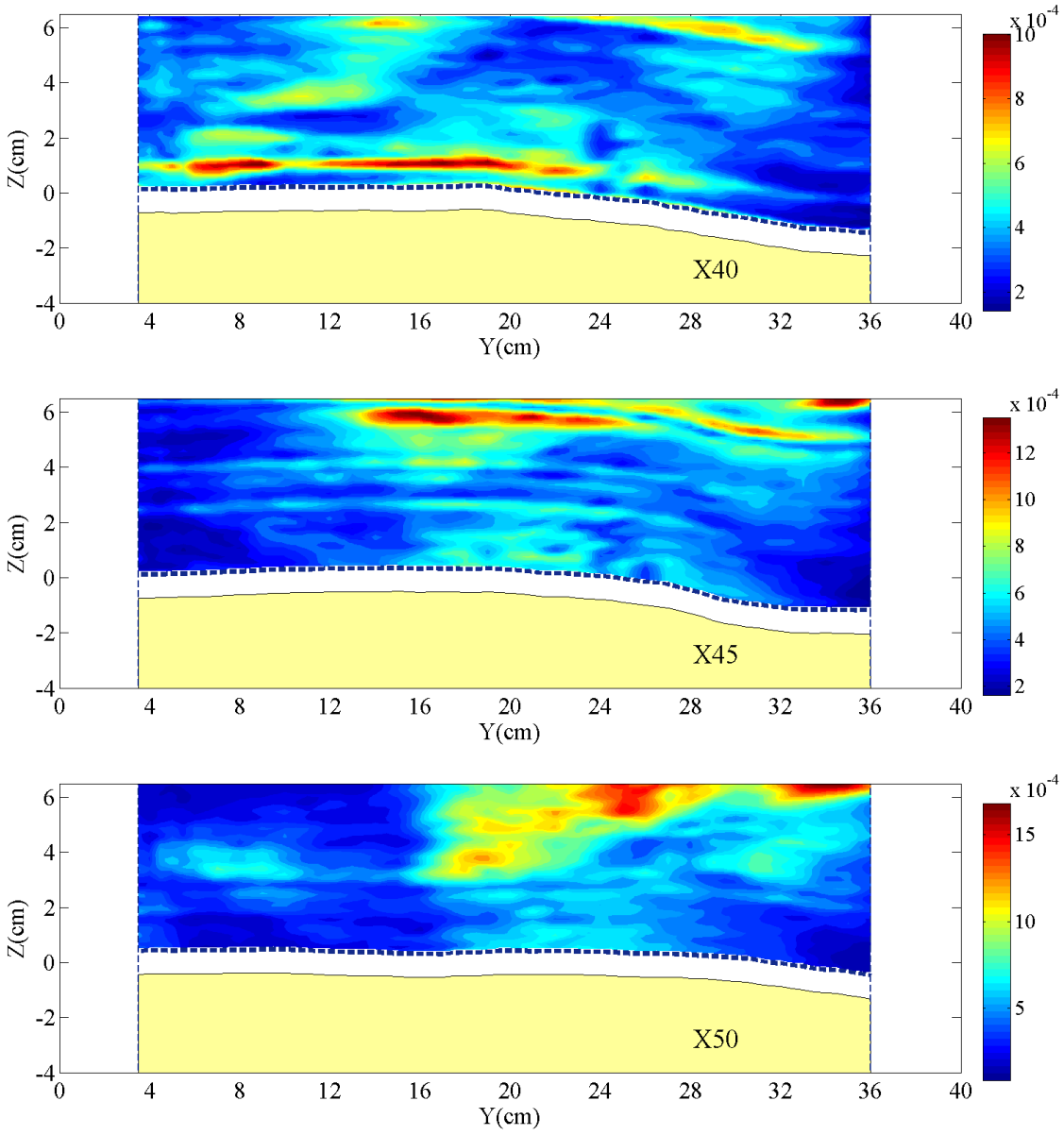

Figure 6.4 – Contour maps of $\overline{u'_y u'_y}$ (m^2/s^2): c) X40 < X < X50.

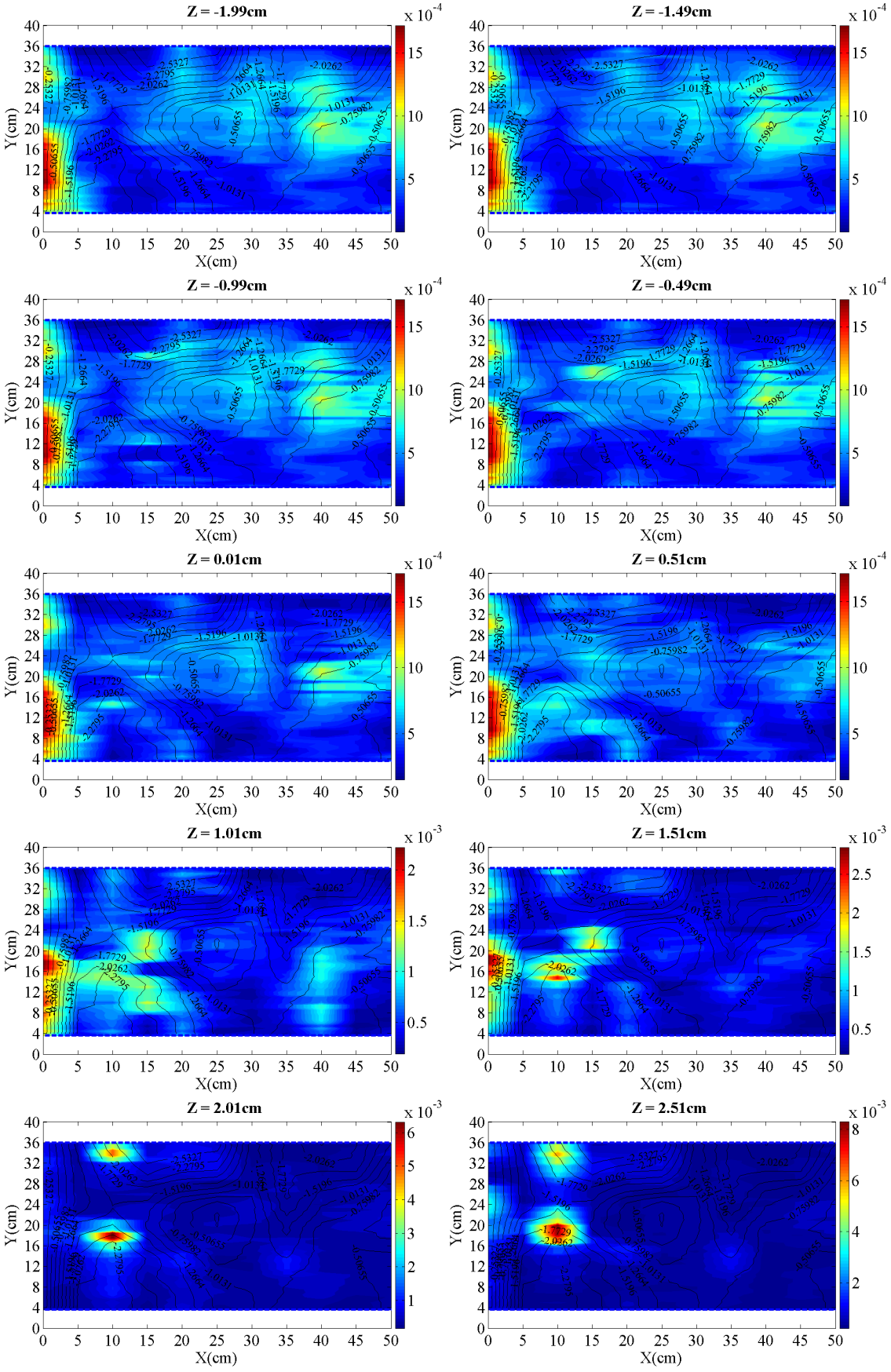

Figure 6.5 – Horizontal contour maps of $\overline{u'_y u'_y}$ (m^2/s^2): a) -1.99cm < Z < 2.51cm.

.

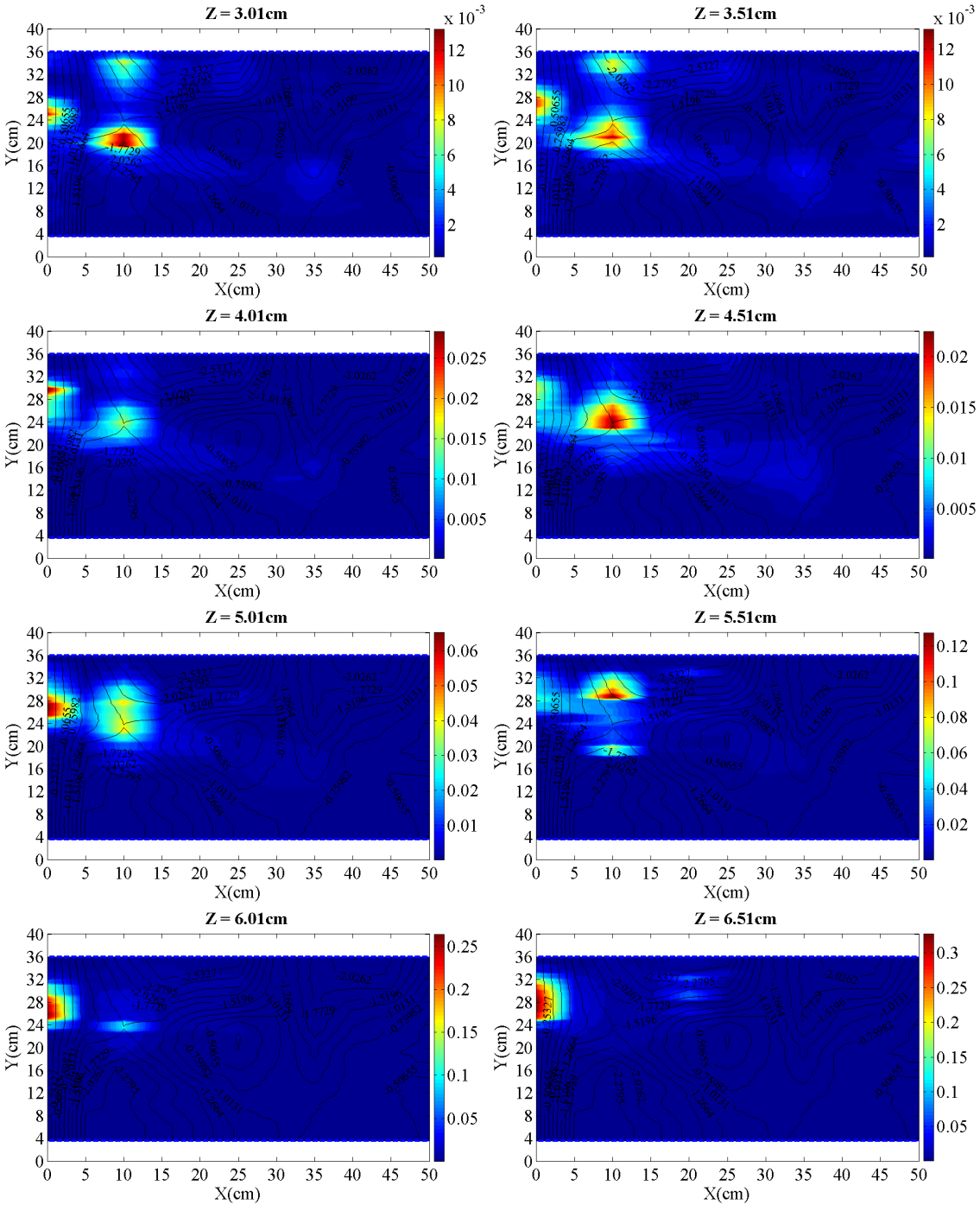

Figure 6.5 – Horizontal contour maps of $\overline{u'_y u'_y}$ (m^2/s^2): b) 3.01cm < Z < 6.51cm.

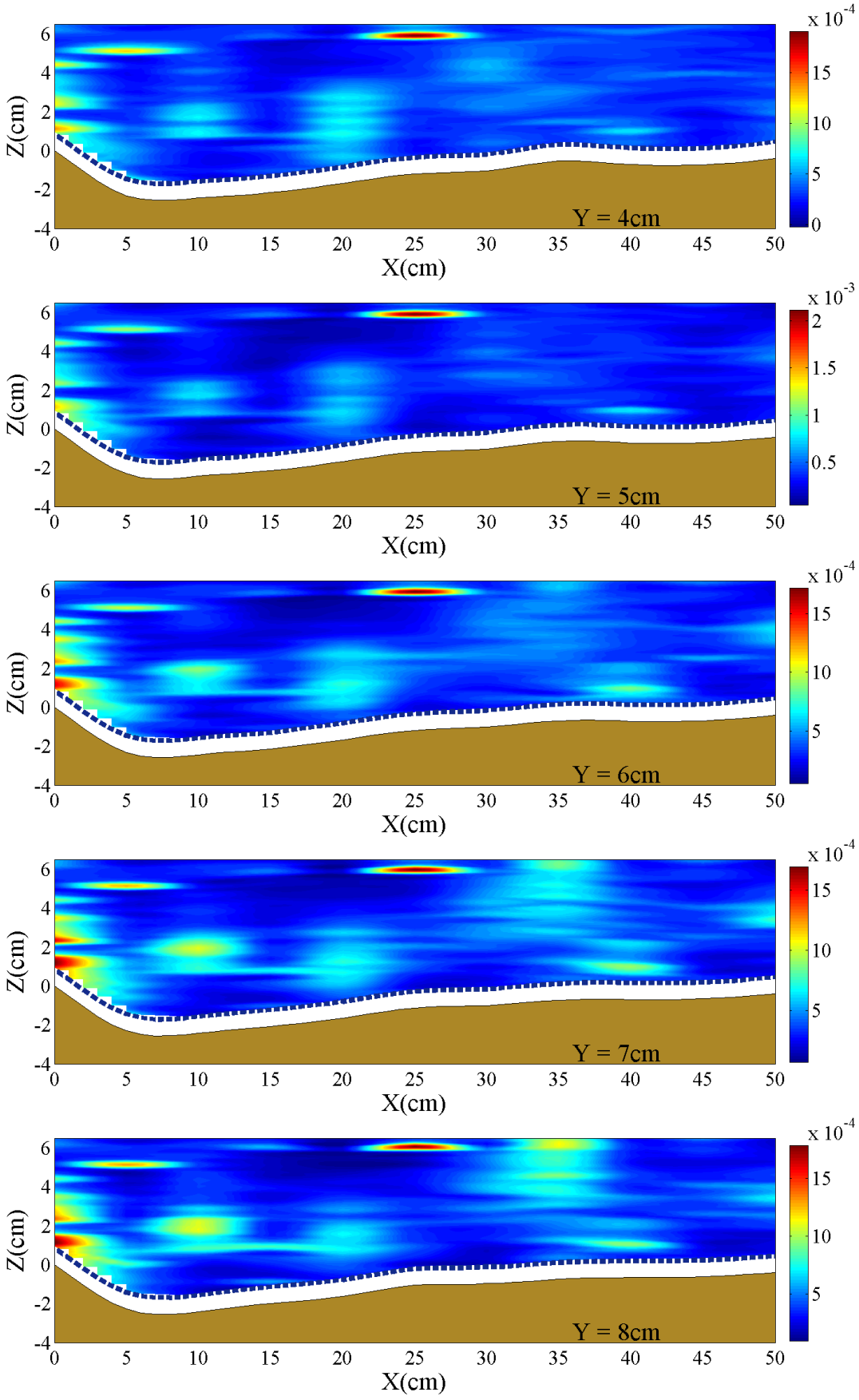

Figure 6.6 – Longitudinal contour maps of $\overline{u'_y u'_y}$ (m^2/s^2): a) 4cm < Y < 8cm.

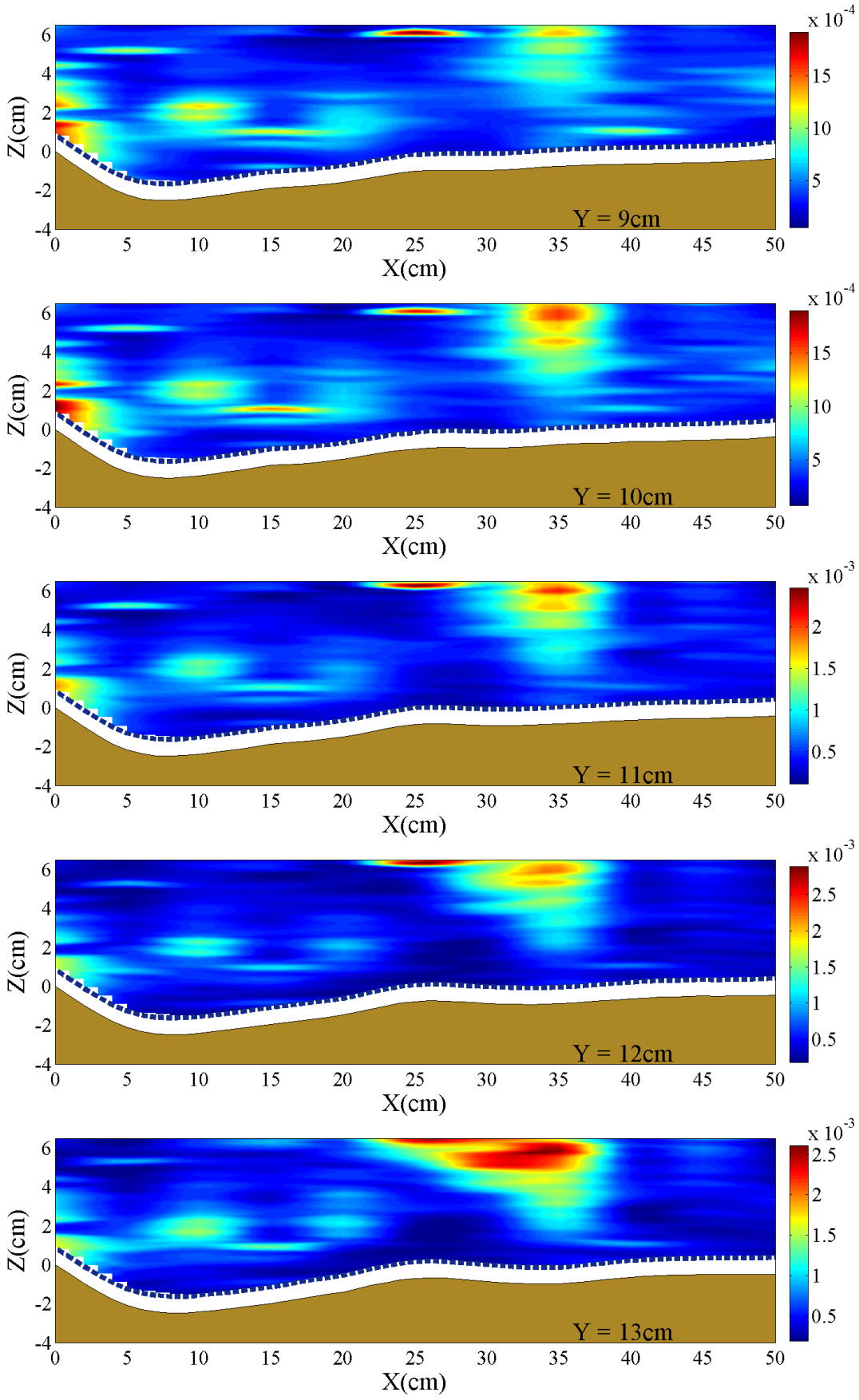

Figure 6.6 – Longitudinal contour maps of $\overline{u'_y u'_y}$ (m^2/s^2): b) 9cm < Y < 13cm.

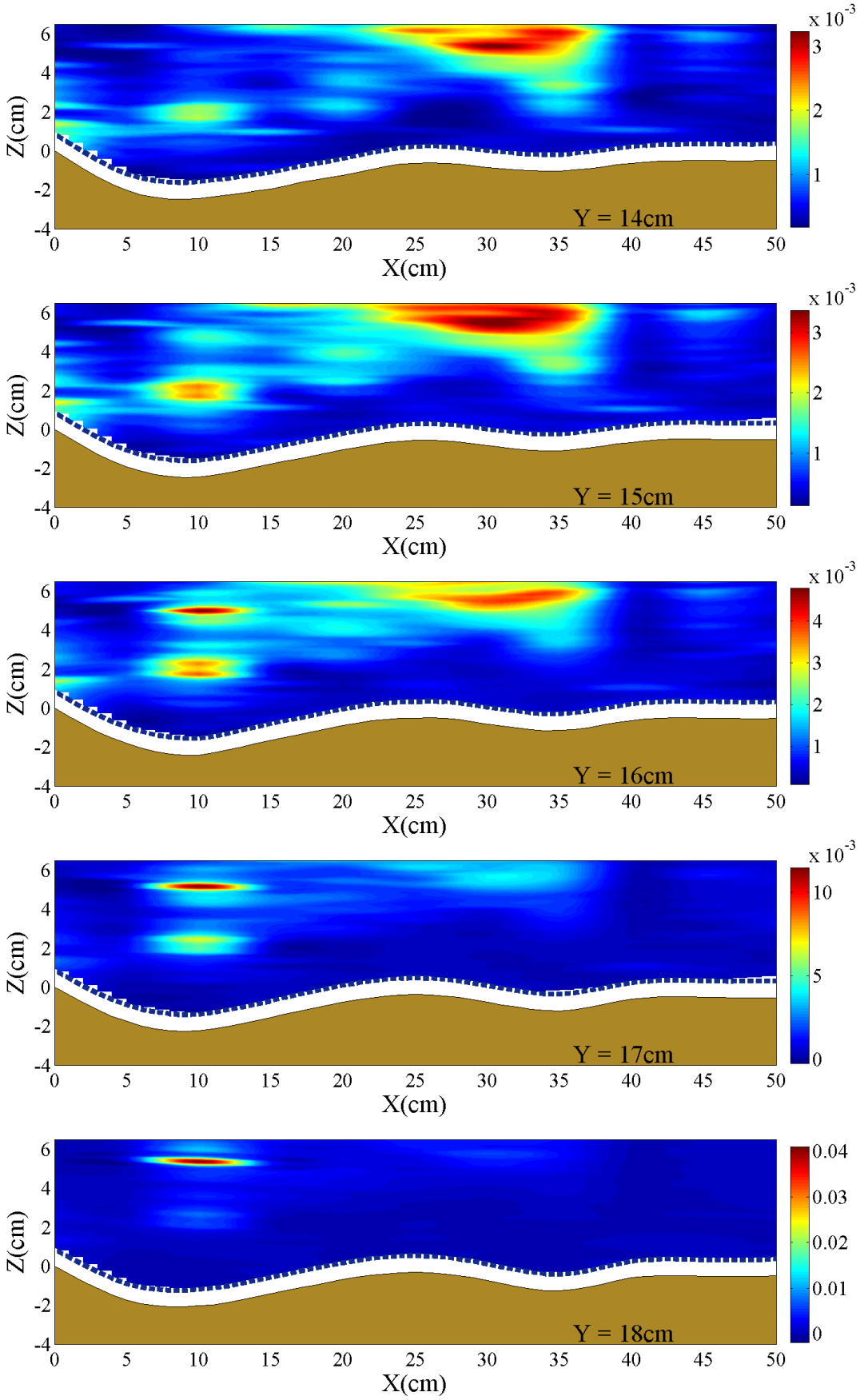

Figure 6.6 – Longitudinal contour maps of $\overline{u'_y u'_y}$ (m^2/s^2): c) 14cm < Y < 18cm.

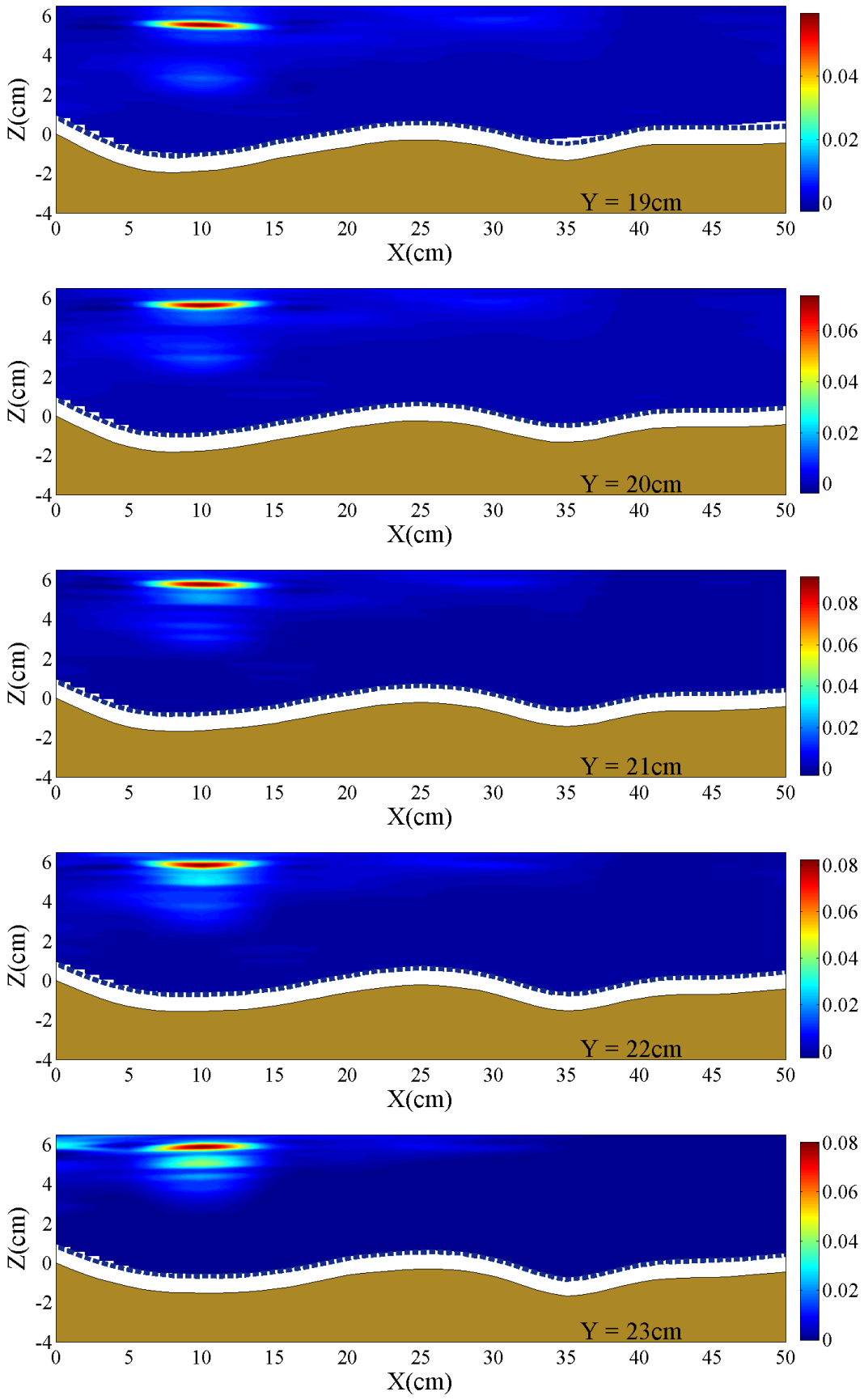

Figure 6.6 – Longitudinal contour maps of $\overline{u'_y u'_y}$ (m^2/s^2): d) 19cm < Y < 23cm.

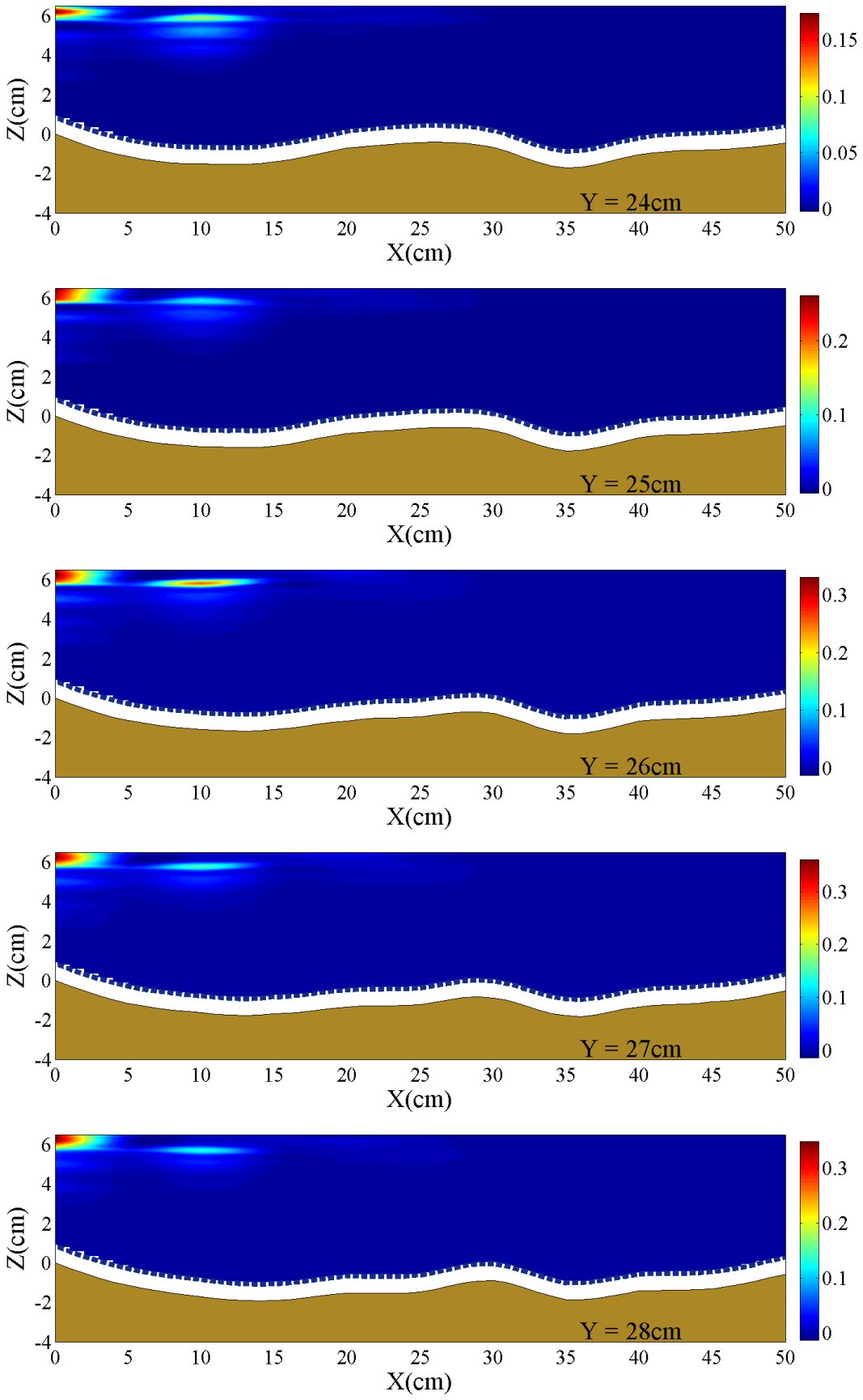

Figure 6.6 – Longitudinal contour maps of $\overline{u'_y u'_y}$ (m^2/s^2): e) 24cm < Y < 28cm.

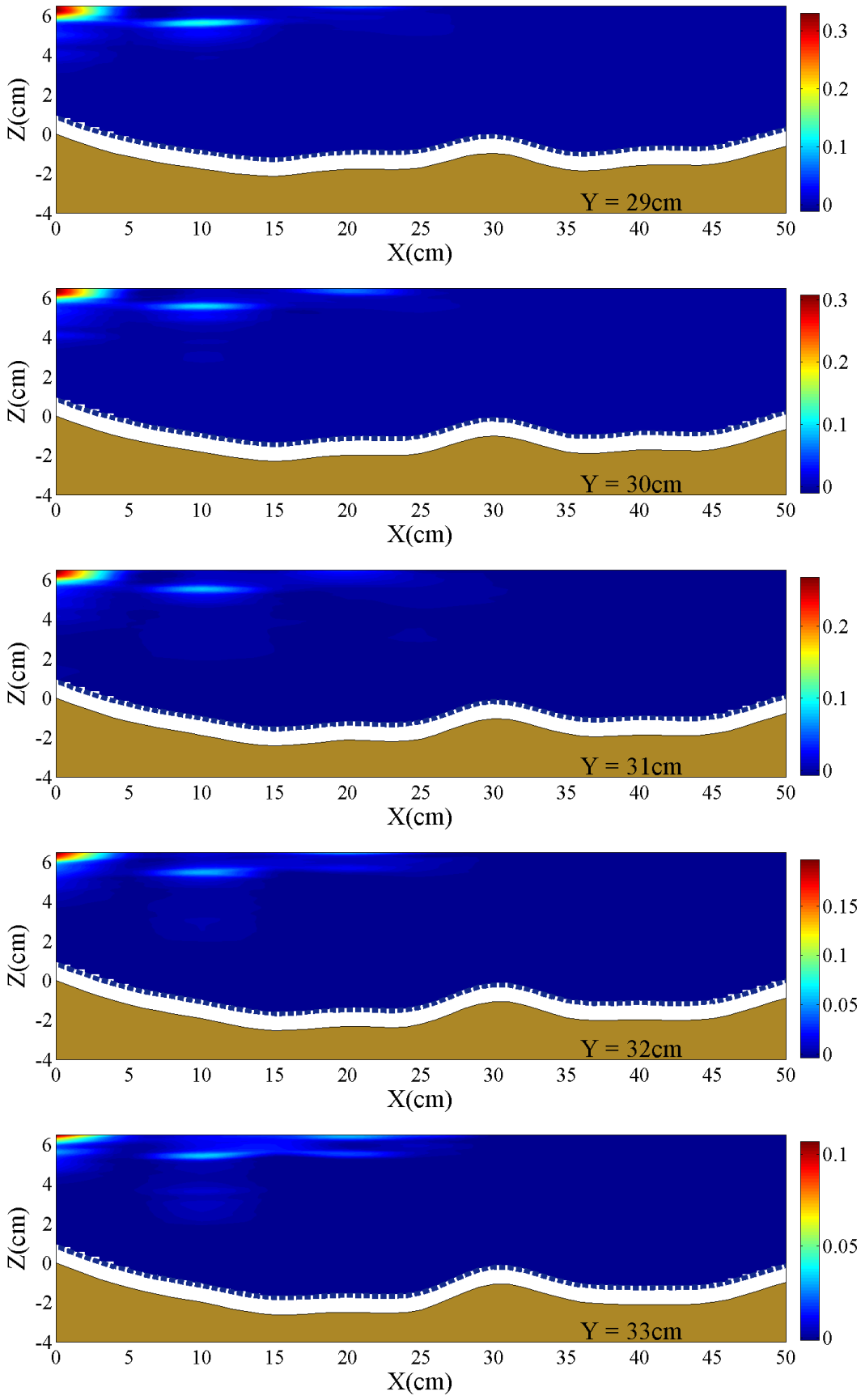

Figure 6.6 – Longitudinal contour maps of $\overline{u'_y u'_y}$ (m^2/s^2): f) 29cm < Y < 33cm.

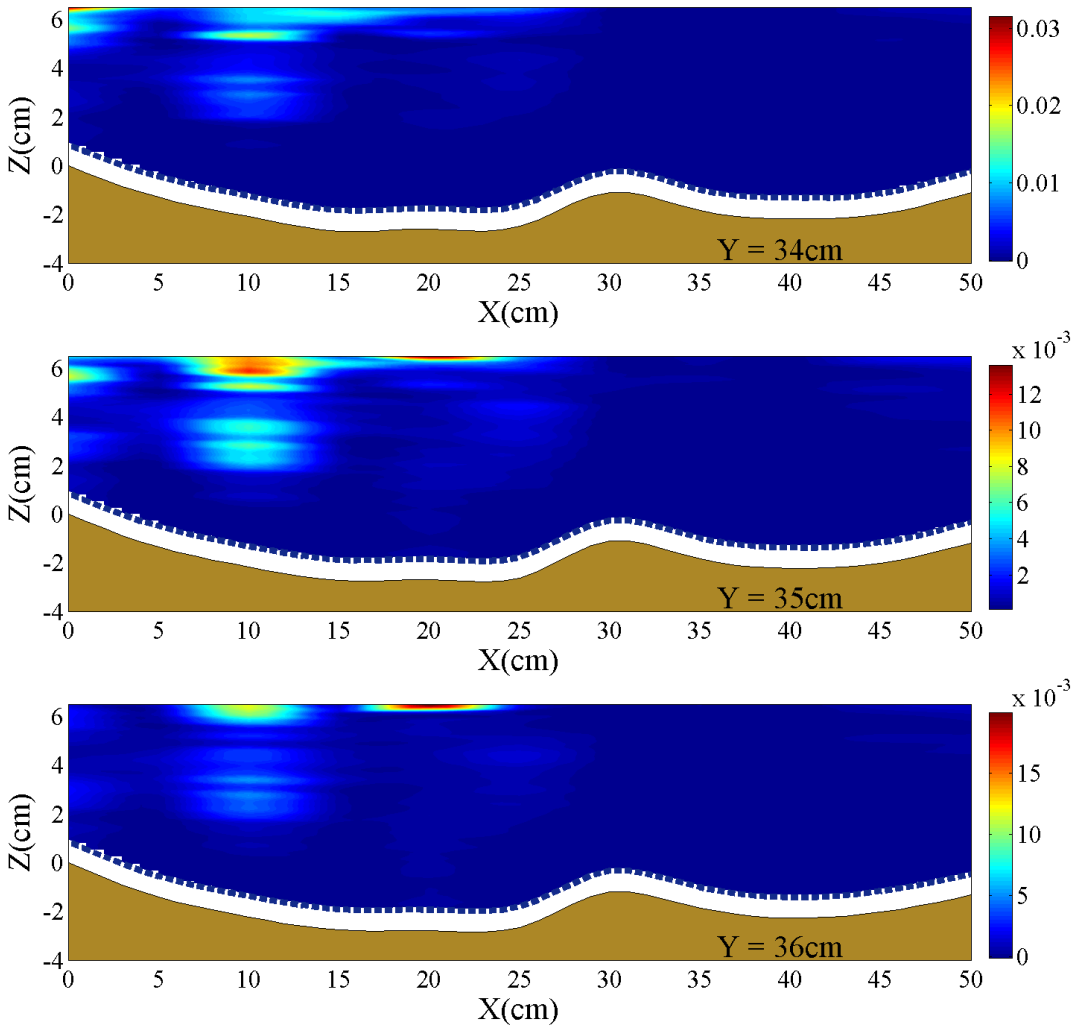

Figure 6.6 – Longitudinal contour maps of $\overline{u'_y u'_y}$ (m^2/s^2): g) 34cm < Y < 36cm.

- *Reynolds momentum flux* $\overline{u'_z u'_z}$

The contour maps of the Reynolds momentum flux component $\overline{u'_z u'_z}$, reported in Figure 6.7, highlight that the pattern of $\overline{u'_z u'_z}$ is almost symmetrical with respect to the channel axis. Passing from section X0 to section X15, $\overline{u'_z u'_z}$ increases in value close to the bed in the near-bank regions (4cm < Y < 18cm and 28cm <Y < 36cm).

From section X20 to section X50, the Figures 6.7b-c show that the pattern of the momentum flux $\overline{u'_z u'_z}$, decreases in value in the near-bank regions and increases in the

central region (18cm < Y < 28cm). Thus the pattern of $\overline{u_z' u_z'}$ seems to be related to the scour evolution: $\overline{u_z' u_z'}$ increases where the scour develops.

The horizontal contour maps of the Reynolds momentum flux component $\overline{u_z' u_z'}$ for different Z are reported in Figure 6.8. This figure shows that streaks of high/low momentum fluxes occur in the central region. Near the bed, for Z < -0.49 cm (see Figure 6.8a) high values of momentum flux are found inside the scour holes (X < X30) and in general, where erosion takes place (X ≥ X35 and Y ≥18 cm).

The longitudinal distribution of the Reynolds momentum flux component $\overline{u_z' u_z'}$ for different values of the transversal abscissa Y are reported in Figure 6.9. It can be observed that near the right bank (Y = 4 cm and Y = 5 cm, see Figure 6.9a) $\overline{u_z' u_z'}$ assumes inside the scour hole (X < X25). Then, approaching to Y = 10 cm (Figures 6.9b-c) the region of high values of $\overline{u_z' u_z'}$ extends towards X > X25. Moving toward the direction of the channel axis, high value of $\overline{u_z' u_z'}$ are especially found for X > X40 (downstream the deposit) near the bed. Within the central region (see Figures 6.9d-e) it can be observed that $\overline{u_z' u_z'}$ assumes high values both near the bed and near the free surface. For Y > 27 cm (Figures 6.9e-d), $\overline{u_z' u_z'}$ increases in value again near the bed, downstream the deposit (for X > X40) and into the scour hole (X < X30). For longitudinal sections Y > 33 cm (see Figures 6.9f-g) the increasing of the vertical Reynolds momentum flux $\overline{u_z' u_z'}$, is more evident in the scour hole. Thus Figures 6.7÷6.9 confirm that the distribution of the Reynolds momentum flux, $\overline{u_z' u_z'}$ allows us to identify the pattern of flow turbulence and the sediment motion. In particular, it can be observed that three regions of high Reynolds momentum flux can be distinguish near the bed: two regions near the banks (for Y < 18cm and Y > 28cm) and a region for 18cm < Y < 28cm.

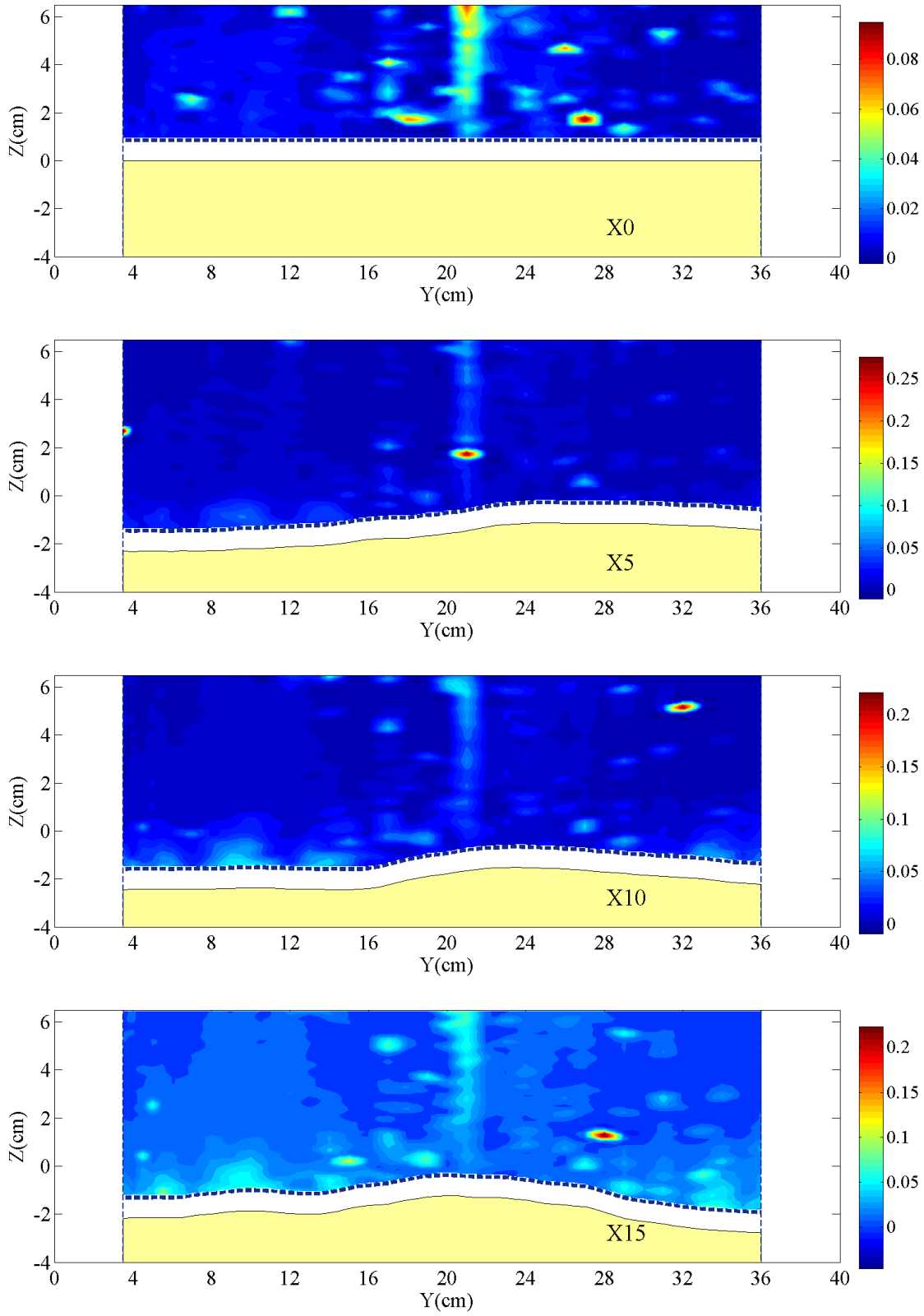

Figure 6.7 – Contour maps of $\overline{u_z' u_z'}$ (m^2/s^2): a) X0 < X < X15.

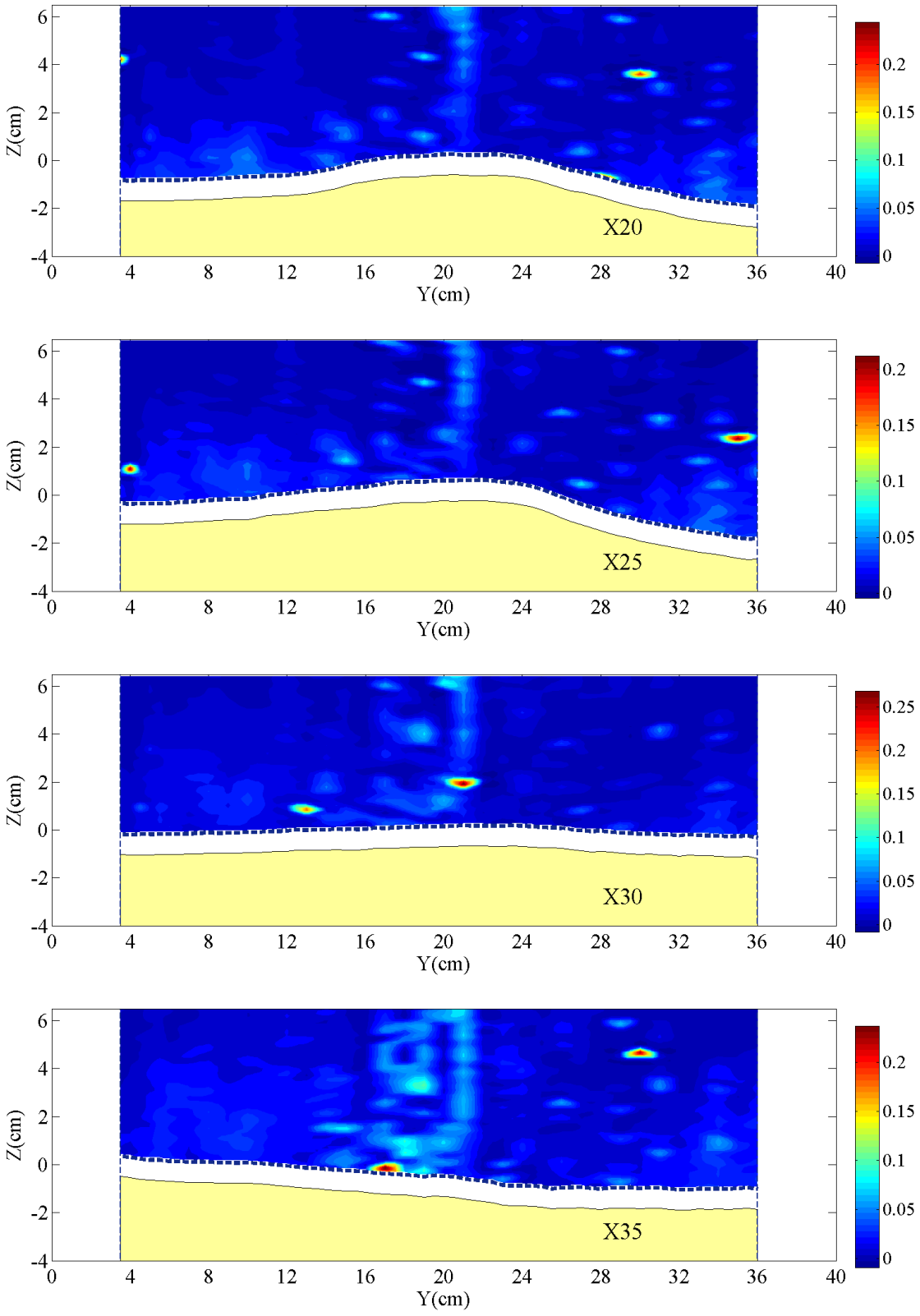

Figure 6.7 – Contour maps of $\overline{u_z' u_z'}$ (m^2/s^2): b) X20 < X < X35.

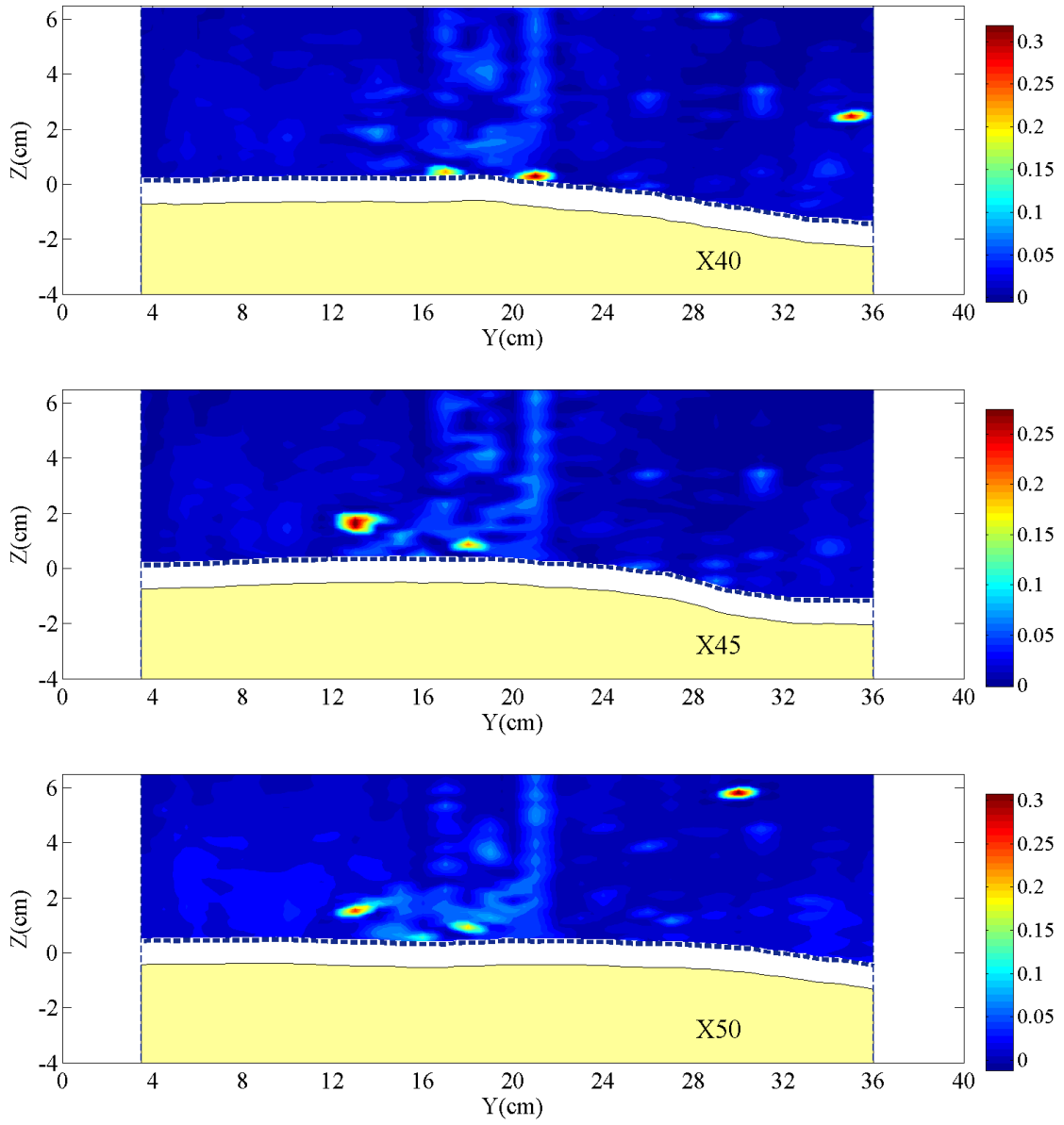

Figure 6.7 – Contour maps of $\overline{u_z' u_z'}$ (m^2/s^2): c) X40 < X < X50.

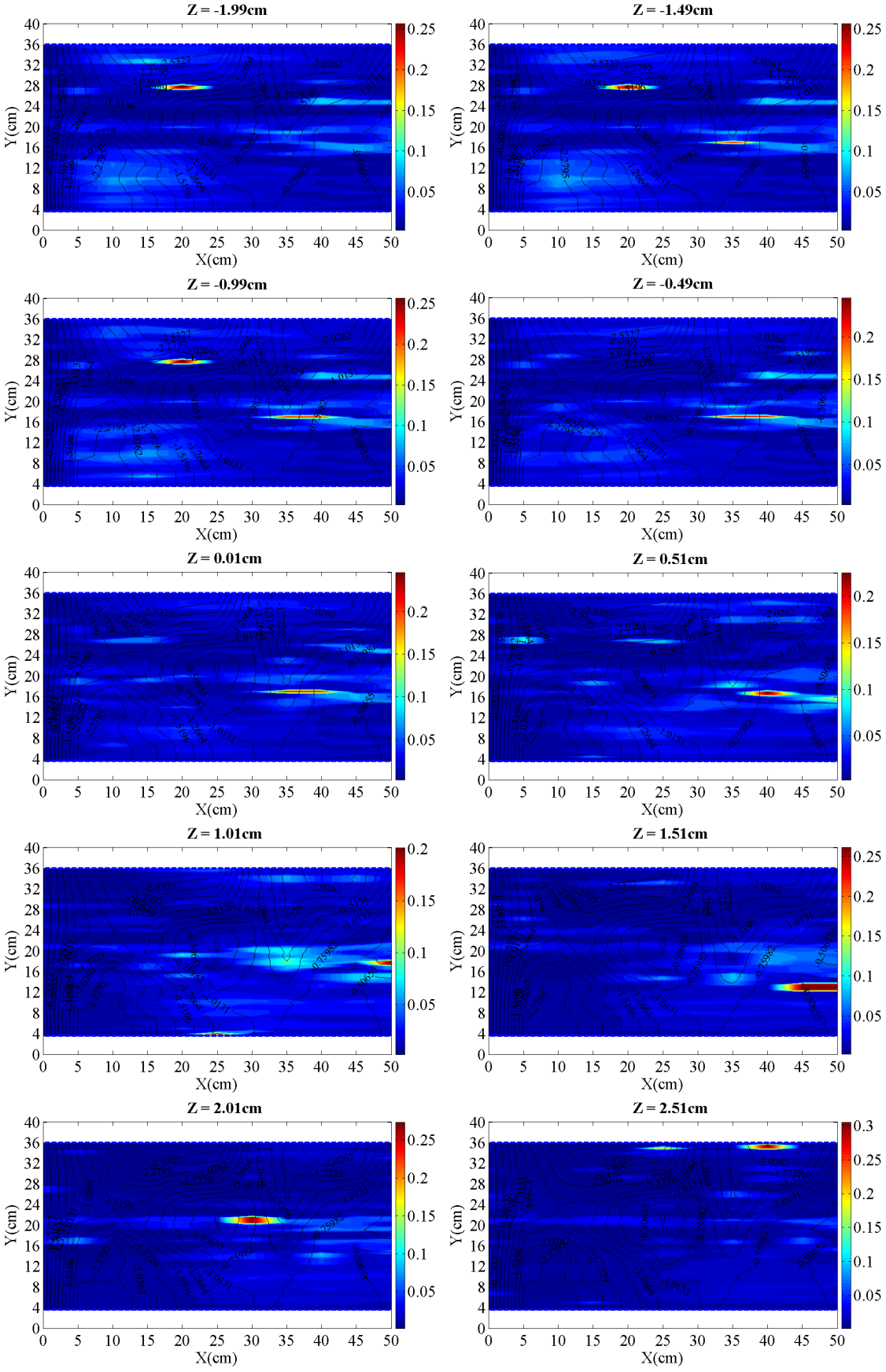

Figure 6.8 – Horizontal contour maps of $\overline{u_z' u_z'}$ (m^2/s^2): a) -1.99cm < Z < 2.51cm.

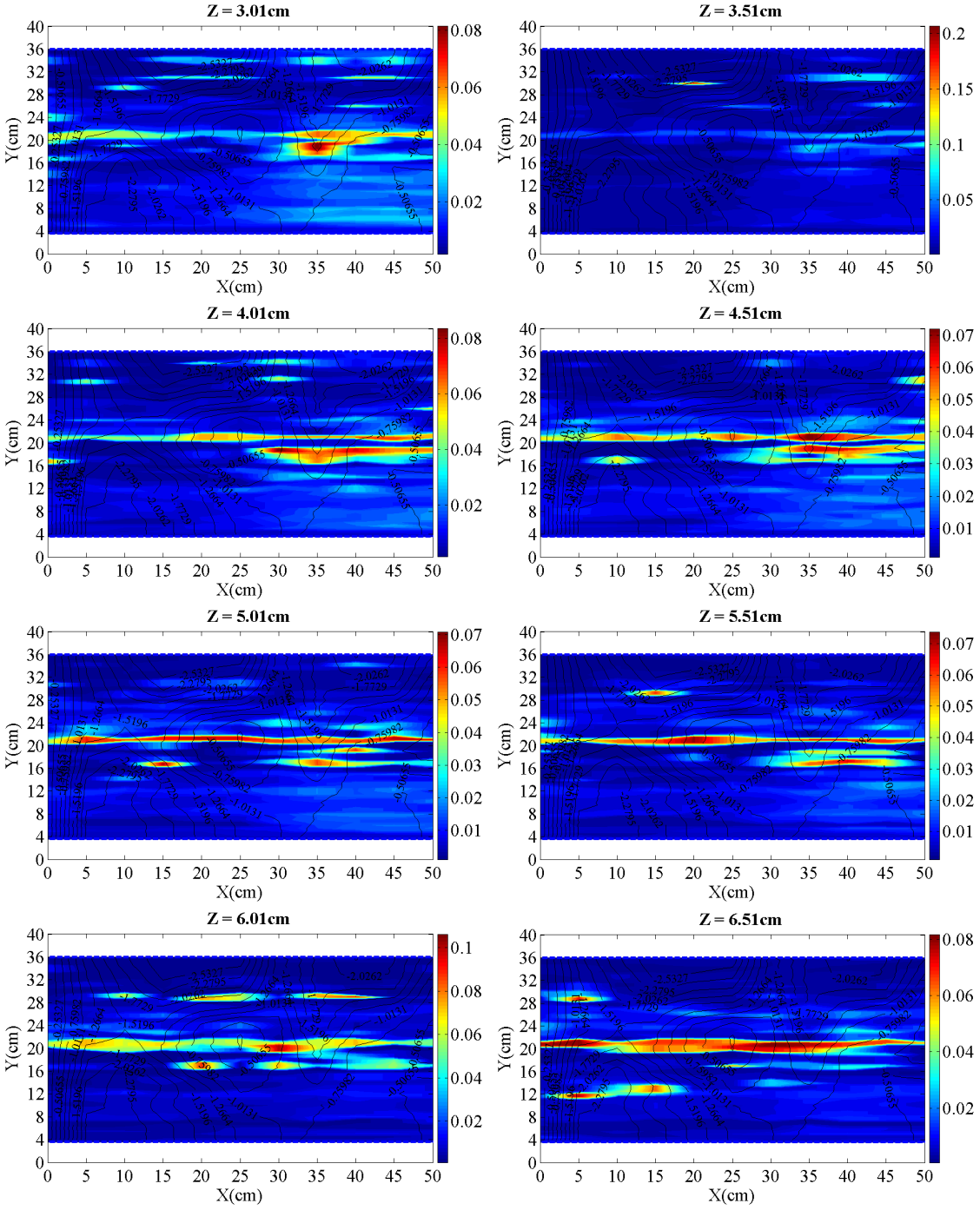

Figure 6.8 – Horizontal contour maps of $\overline{u_z' u_z'}$ (m^2/s^2): b) 3.01cm < Z < 6.51cm.

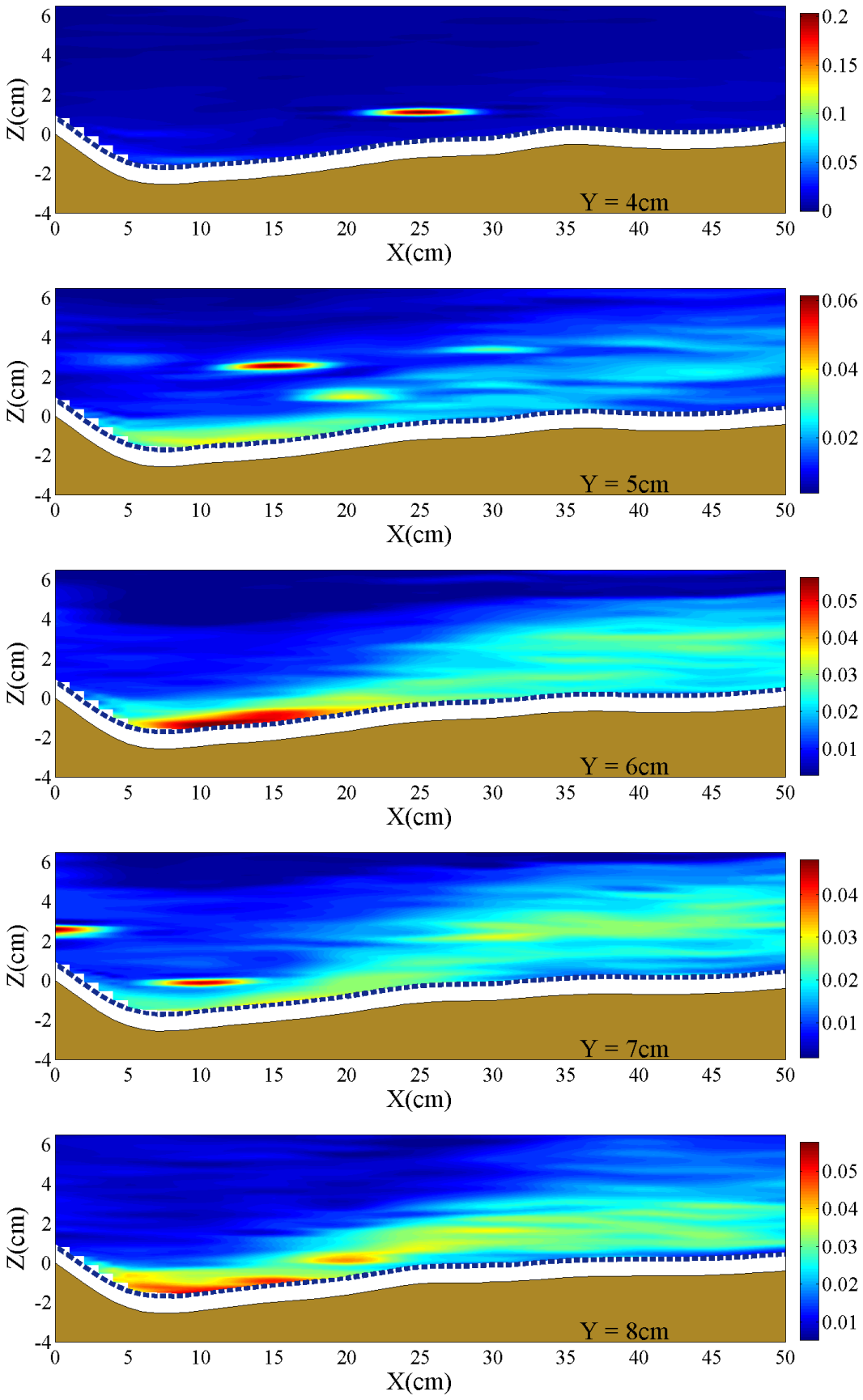

Figure 6.9 – Longitudinal contour maps of $\overline{u'_z u'_z}$ (m^2/s^2): a) 4cm < Y < 8cm.

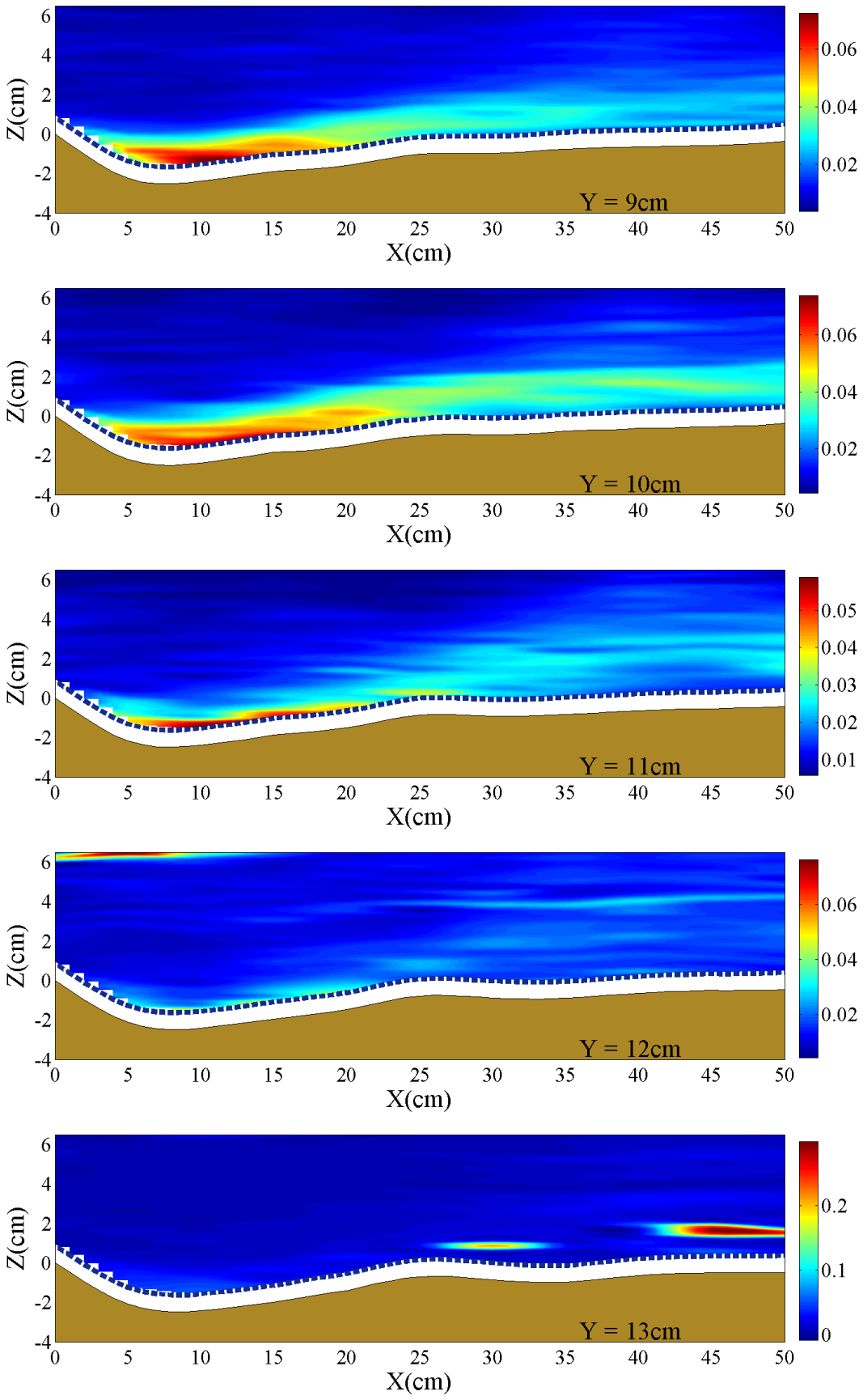

Figure 6.9 – Longitudinal contour maps of $\overline{u_z' u_z'}$ (m^2/s^2): b) 9cm < Y < 13cm.

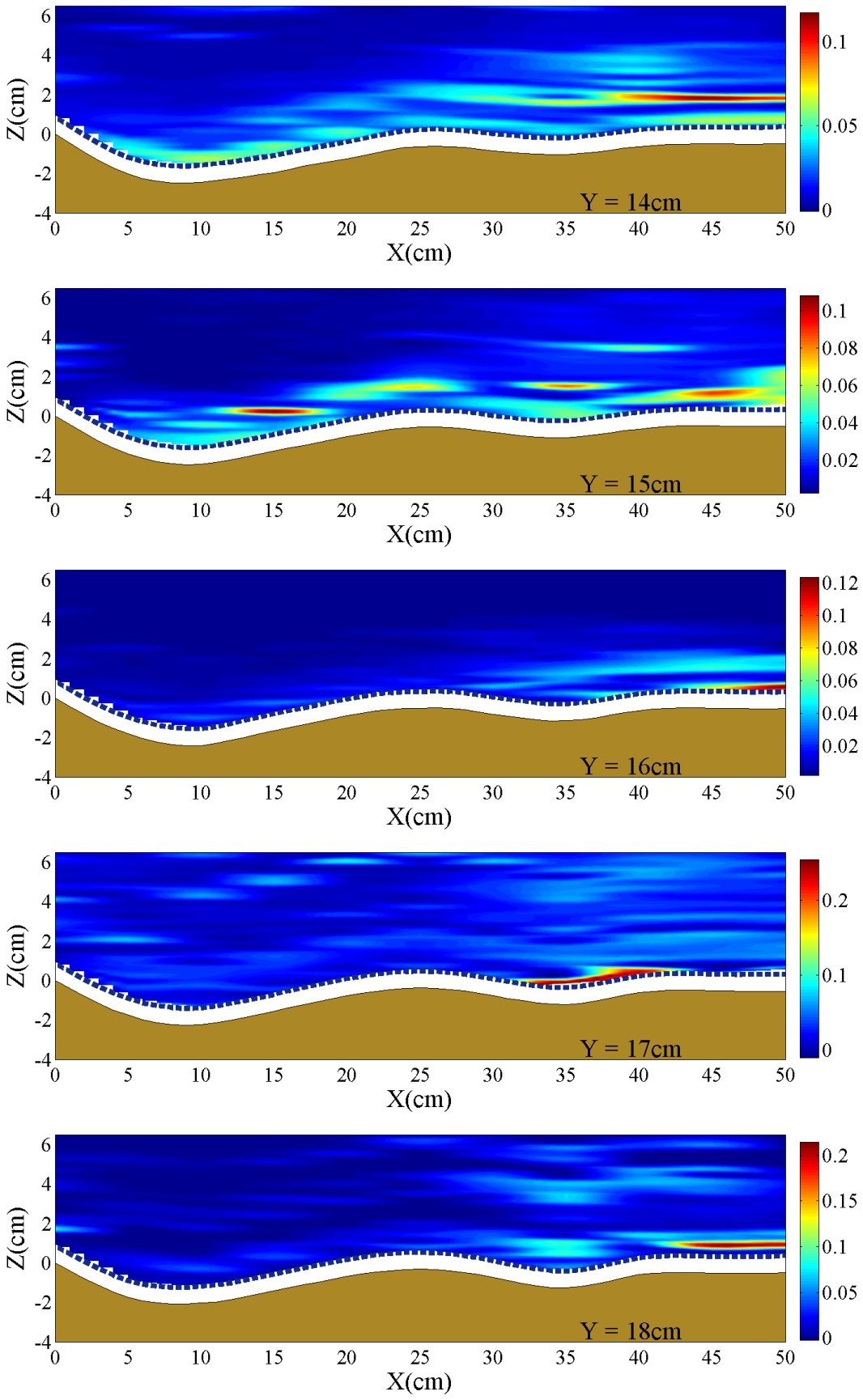

Figure 6.9 – Longitudinal contour maps of $\overline{u_z' u_z'}$ (m^2/s^2): c) 14cm < Y < 18cm.

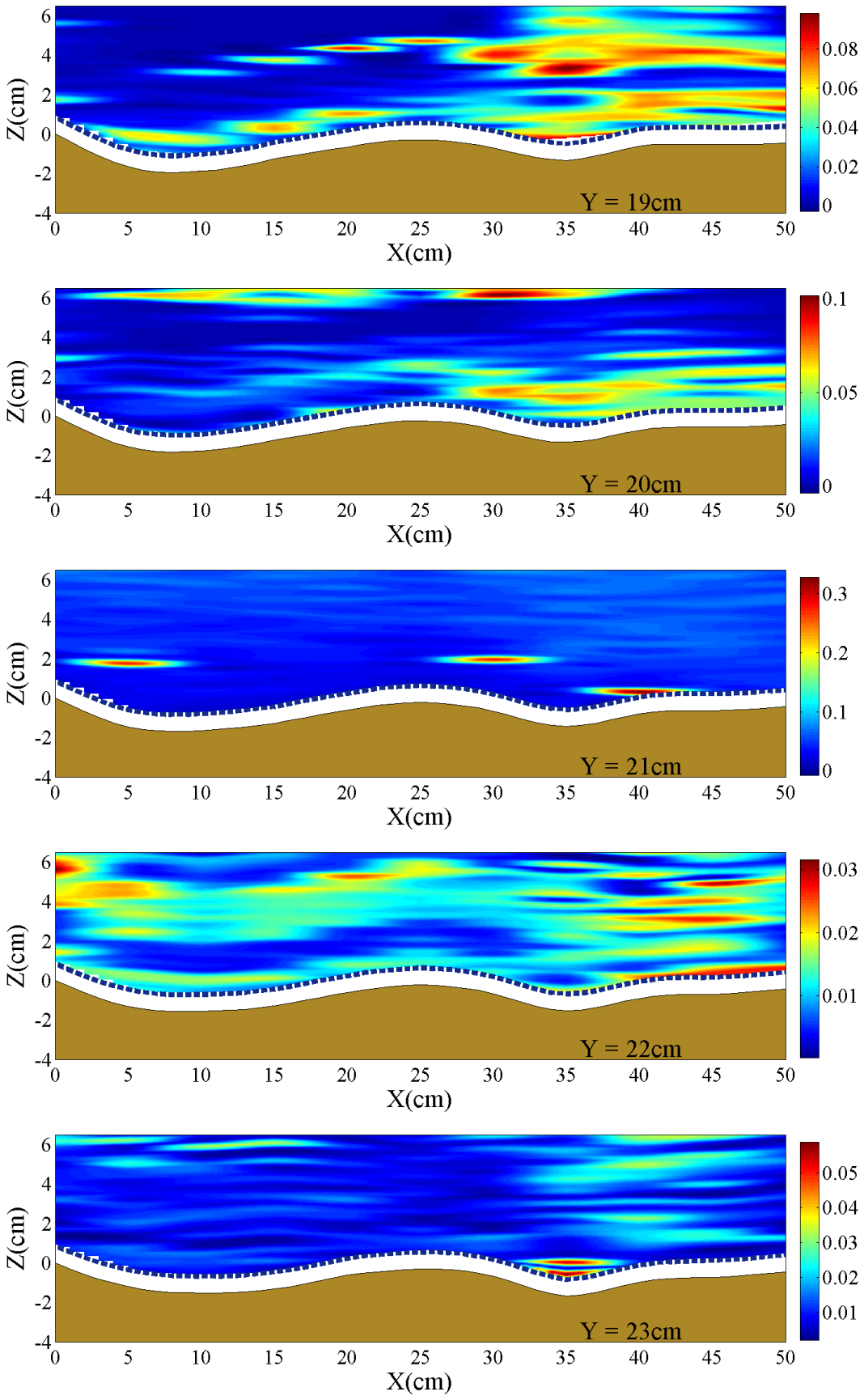

Figure 6.9 – Longitudinal contour maps of $\overline{u_z' u_z'}$ (m^2/s^2): d) 19cm < Y < 23cm.

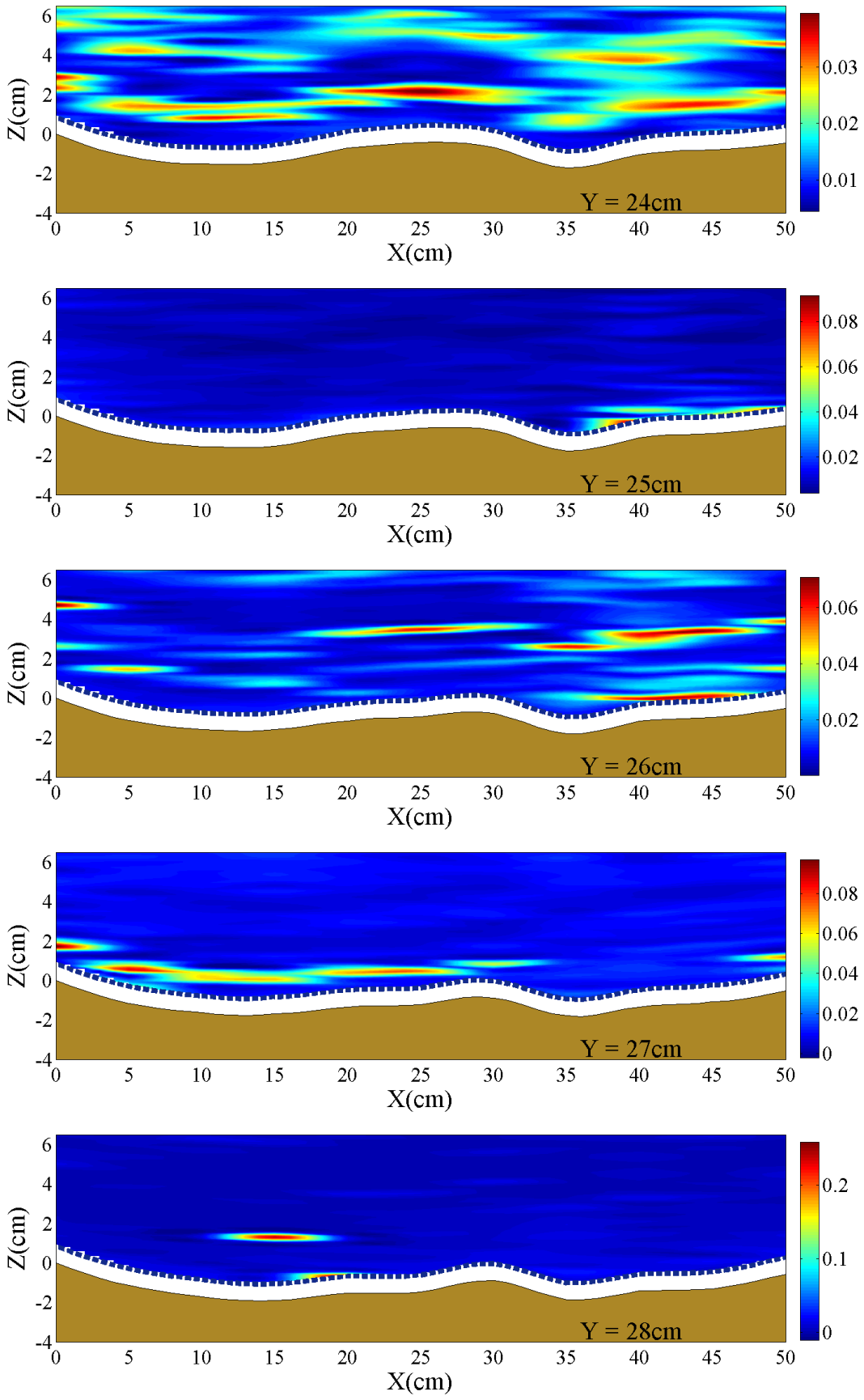

Figure 6.9 – Longitudinal contour maps of $\overline{u_z' u_z'}$ (m^2/s^2): e) 24cm < Y < 28cm.

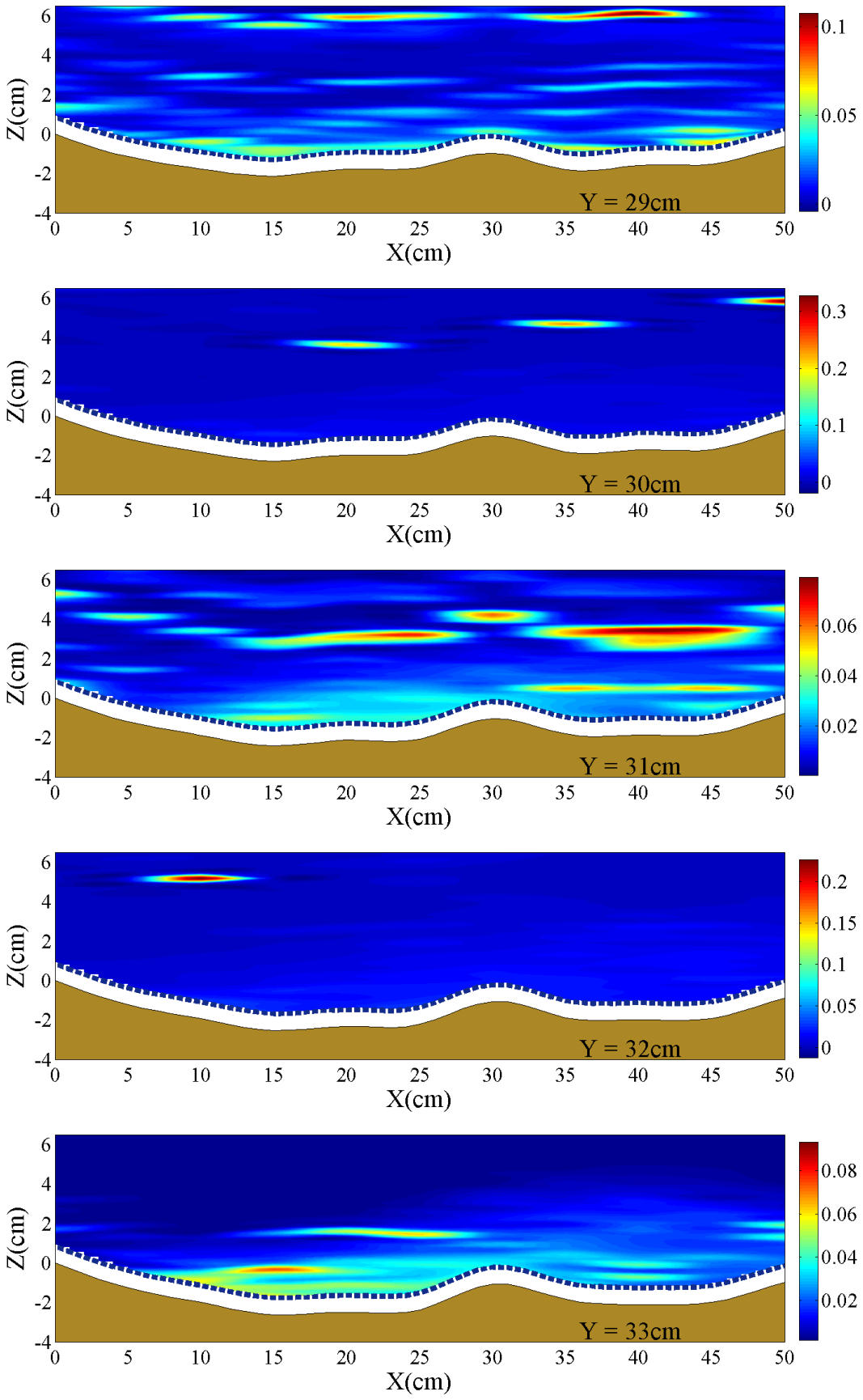

Figure 6.9 – Longitudinal contour maps of $\overline{u_z' u_z'}$ (m^2/s^2): f) 29cm < Y < 33cm.

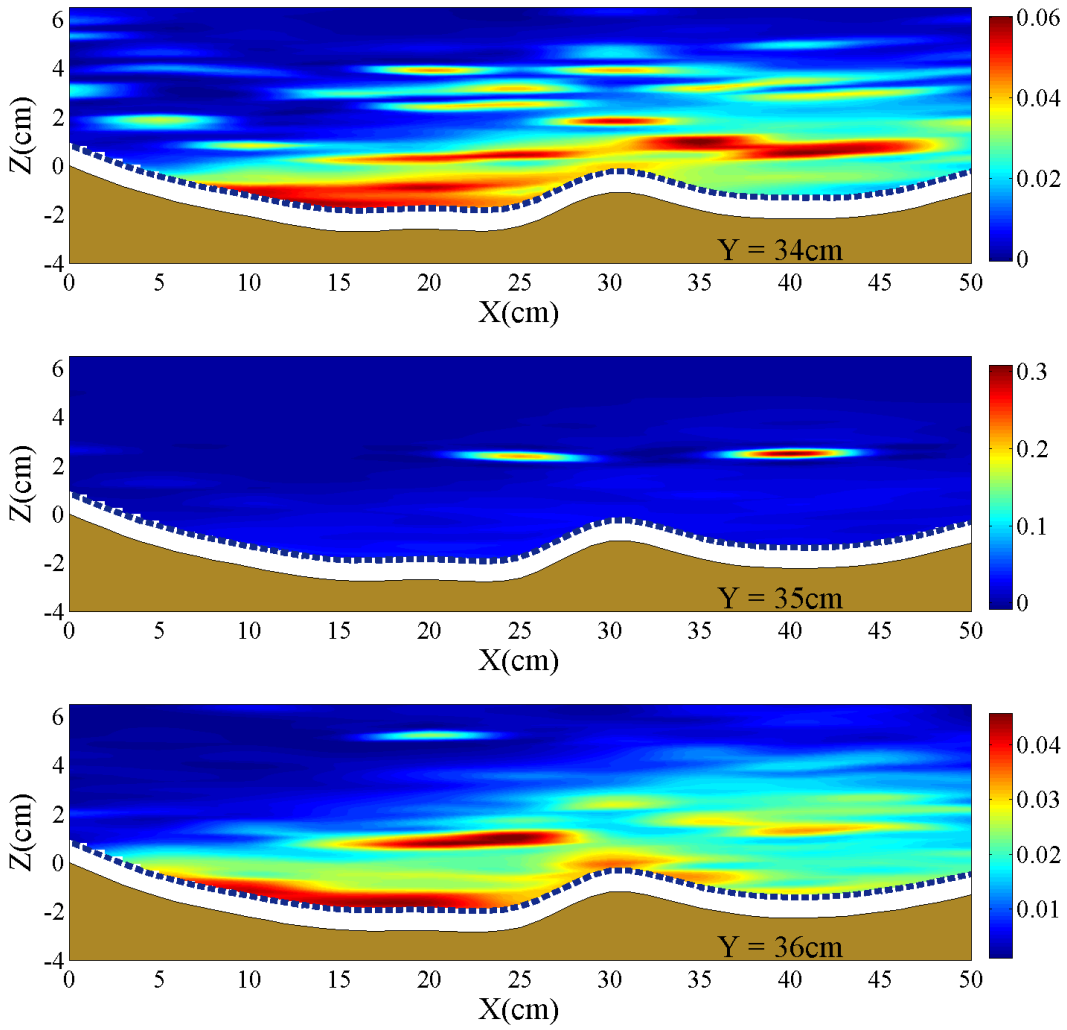

Figure 6.9 – Longitudinal contour maps of $\overline{u_z' u_z'}$ (m^2/s^2): g) 34cm < Y < 36cm.

- *Reynolds momentum flux* $\overline{u'_x u'_y}$

The distributions of the Reynolds momentum flux $\overline{u'_x u'_y}$ are reported in Figure 6.10. Inside the scour hole, for X< X15 (see Figure 6.10a), high values of Reynolds momentum flux $\overline{u'_x u'_y}$ are found near the free surface in the central region (especially at 22 cm < Y < 30 cm). At section X30 (see Figure 6.10b) $\overline{u'_x u'_y}$ increases especially at the cannel axis along the vertical direction. For X > X35 (see Figure 6.10b-c) high values of $\overline{u'_x u'_y}$ especially occur at the channel axis (near the bed for sections X > X40).

The horizontal distributions of $\overline{u'_x u'_y}$, reported in Figure 6.11, highlight that near the bed (Z < 0, see Figure 6.11a), high positive values of the Reynolds momentum occur near sections X = X10 ÷ X25 and in the near-bank regions.

The longitudinal distributions of $\overline{u'_x u'_y}$ for different values of Y are reported in Figure 6.12. In the near-bank regions (4 cm < Y < 18 cm and 28 cm < Y < 36 cm) an alternating of high positive and negative values of $\overline{u'_x u'_y}$ especially occurs inside the scour hole X < X30.

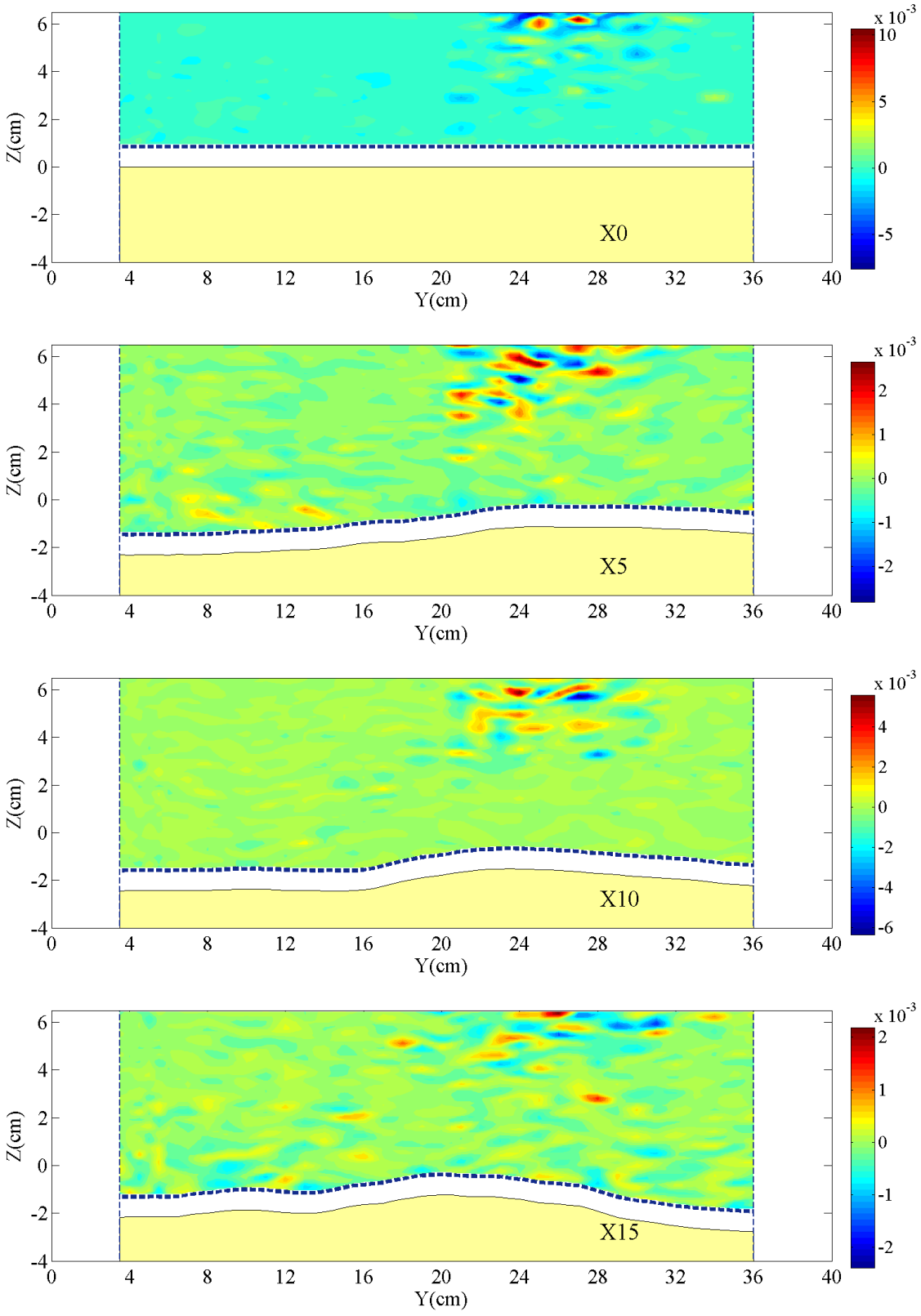

Figure 6.10 – Contour maps of $\overline{u_x' u_y'}$ (m^2/s^2): a) X0 < X < X15.

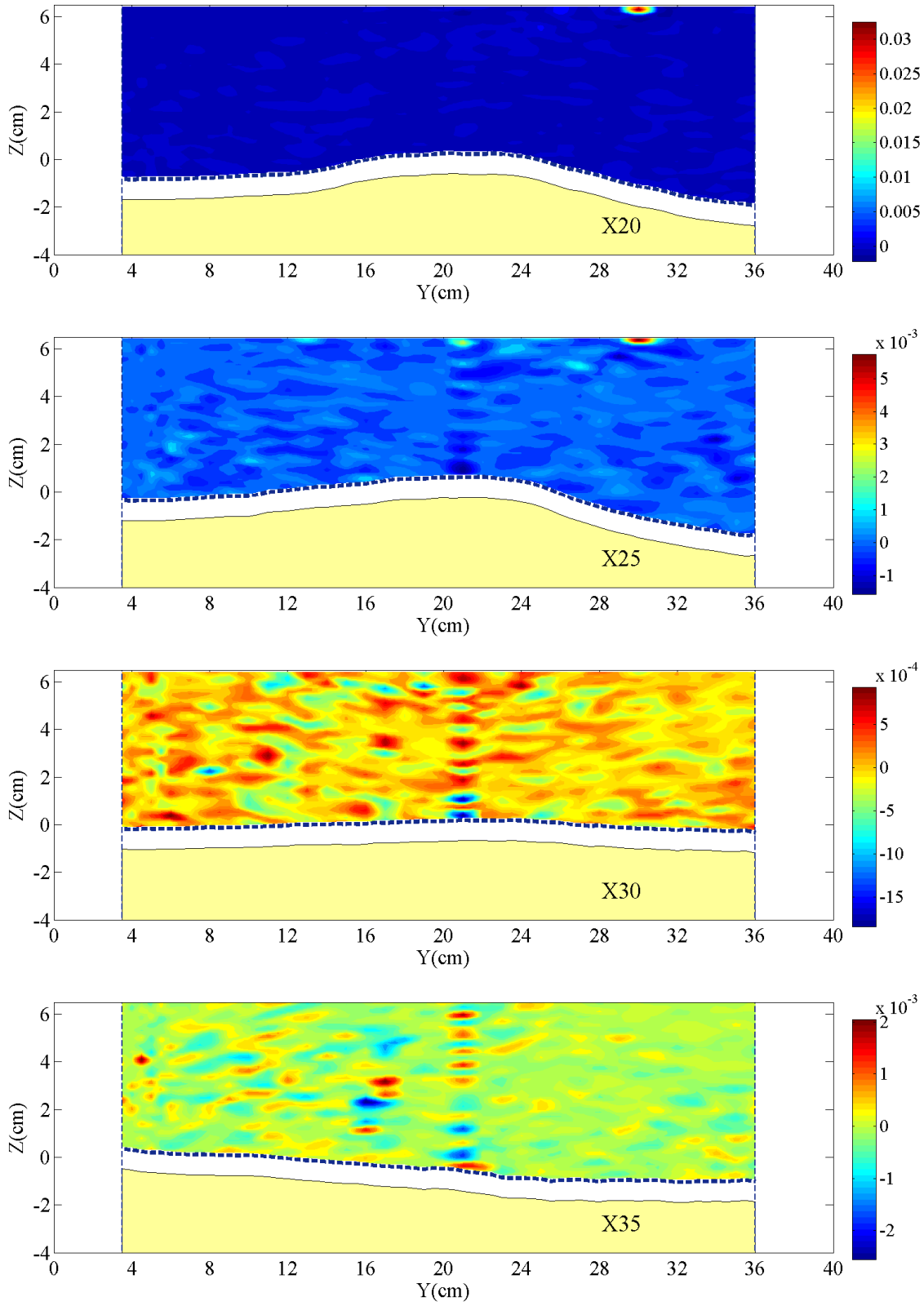

Figure 6.10 – Contour maps of $\overline{u'_x u'_y}$ (m^2/s^2): b) X20 < X < X35.

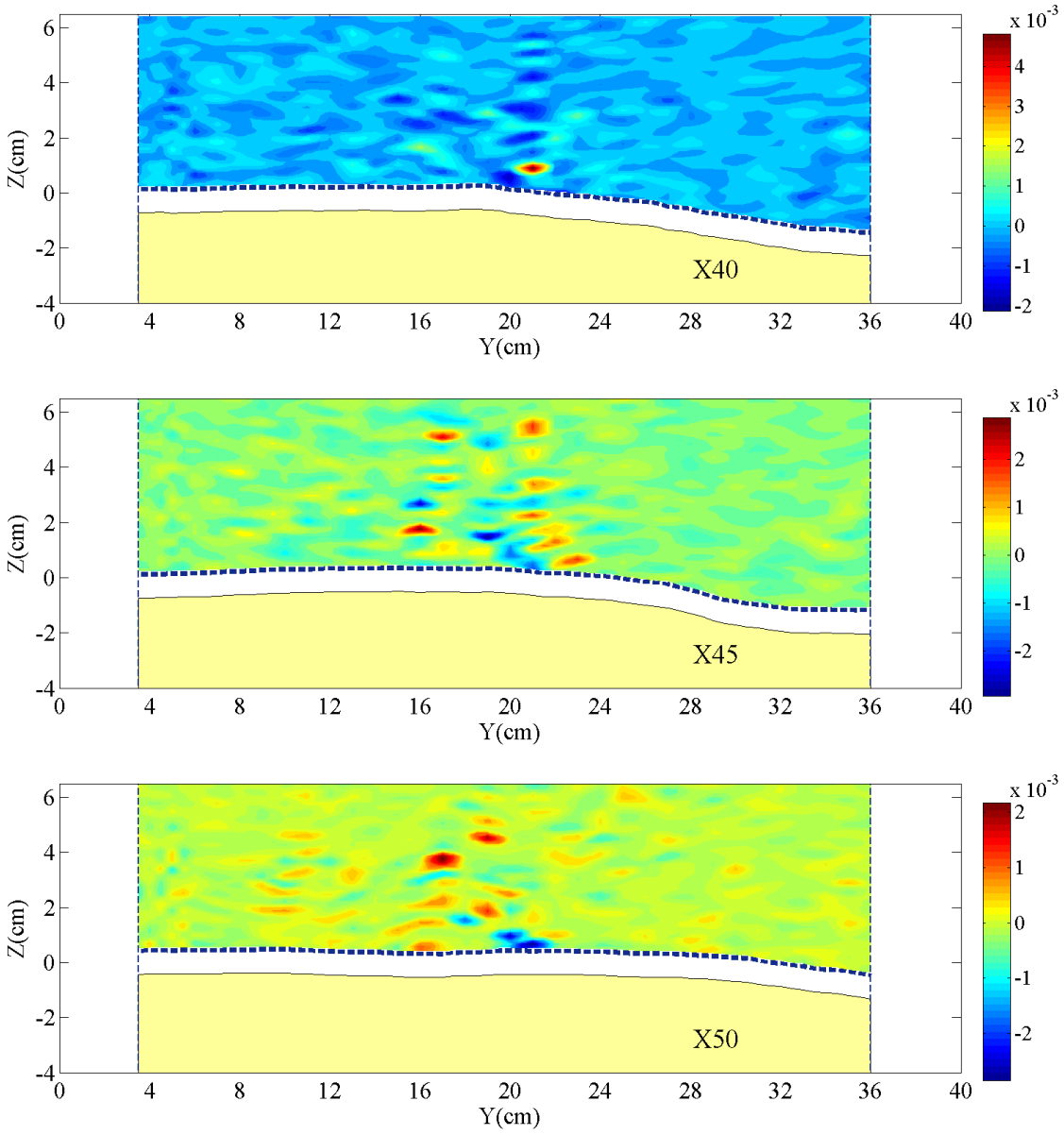

Figure 6.10 – Contour maps of $\overline{u'_x u'_y}$ (m^2/s^2): c) X40 < X < X50.

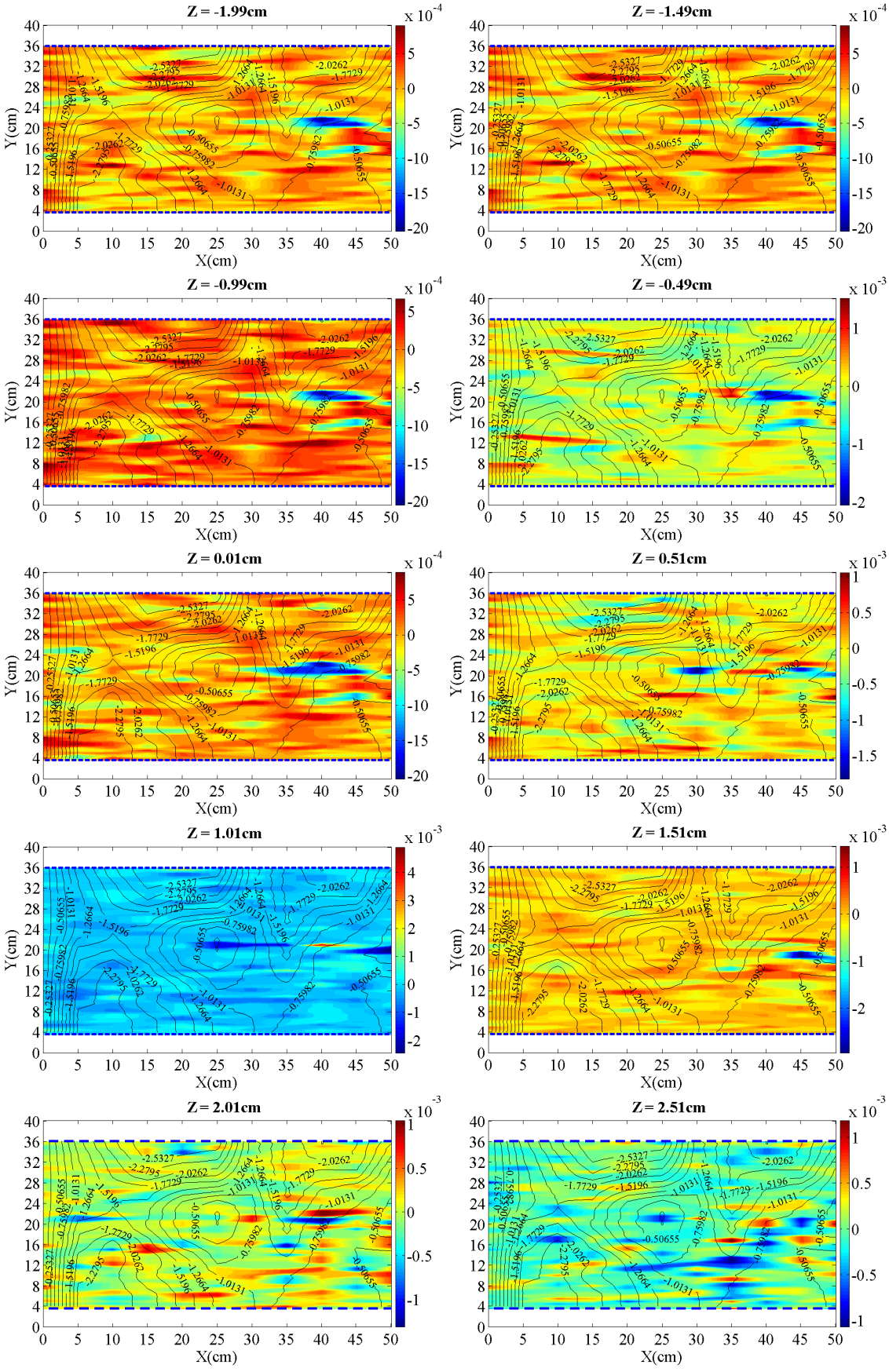

Figure 6.11 – Horizontal contour maps of $\overline{u'_x u'_y}$ (m^2/s^2): a) -1.99cm < Z < 2.51cm.

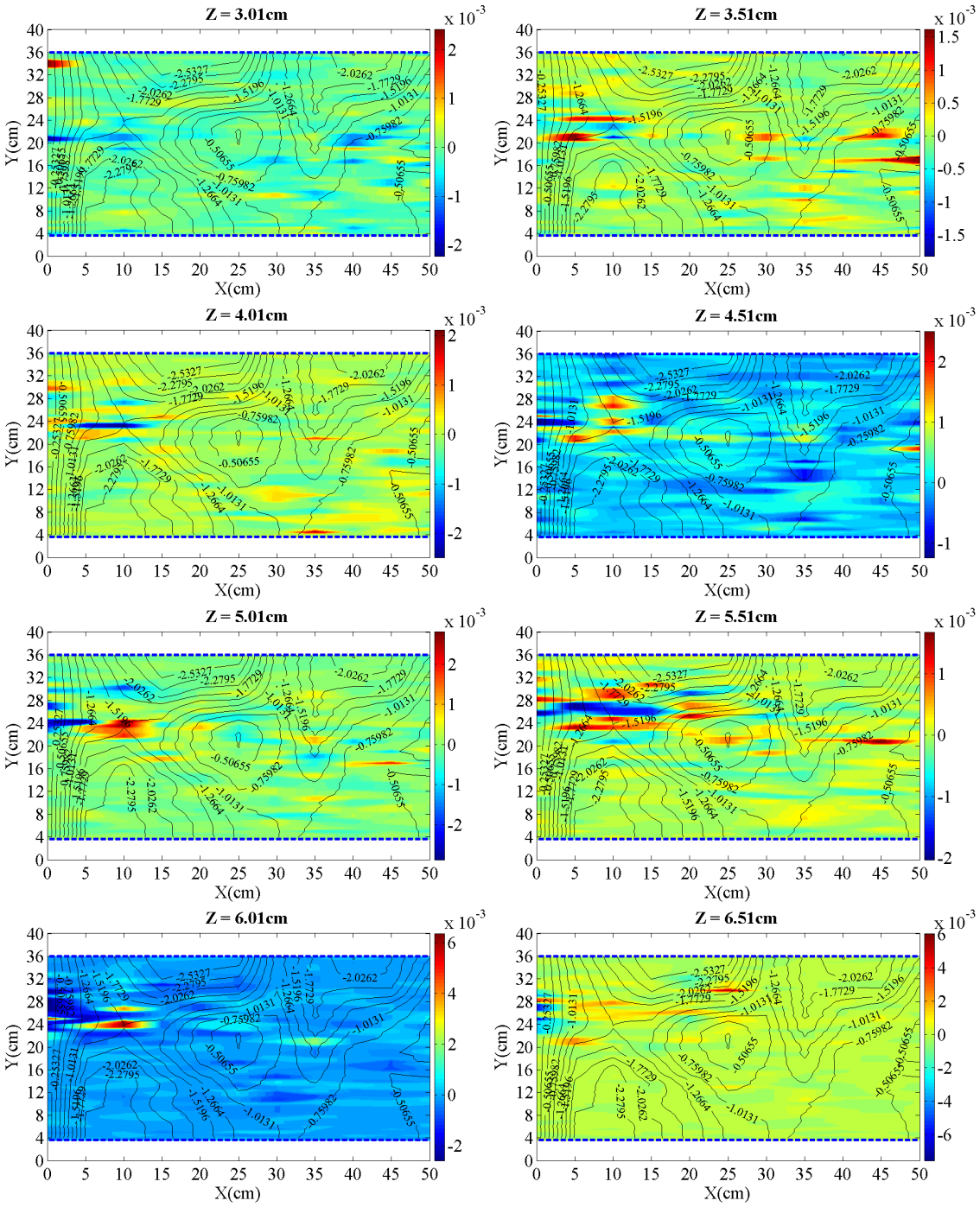

Figure 6.11 – Horizontal contour maps of $\overline{u'_x u'_y}$ (m^2/s^2): b) -3.01cm < Z <6.51cm.

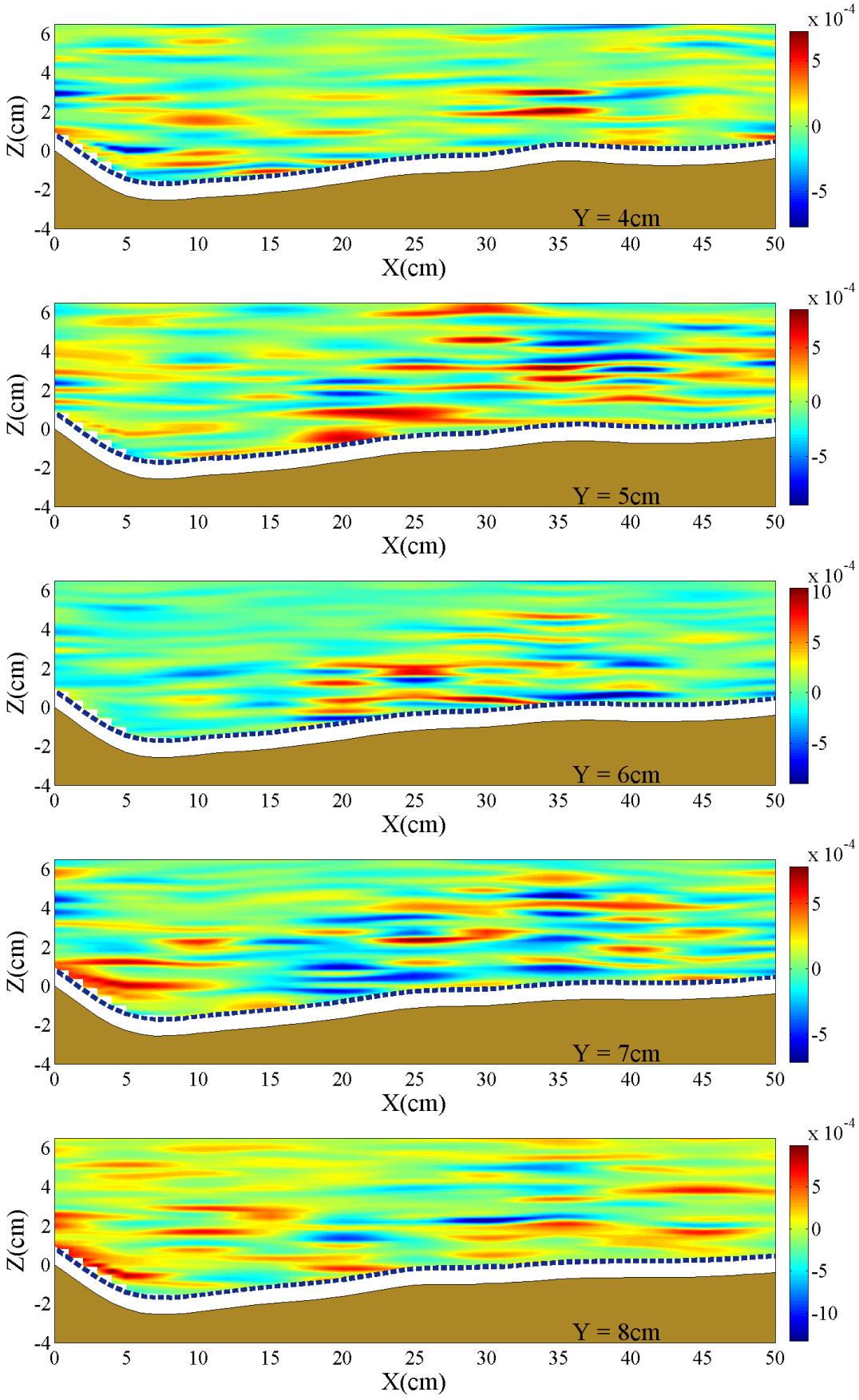

Figure 6.12 – Longitudinal contour maps of $\overline{u'_x u'_y}$ (m^2/s^2): a) 4cm < Y < 8cm.

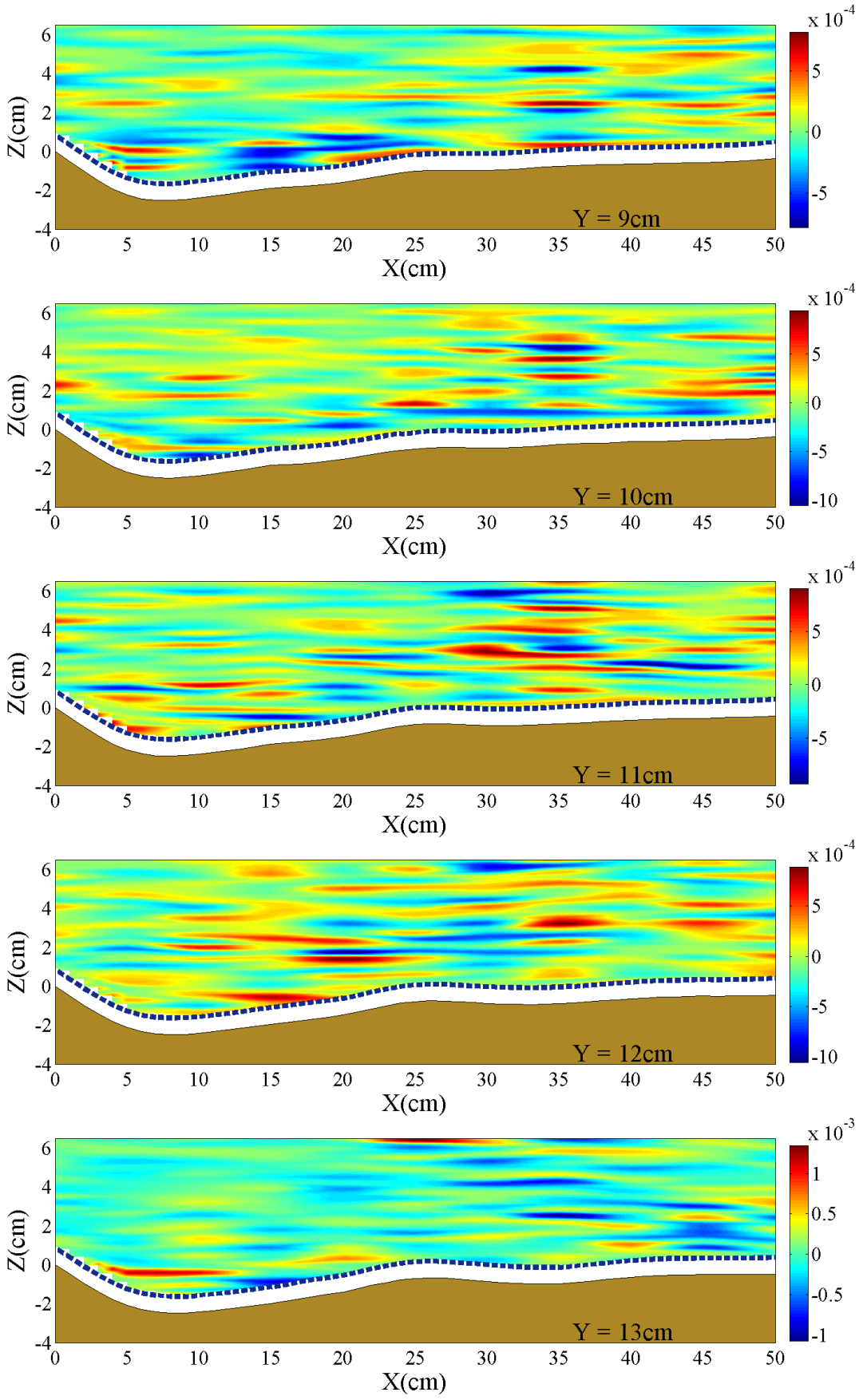

Figure 6.12 – Longitudinal contour maps of $\overline{u'_x u'_y}$ (m^2/s^2): b) 9cm < Y < 13cm.

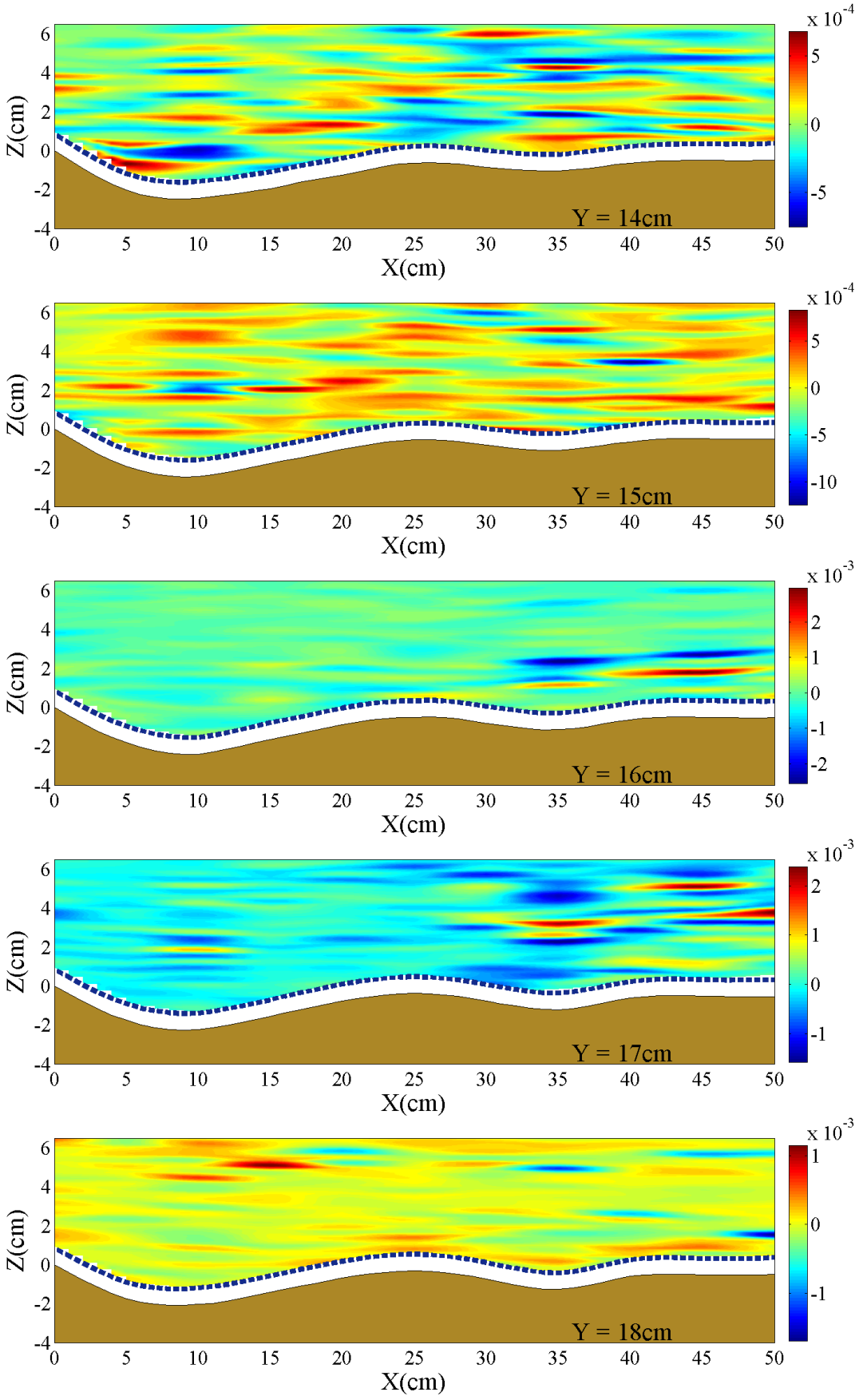

Figure 6.12 – Longitudinal contour maps of $\overline{u'_x u'_y}$ (m^2/s^2): c) 14cm < Y < 18cm.

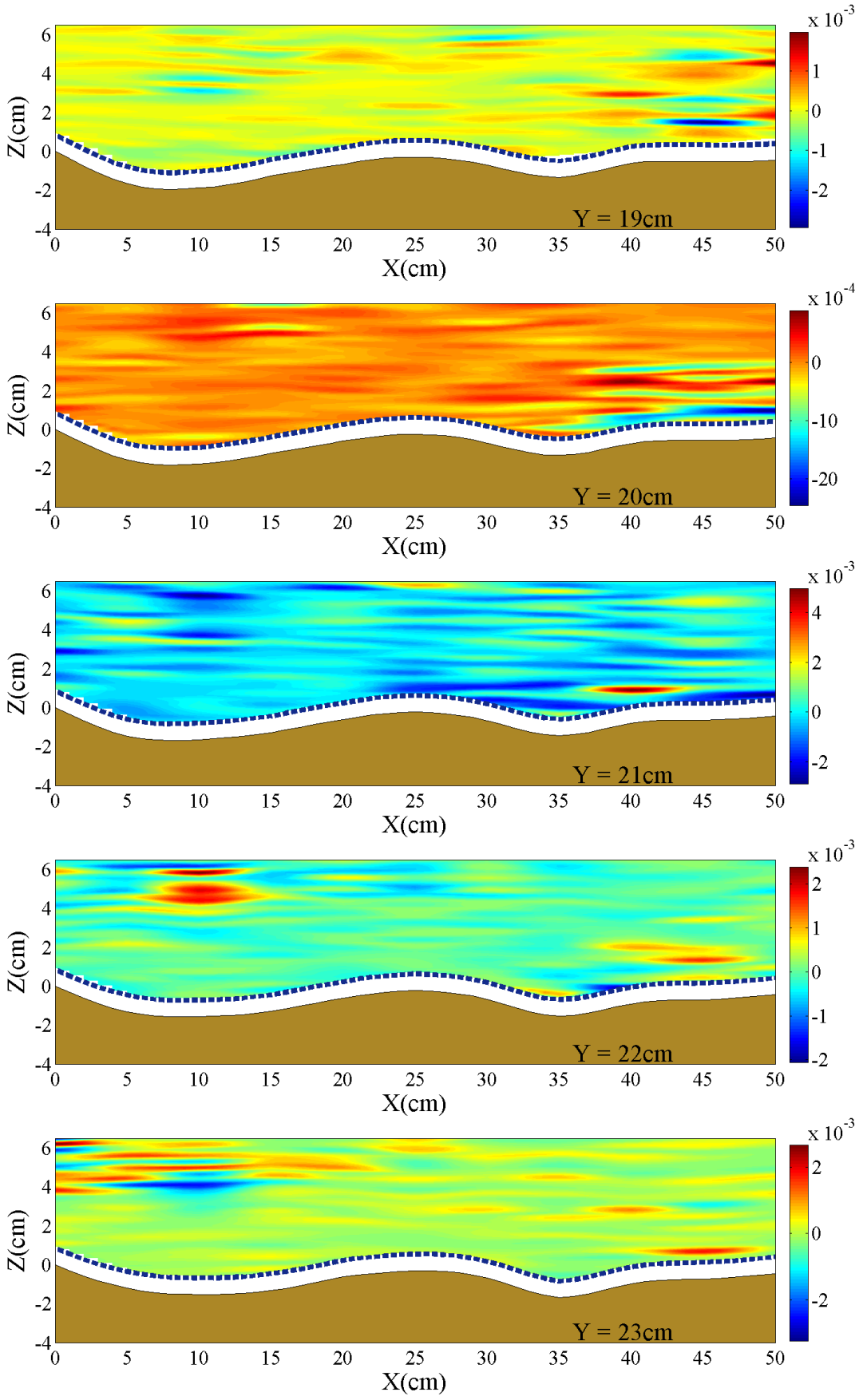

Figure 6.12 – Longitudinal contour maps of $\overline{u'_x u'_y}$ (m^2/s^2): d) 19cm < Y < 23cm.

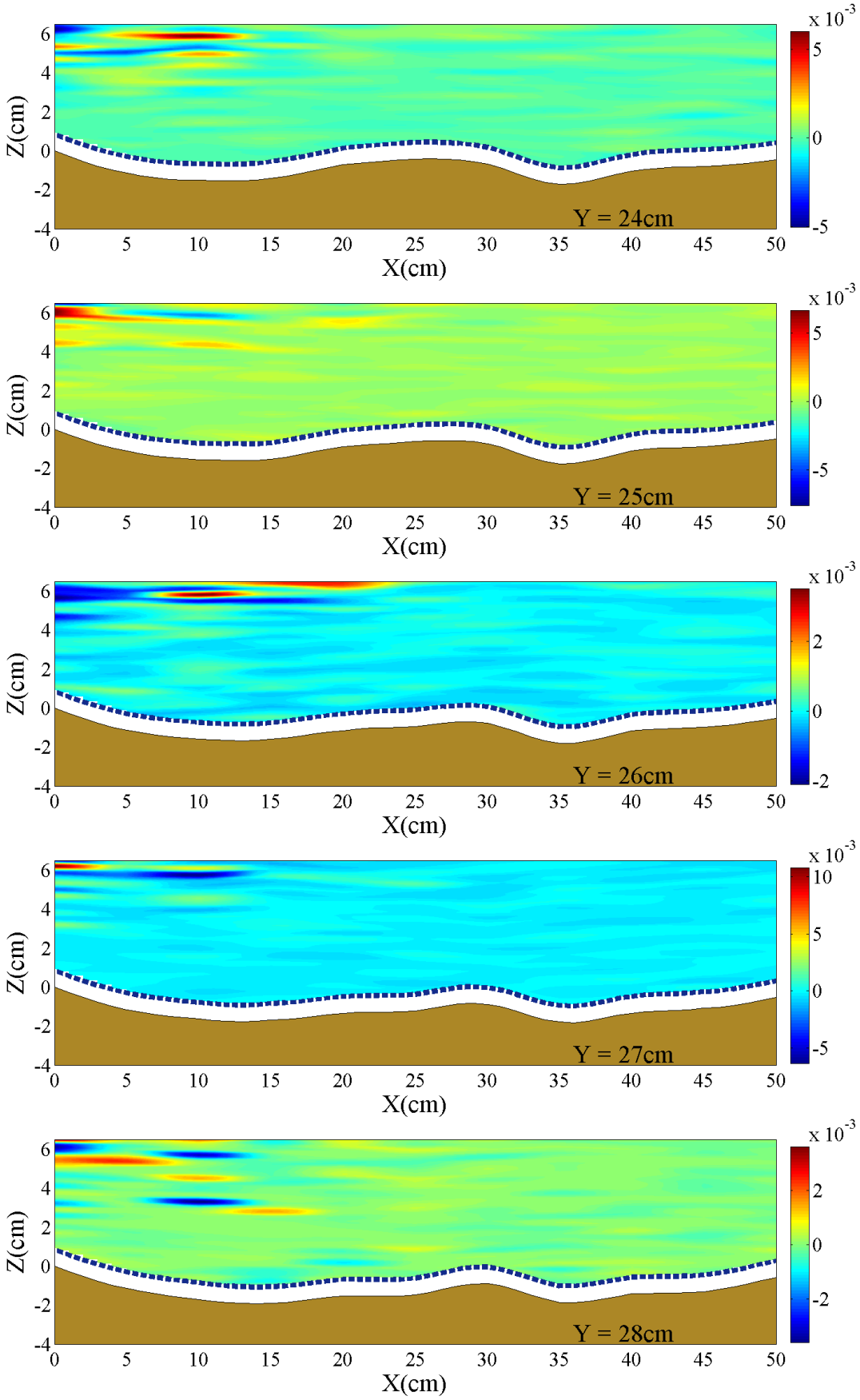

Figure 6.12 – Longitudinal contour maps of $\overline{u'_x u'_y}$ (m^2/s^2): e) 24cm < Y < 28cm.

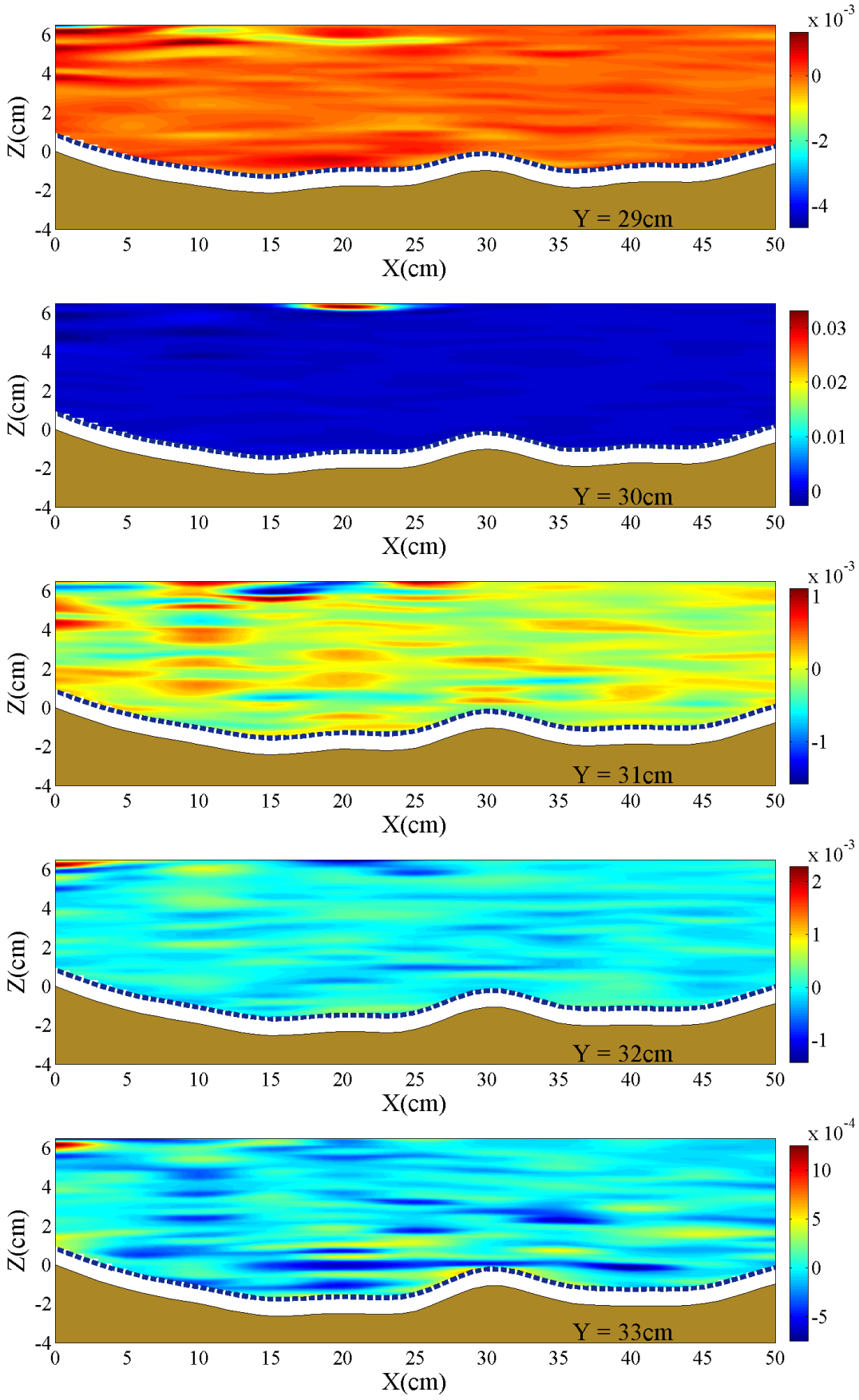

Figure 6.12 – Longitudinal contour maps of $\overline{u'_x u'_y}$ (m^2/s^2): f) 29cm < Y < 33cm.

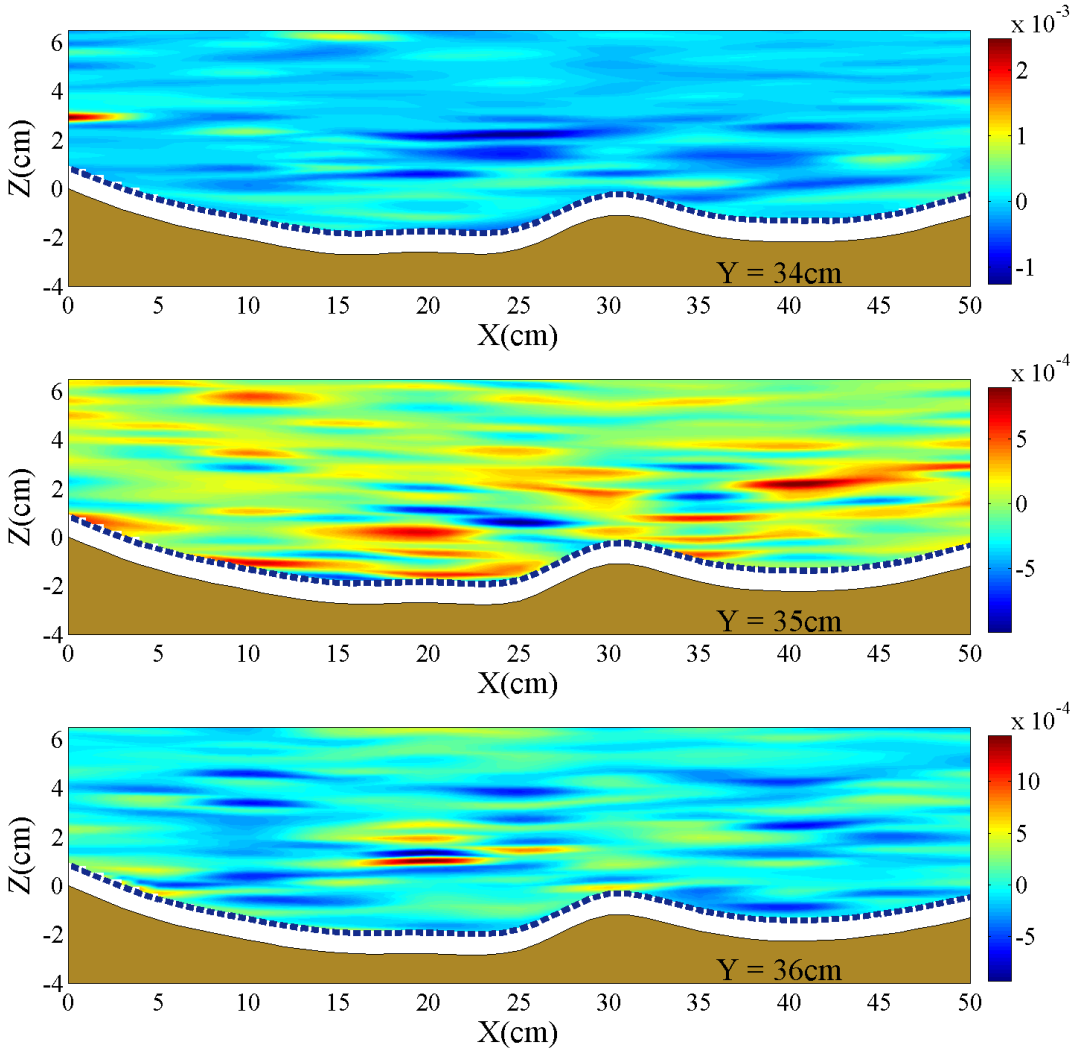

Figure 6.12 – Longitudinal contour maps of $\overline{u'_x u'_y}$ (m^2/s^2): g) 34cm < Y < 36cm.

- *Reynolds momentum flux* $\overline{u'_x u'_z}$

The transversal distributions of the Reynolds momentum flux $\overline{u'_x u'_z}$ are reported in Figure 6.13. This figure shows that the pattern of $\overline{u'_x u'_z}$ is similar to that of the component $\overline{u'_x u'_x}$ observed in Figure 6.1. In particular, high values of $\overline{u'_x u'_z}$ are found in the scour holes of all the examined sections.

The horizontal contour maps of $\overline{u'_x u'_z}$, are reported in Figure 6.14. Near the bed (Z < 0, see Figure 6.14a) negative values of $\overline{u'_x u'_z}$ occur for X < X30 within the near-bank regions and positive values of $\overline{u'_x u'_z}$ are especially found near the channel axis (18 cm < Y < 25 cm) and for X>X40. Moving towards the free surface (Z > 3.01 cm, see Figure 6.14b) positive peak values of $\overline{u'_x u'_z}$ occur at the channel axis and downstream of the central sand deposit (X > X35).

Finally, the longitudinal distributions of $\overline{u'_x u'_z}$ (reported in Figure 6.15) show that near the right bank (Y < 18cm, see Figures 6.15a-c) $\overline{u'_x u'_z}$ assumes high negative values near the bed. At the channel region (18cm < Y < 28cm, see Figures 6.15c-e), positive values of $\overline{u'_x u'_z}$ occur for X > 35cm. For 28cm < Y < 36cm (Figures 6.15f-g) $\overline{u'_x u'_z}$ increases again near inside the scour hole (for X < X30), assuming a pattern similar to that observed near the right bank (Y < 18cm). Thus, the highest values of momentum flux occur where the scour hole develops.

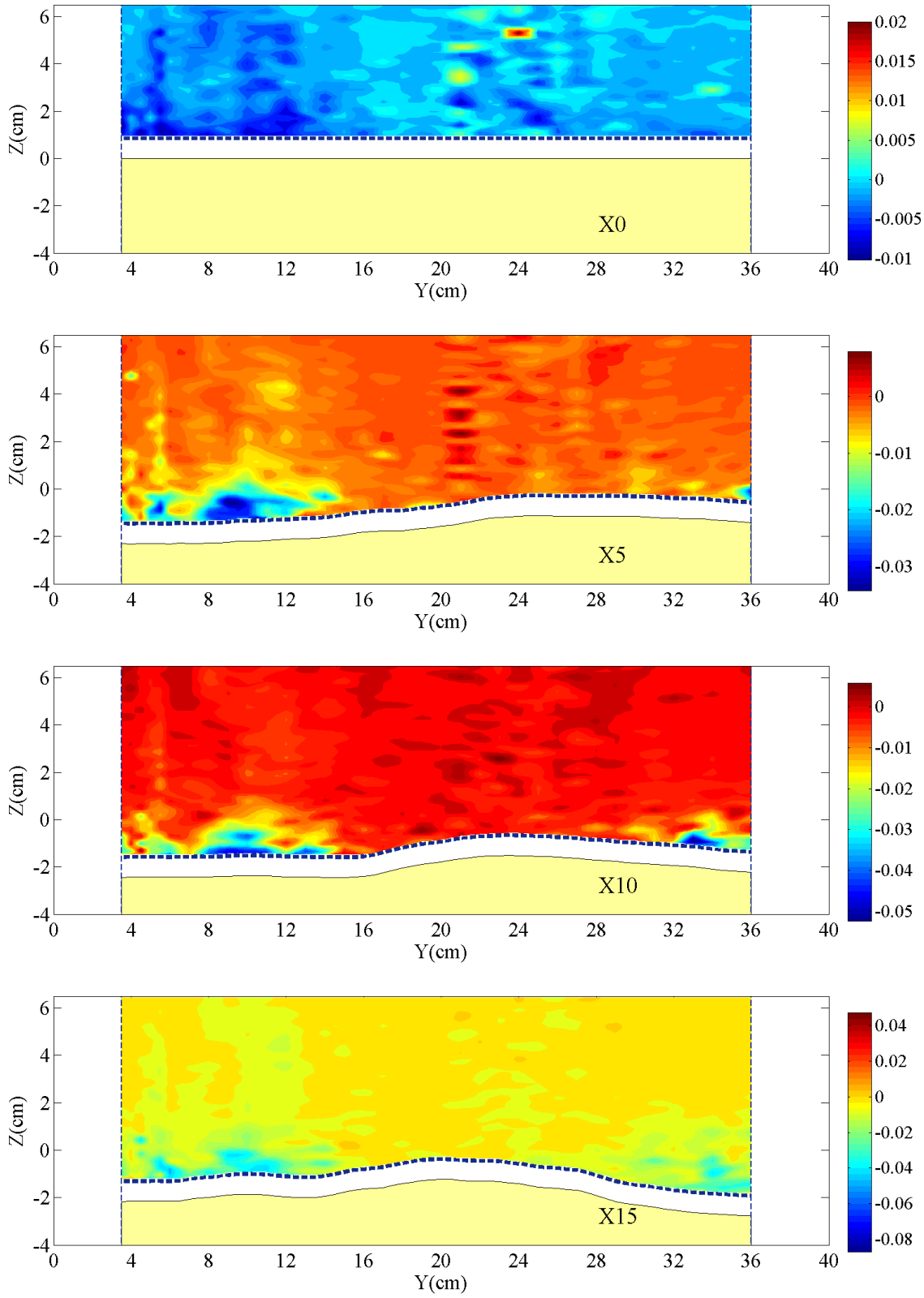

Figure 6.13 – Contour maps of $\overline{u_x' u_z'}$ (m^2/s^2): a) X0 < X < X15.

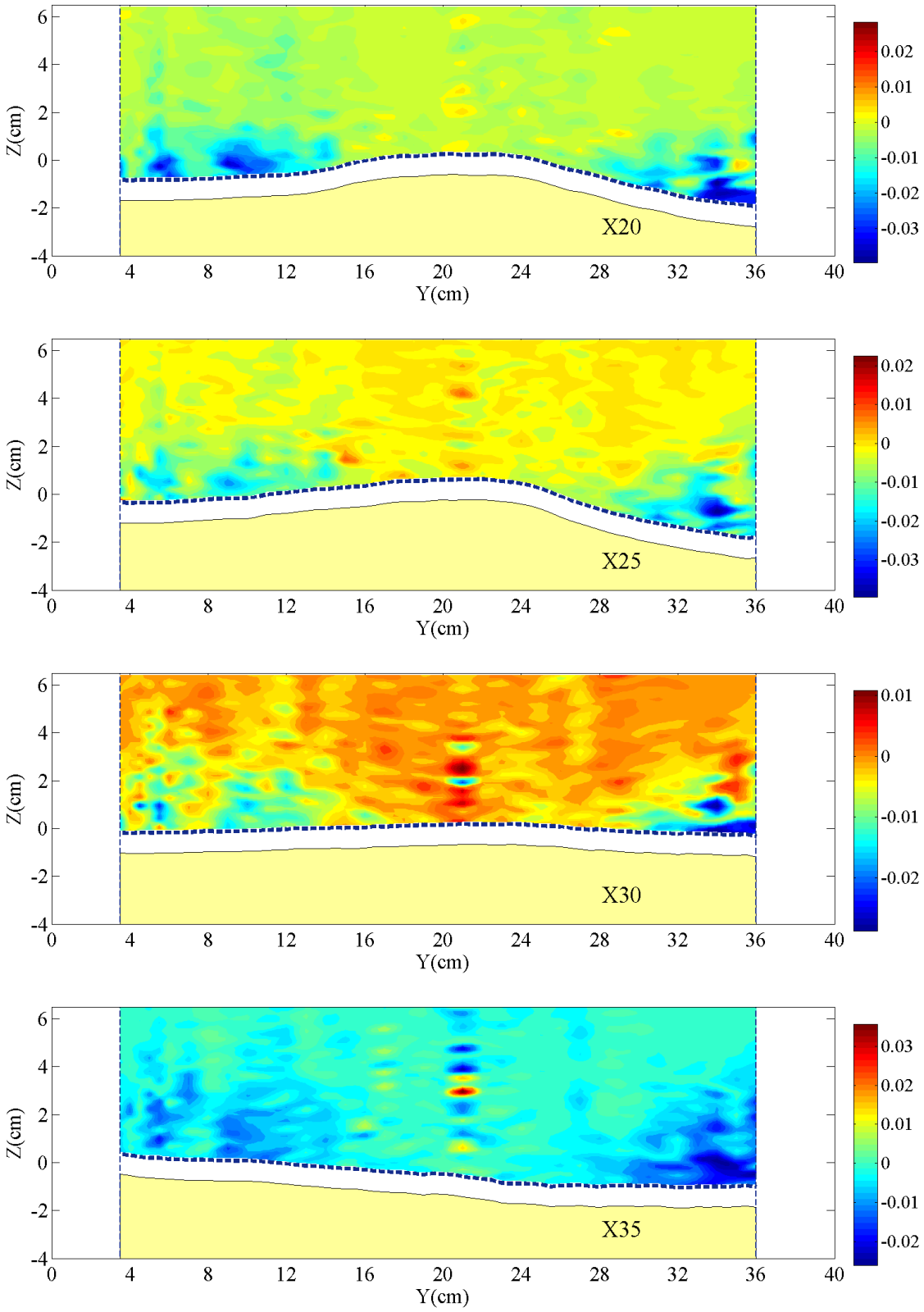

Figure 6.13 – Contour maps of $\overline{u_x' u_z'}$ (m^2/s^2): b) X20 < X < X35.

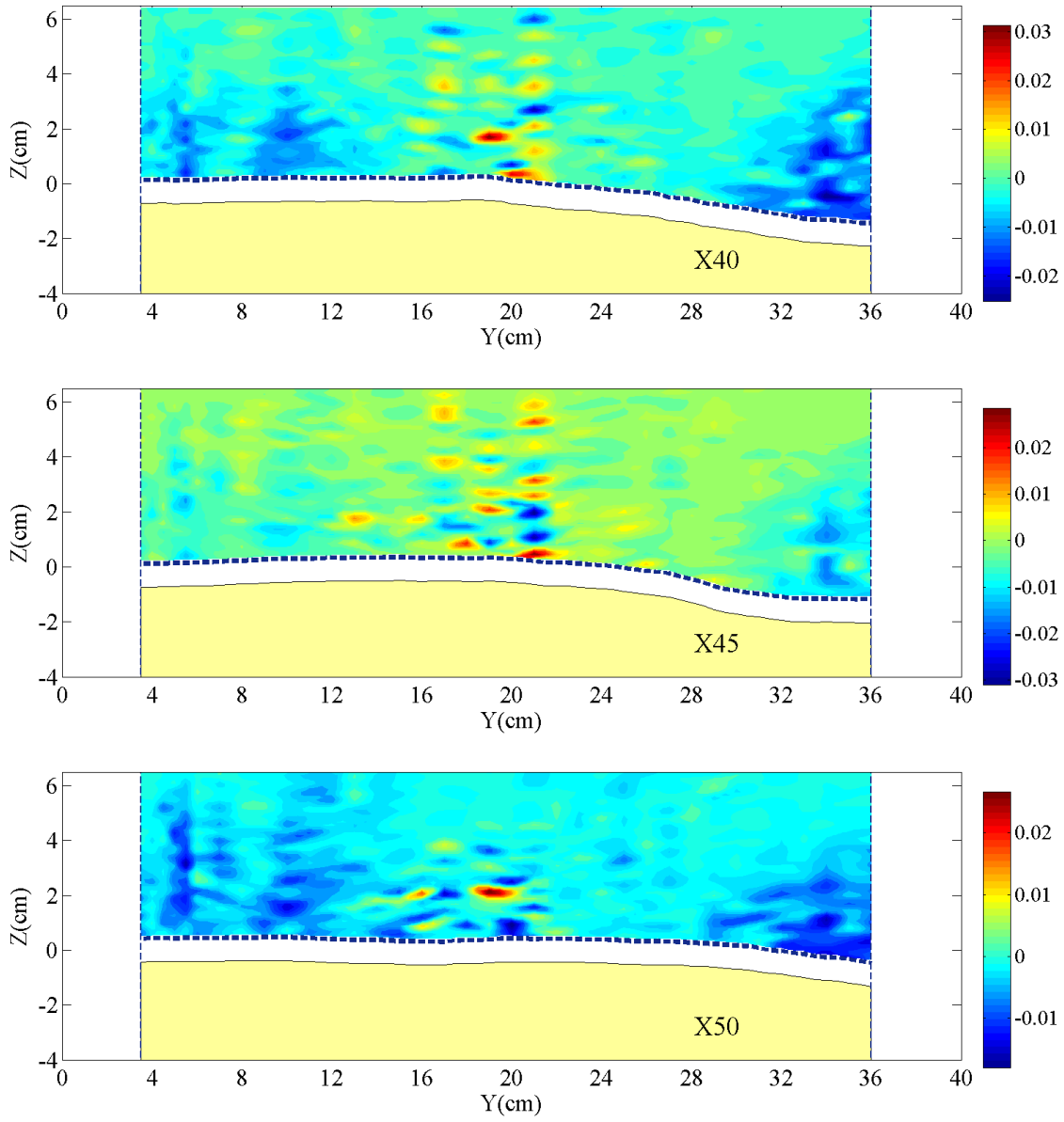

Figure 6.13 – Contour maps of $\overline{u_x' u_z'}$ (m^2/s^2): c) X40 < X < X50.

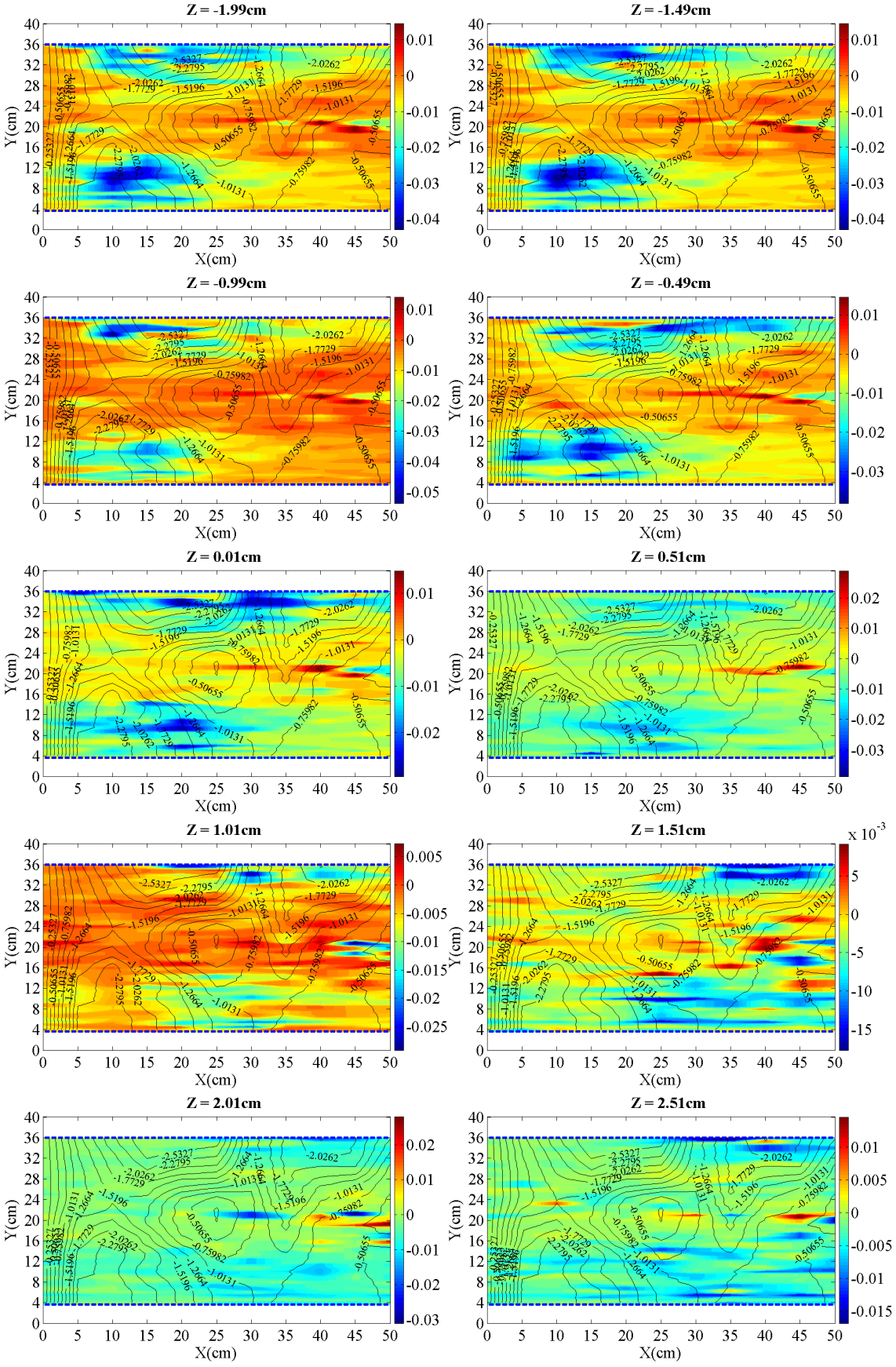

Figure 6.14 – Horizontal contour maps of $\overline{u'_x u'_z}$ (m^2/s^2): a) -1.99cm < Z < 2.51cm.

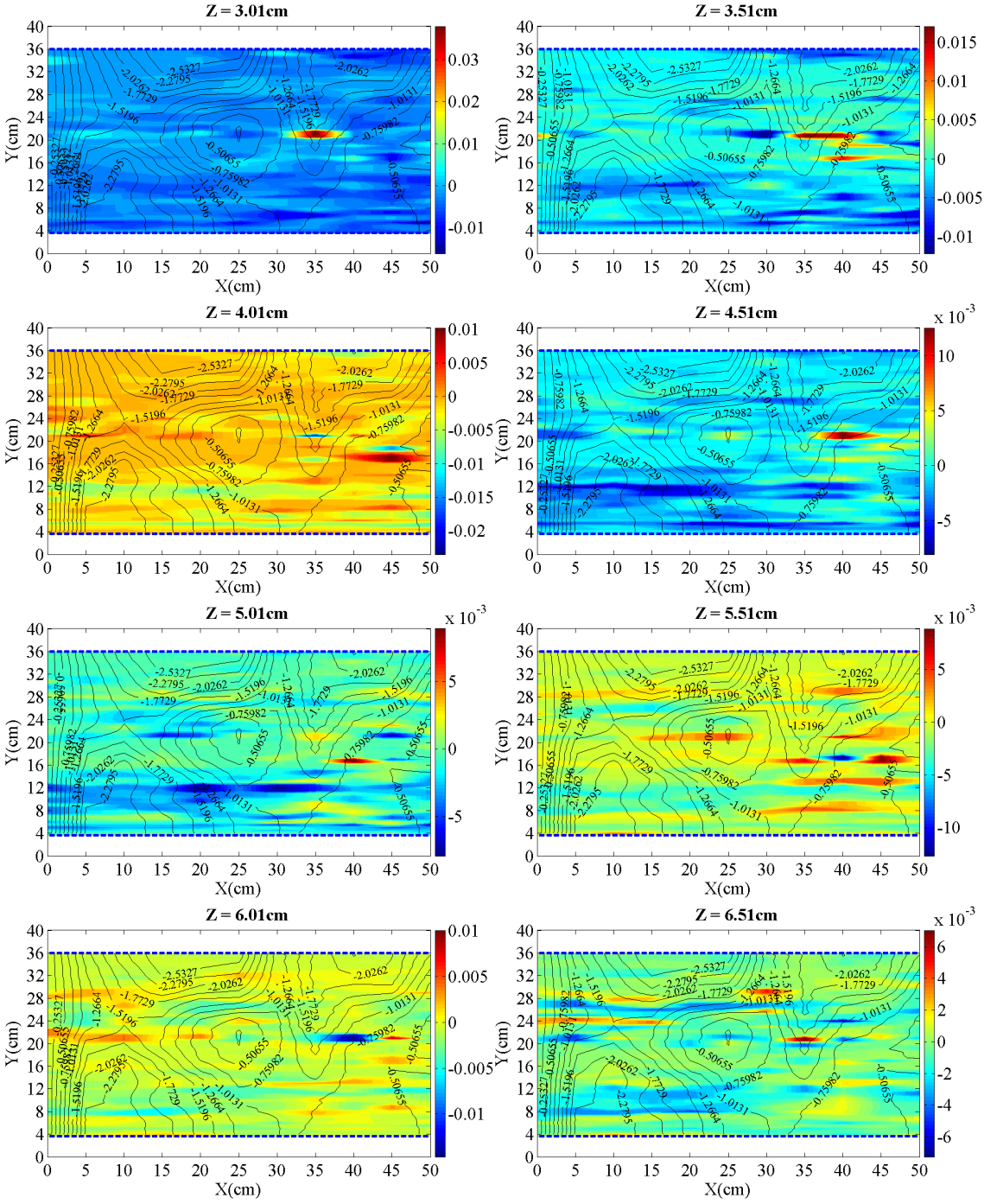

Figure 6.14 – Horizontal contour maps of $\overline{u'_x u'_z}$ (m^2/s^2): b) -3.01 cm < Z < 6.51cm.

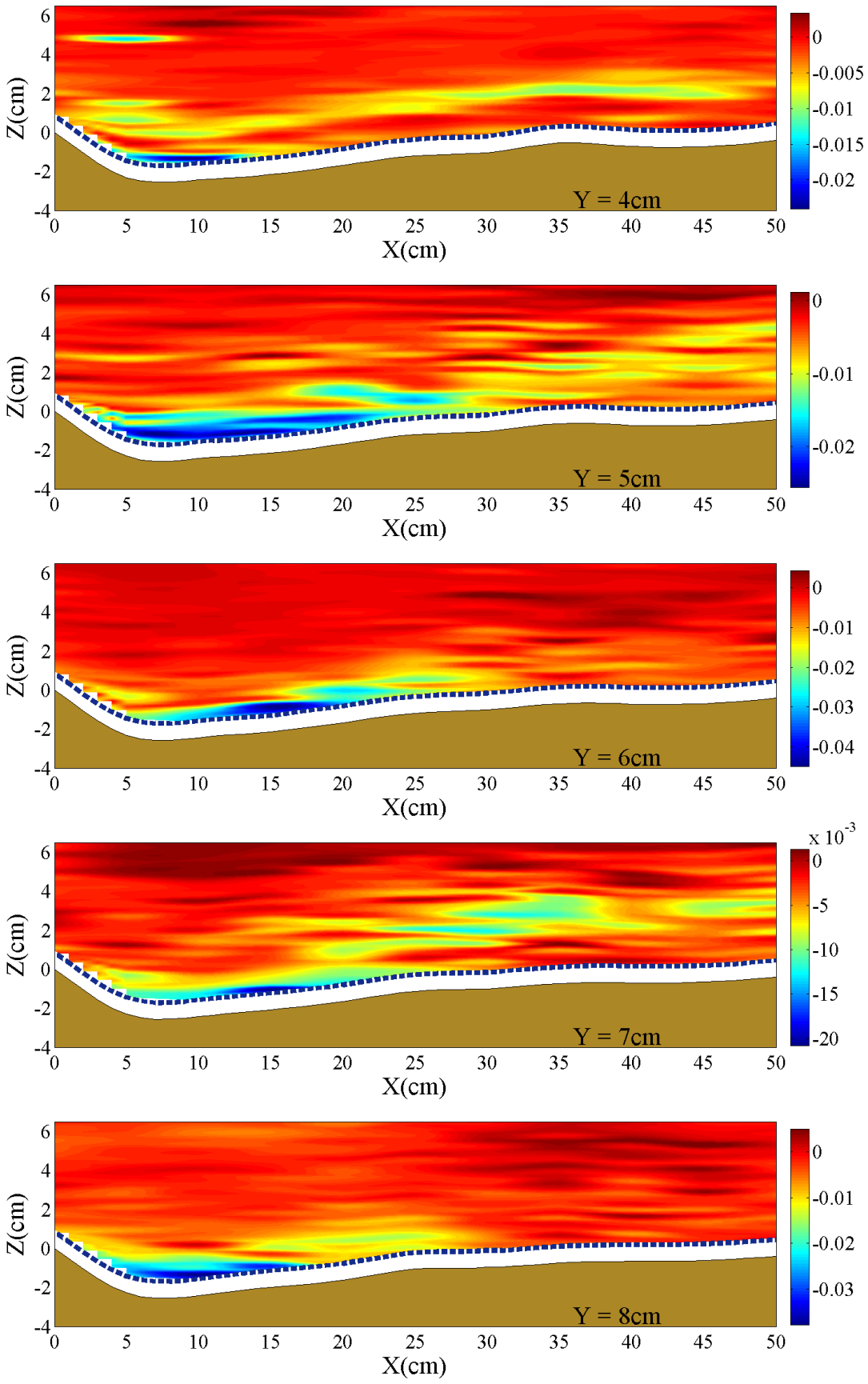

Figure 6.15 – Longitudinal contour maps of $\overline{u_x' u_z'}$ (m^2/s^2): a) 4cm < Y < 8cm.

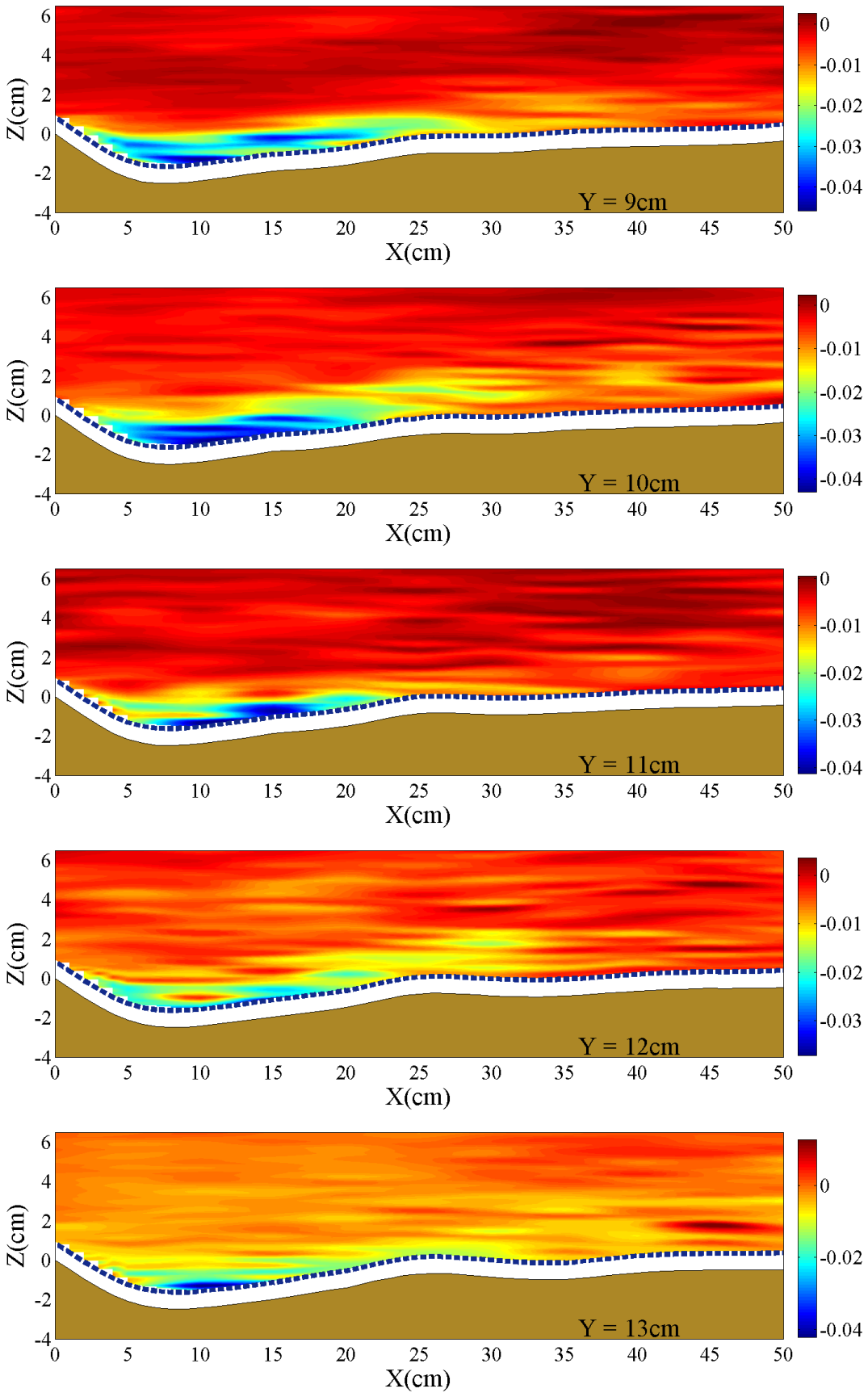

Figure 6.15 – Longitudinal contour maps of $\overline{u_x' u_z'}$ (m^2/s^2): b) 9cm < Y < 13cm.

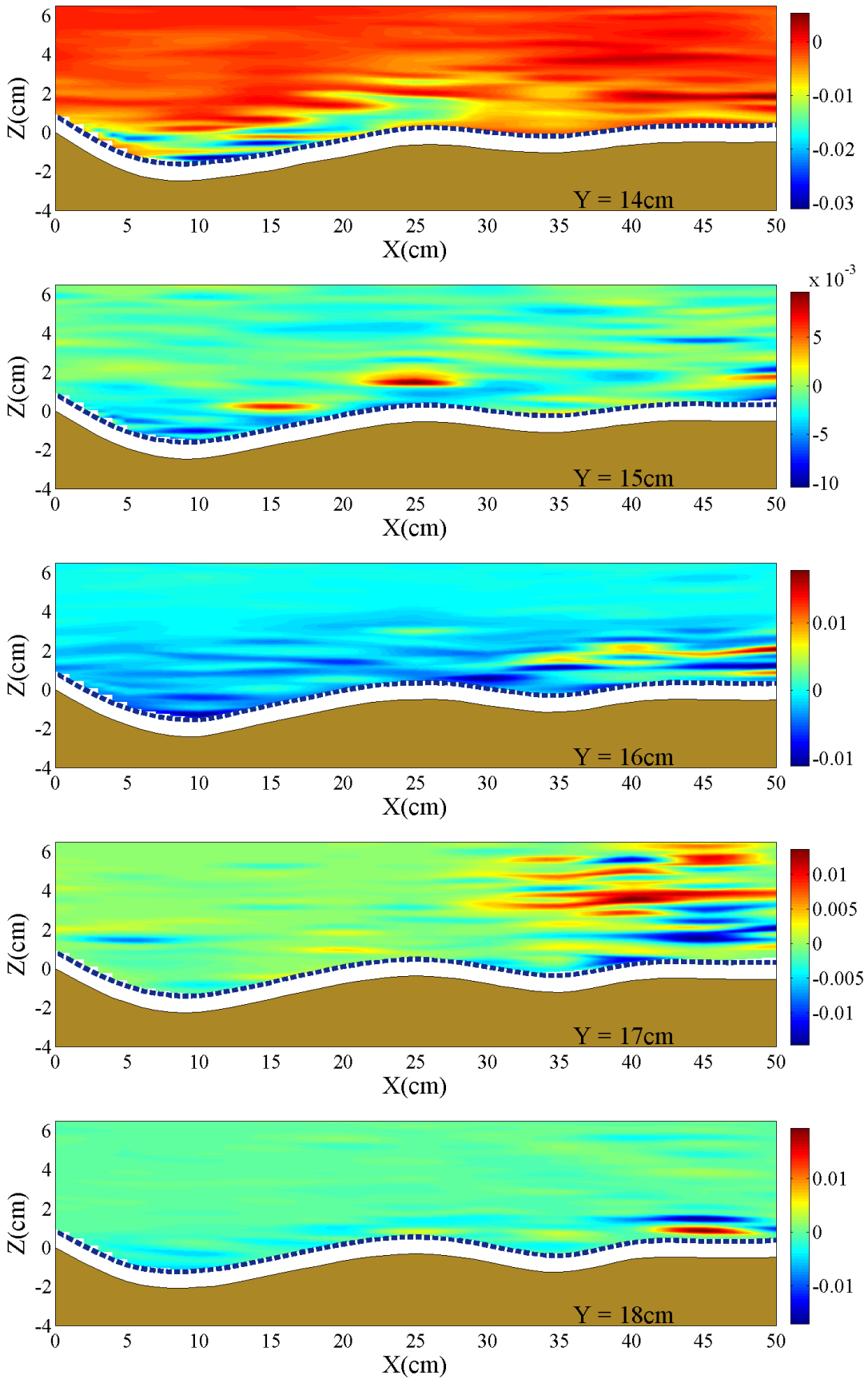

Figure 6.15 – Longitudinal contour maps of $\overline{u'_x u'_z}$ (m^2/s^2): c) 14cm < Y < 18cm.

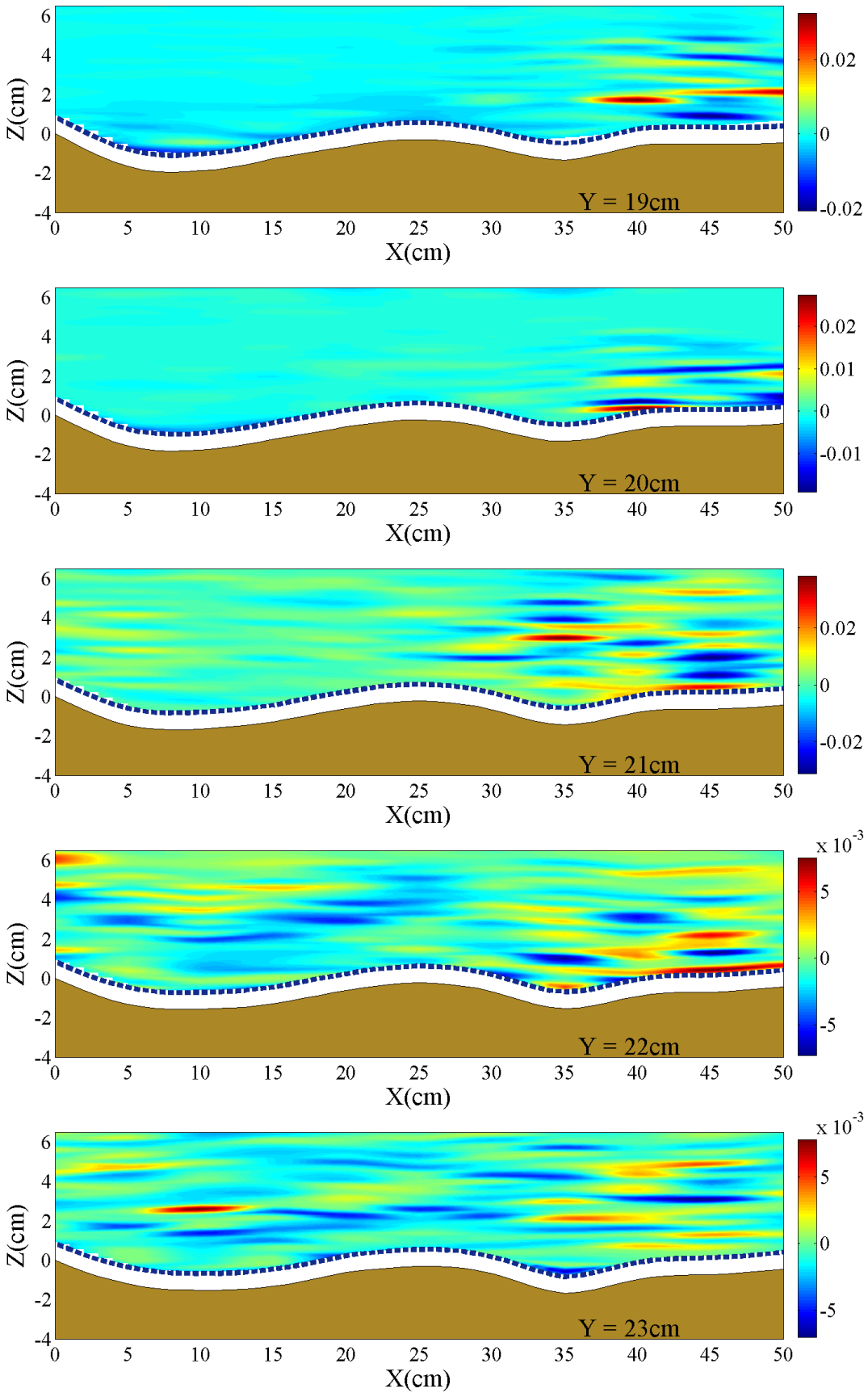

Figure 6.15 – Longitudinal contour maps of $\overline{u'_x u'_z}$ (m^2/s^2): d) 19cm < Y < 23cm.

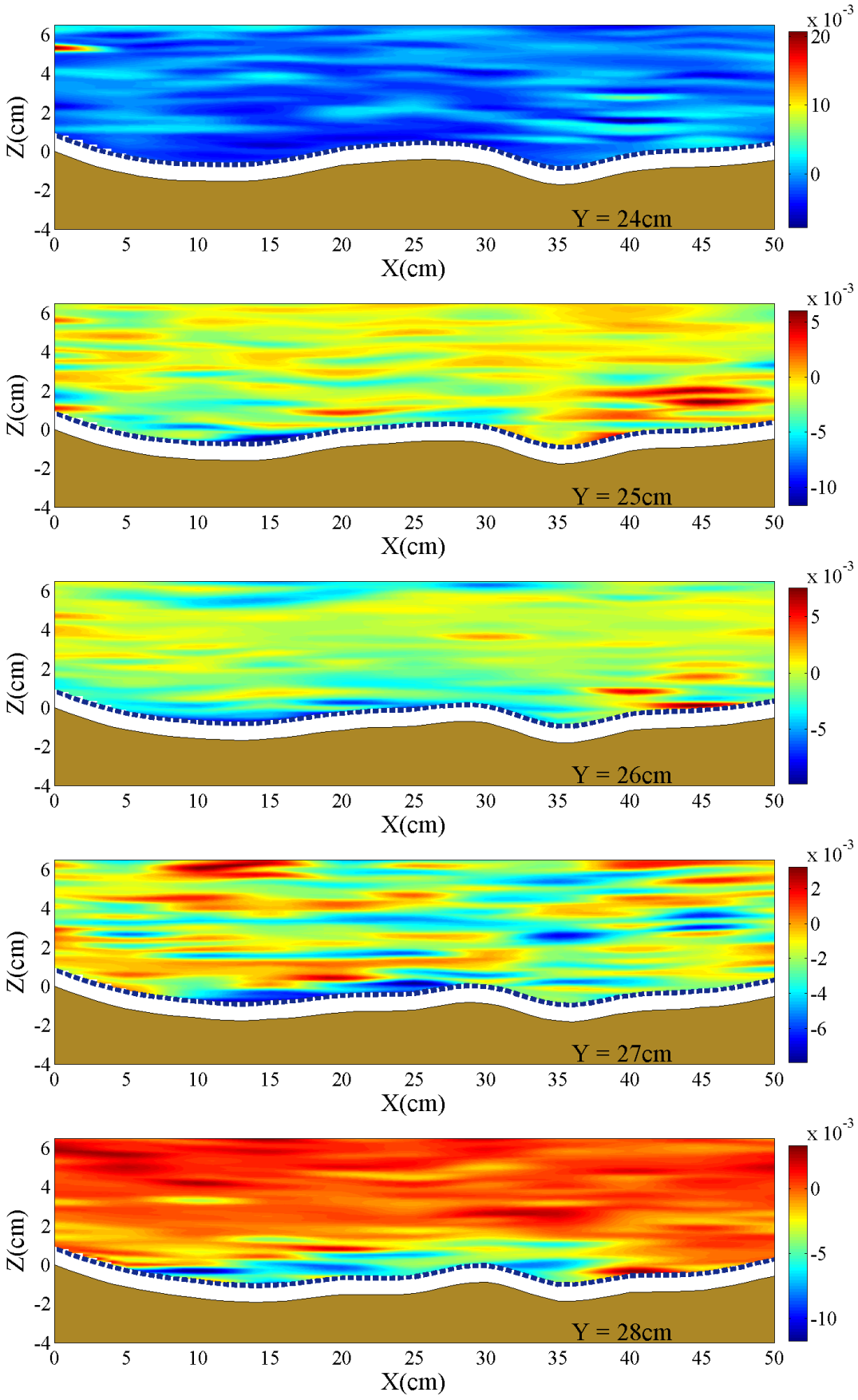

Figure 6.15 – Longitudinal contour maps of $\overline{u'_x u'_z}$ (m^2/s^2): e) 24cm < Y < 28cm.

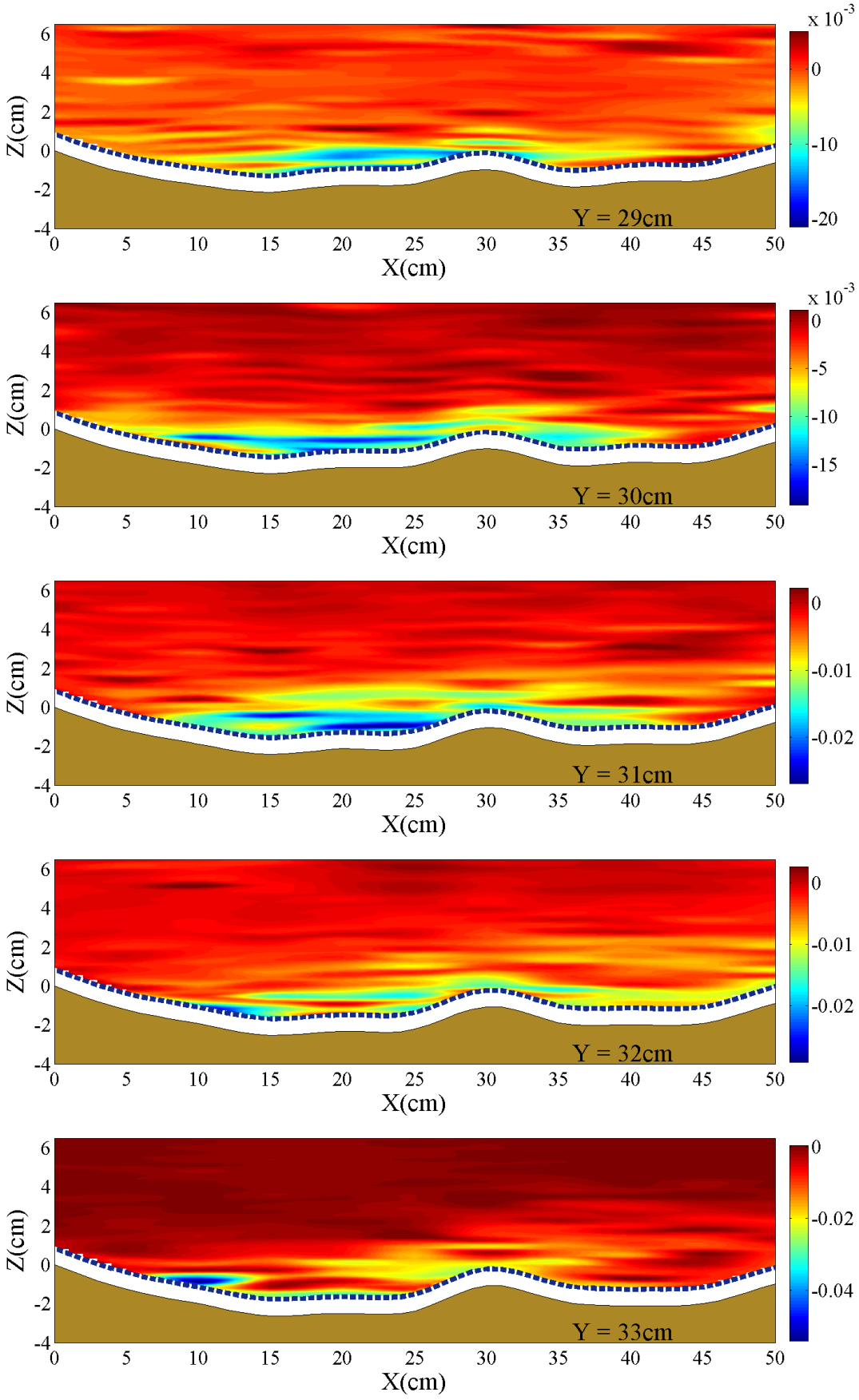

Figure 6.15 – Longitudinal contour maps of $\overline{u_x' u_z'}$ (m^2/s^2): f) 29cm < Y < 33cm.

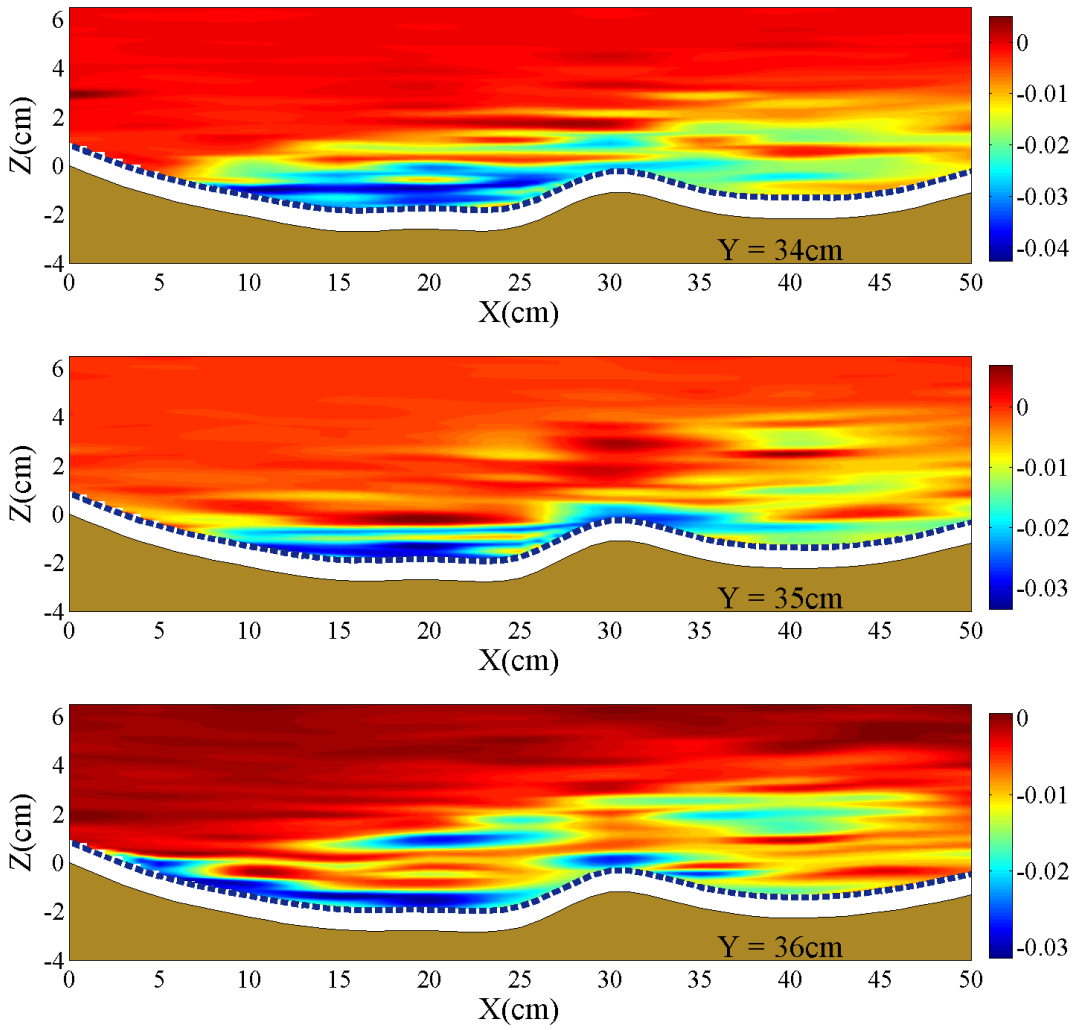

Figure 6.15 – Longitudinal contour maps of $\overline{u'_x u'_z}$ (m^2/s^2): g) 34cm < Y < 36cm.

– *Reynolds momentum flux* $\overline{u'_y u'_z}$

The transversal distributions of $\overline{u'_y u'_z}$ are reported in Figure 6.16. From section X0 to section X10 the transversal distribution of $\overline{u'_y u'_z}$ shows high values near the free surface for 20cm < Y < 30cm. The momentum flux $\overline{u'_y u'_z}$ assumes both negative and positive values. The horizontal distributions of $\overline{u'_y u'_z}$ are reported in Figure 6.17. Near the bed high values are located at the channel axis and for X > X40. Particularly, near the bed, at Z < 0cm (see Figure 6.17a), some positive high values of $\overline{u'_y u'_z}$ are found for X = X10 ÷ X25 within the near-bank regions. Near the free surface (Z > 3.01cm, see Figure 6.17b) high positive values occur for X0 < X < X5 and close to the channel axis for Y = 20 ÷ 25cm.

The longitudinal distributions of $\overline{u'_y u'_z}$ are reported in Figure 6.18. Near the right bank, at Y = 4cm, the longitudinal distribution clearly show the alternating of positive and negative high values close to the bed inside the scour hole (X < X10). Other positive values occur downstream the deposition zone (at X > X35).

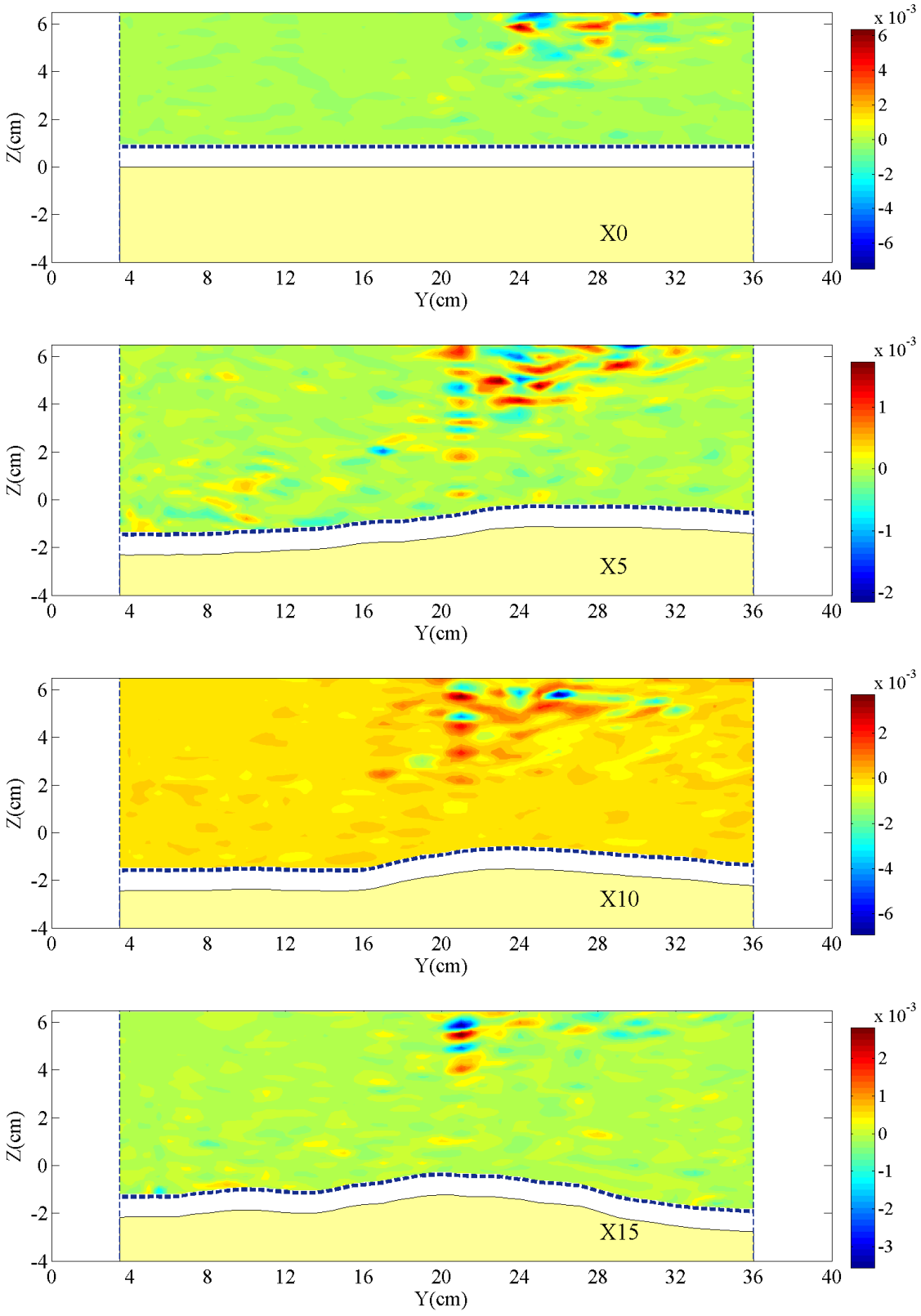

Figure 6.16 –Contour maps of $\overline{u'_y u'_z}$ (m^2/s^2): a) X0 < X < X15.

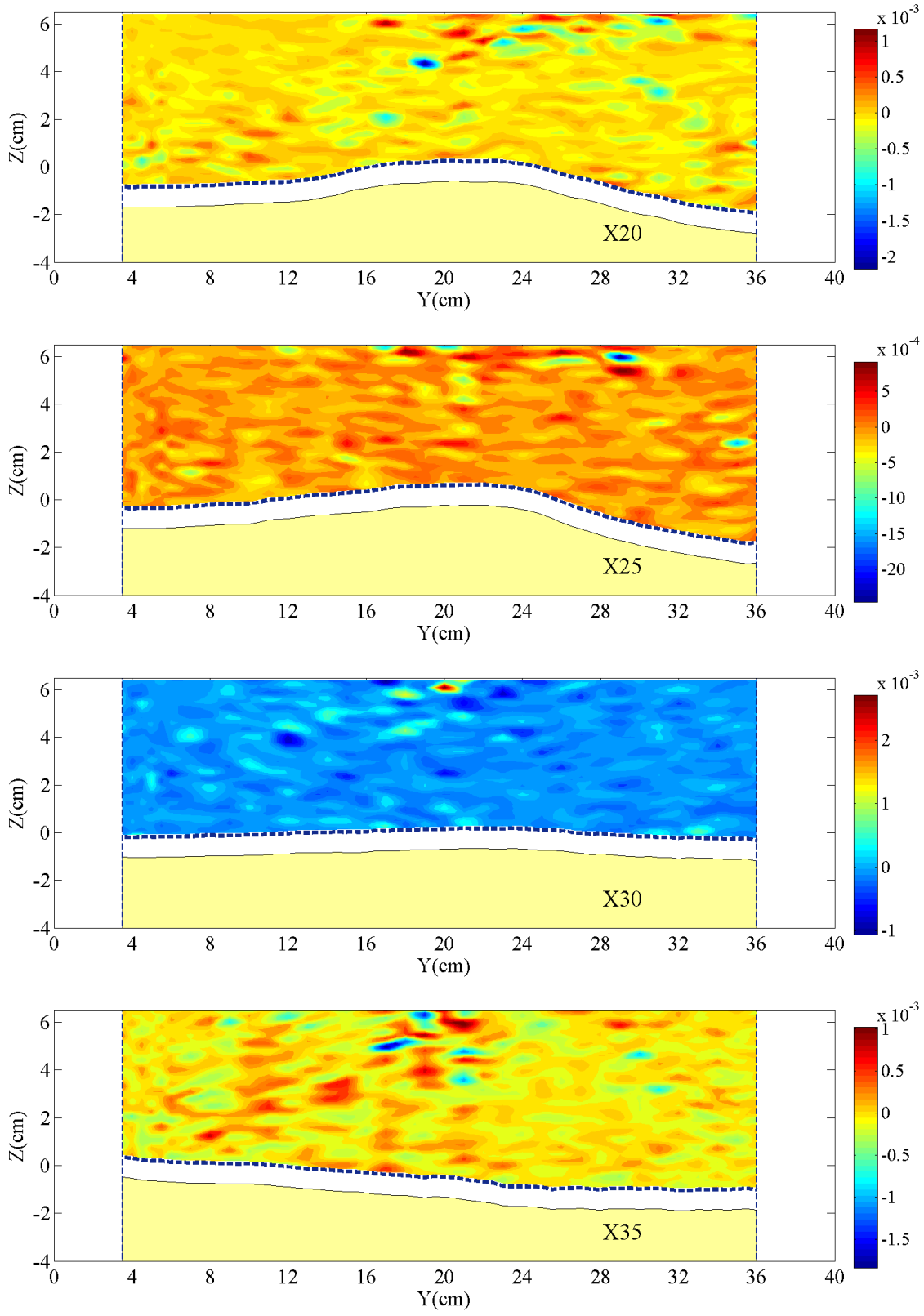

Figure 6.16 –Contour maps of $\overline{u'_y u'_z}$ (m^2/s^2): b) X20 < X < X35.

.

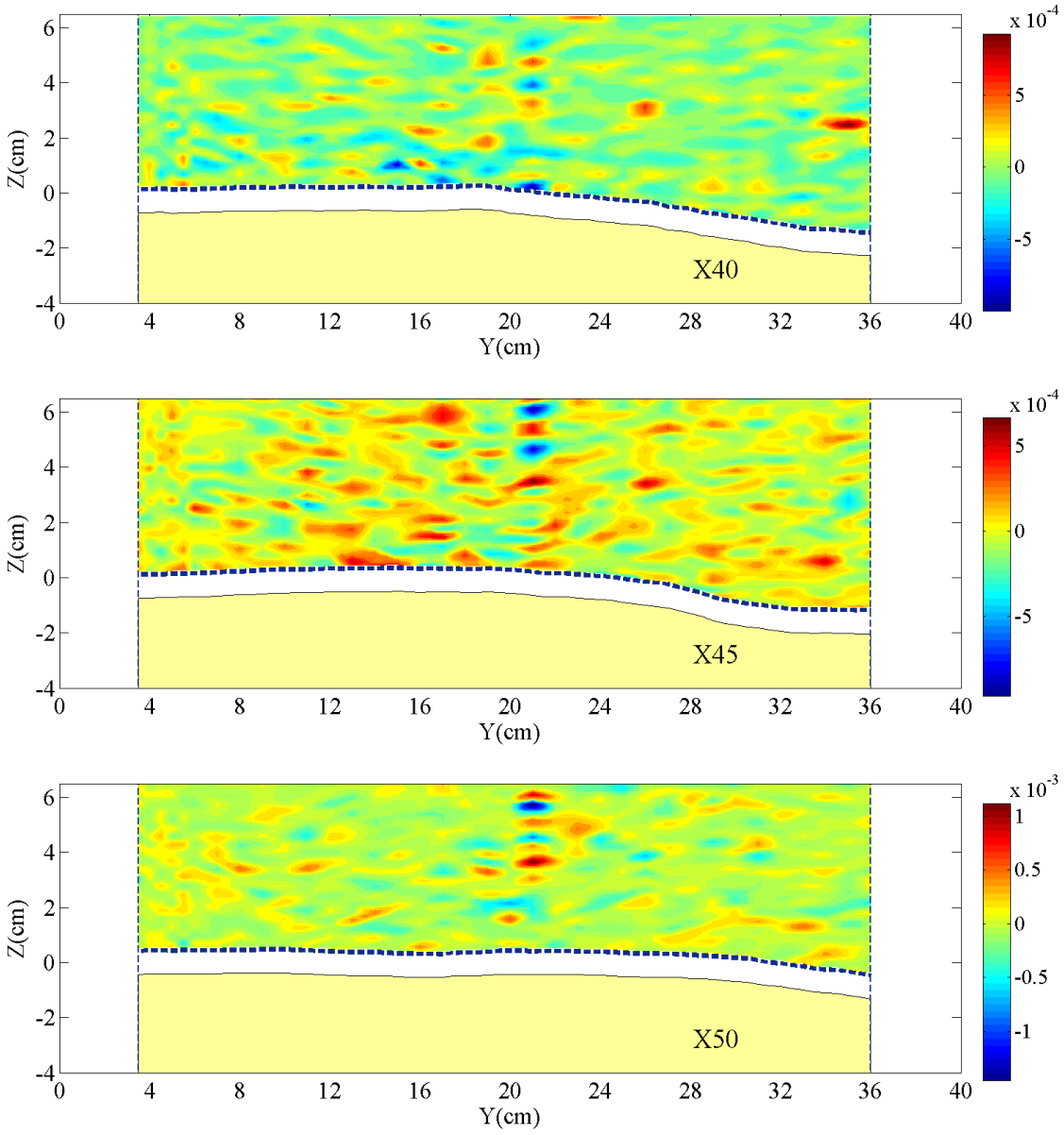

Figure 6.16 –Contour maps of $\overline{u'_y u'_z}$ (m^2/s^2): c) X40 < X < X50.

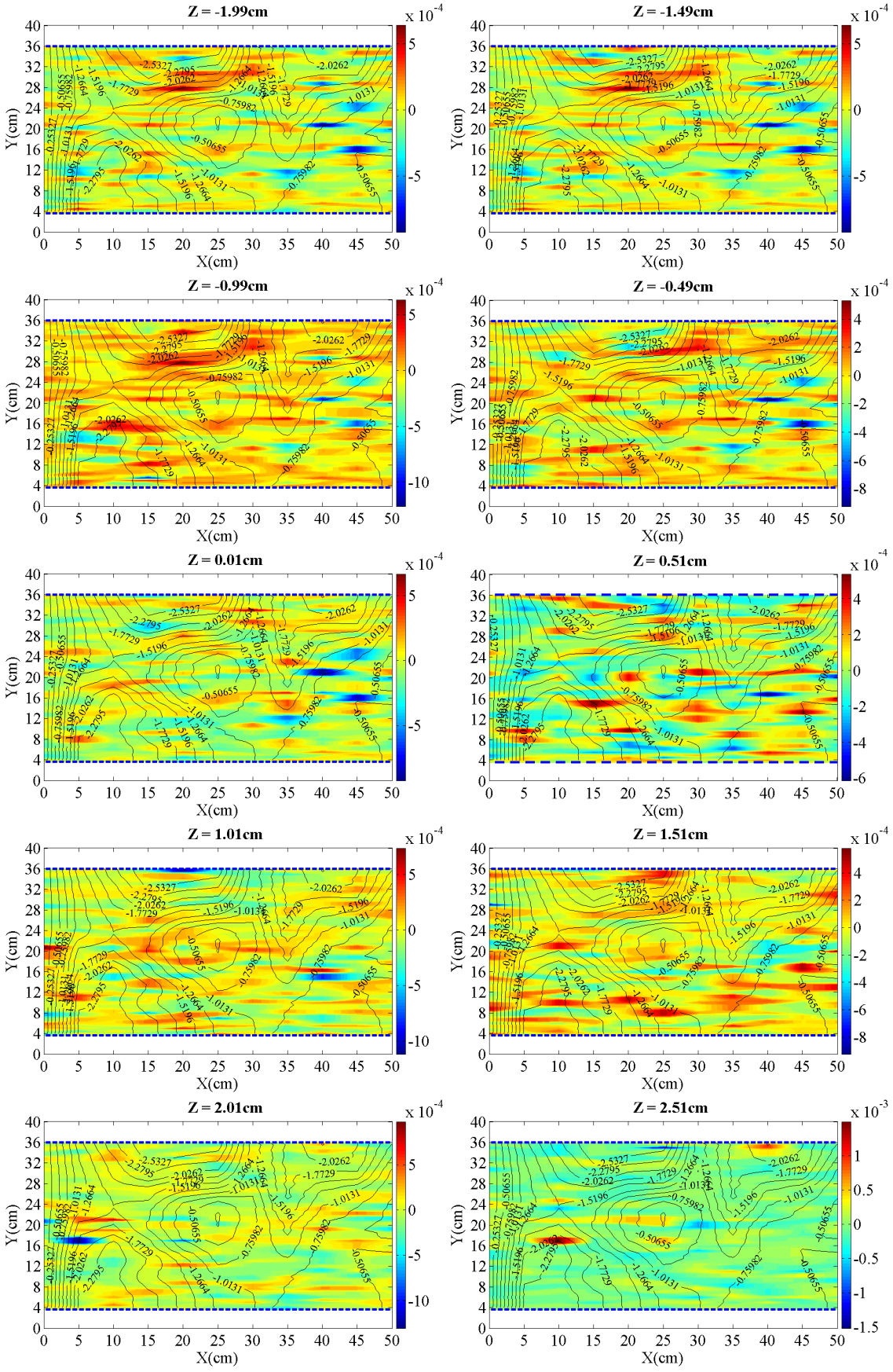

Figure 6.17 – Horizontal contour maps of $\overline{u'_y u'_z}$ (m^2/s^2): a) -1.99cm < Z < 2.51cm.

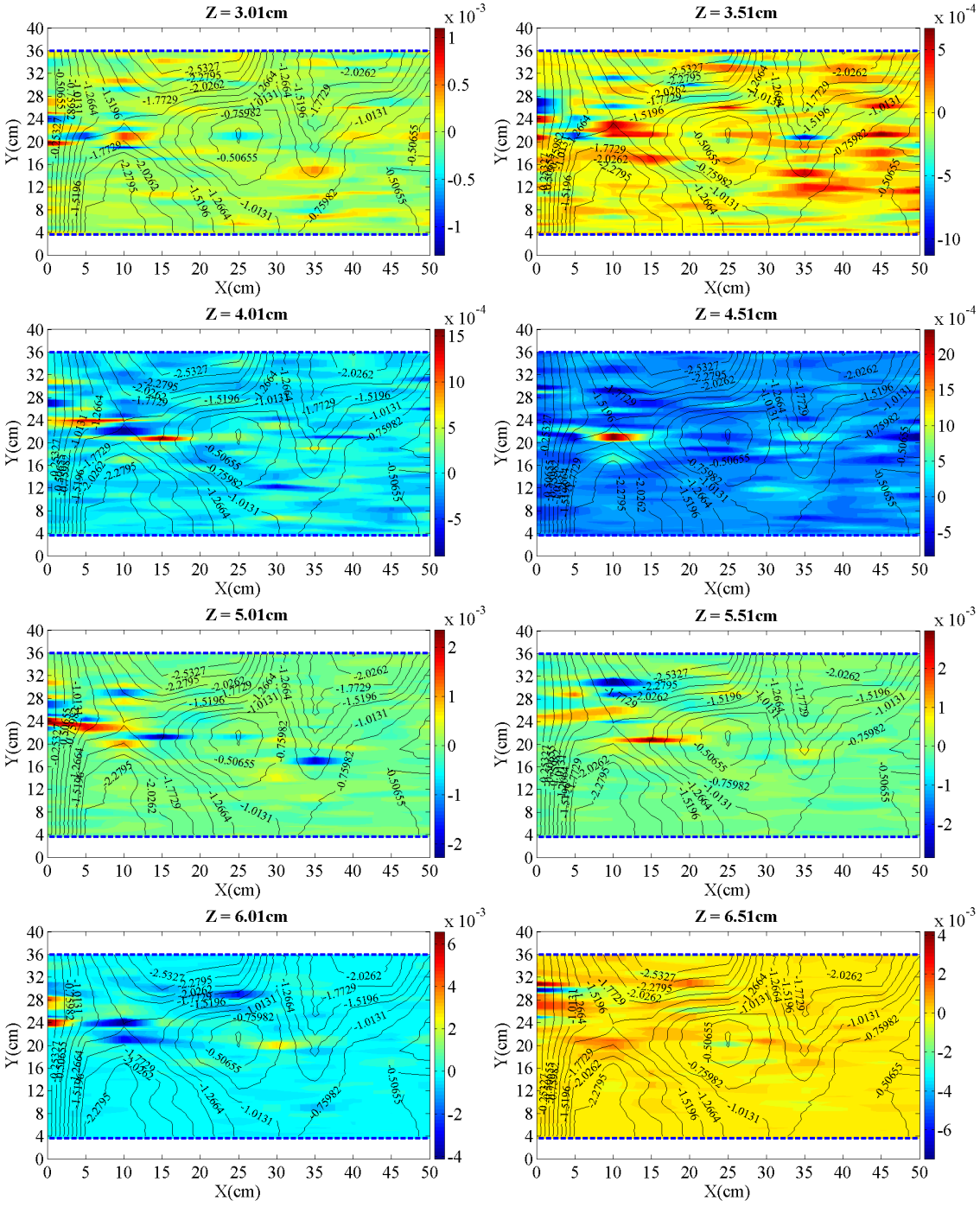

Figure 6.17 – Horizontal contour maps of $\overline{u'_y u'_z}$ (m^2/s^2): b) 3.01cm < Z < 6.51cm.

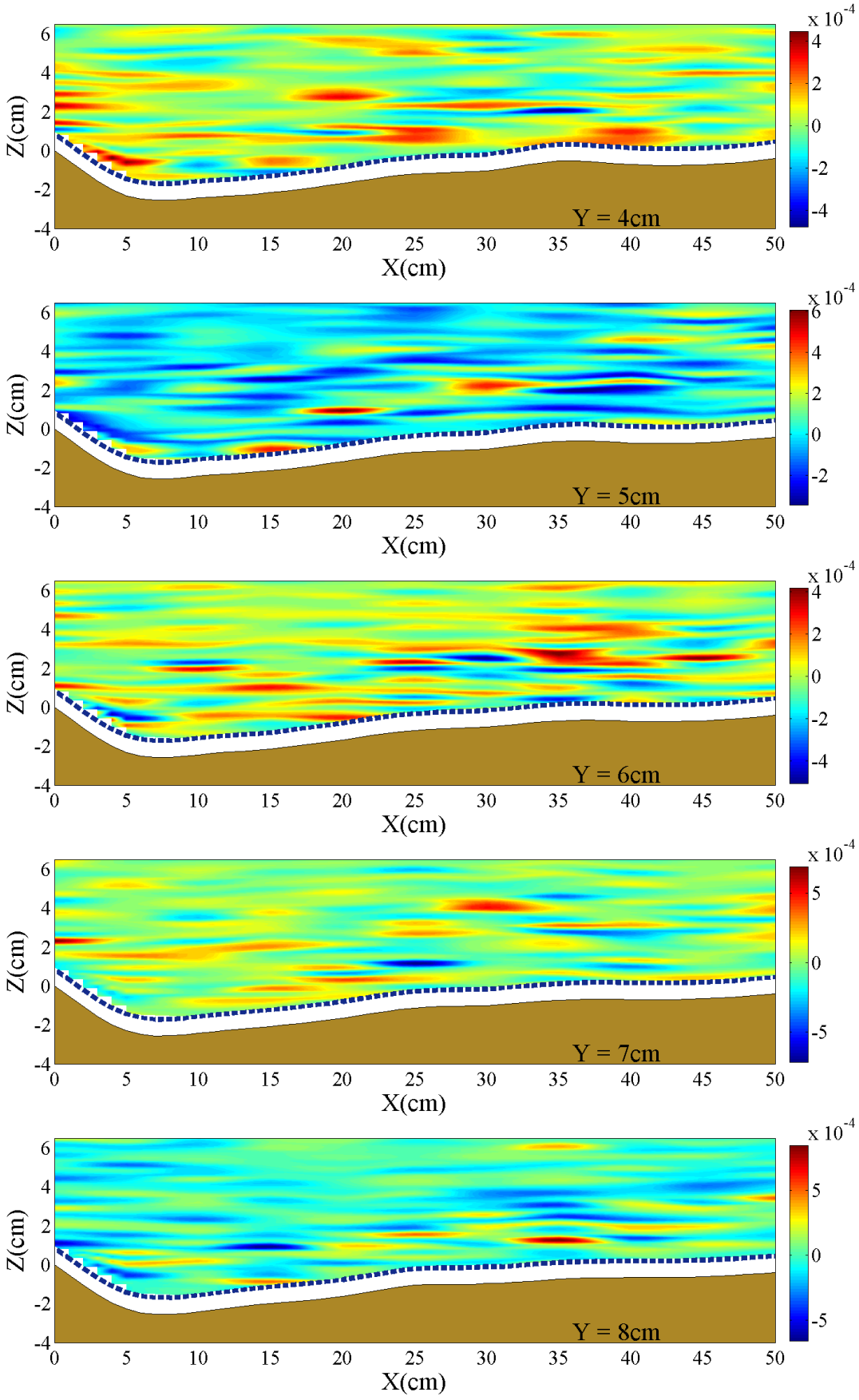

Figure 6.18 – Longitudinal contour maps of $\overline{u'_y u'_z}$ (m^2/s^2): a) 4cm < Y < 8cm.

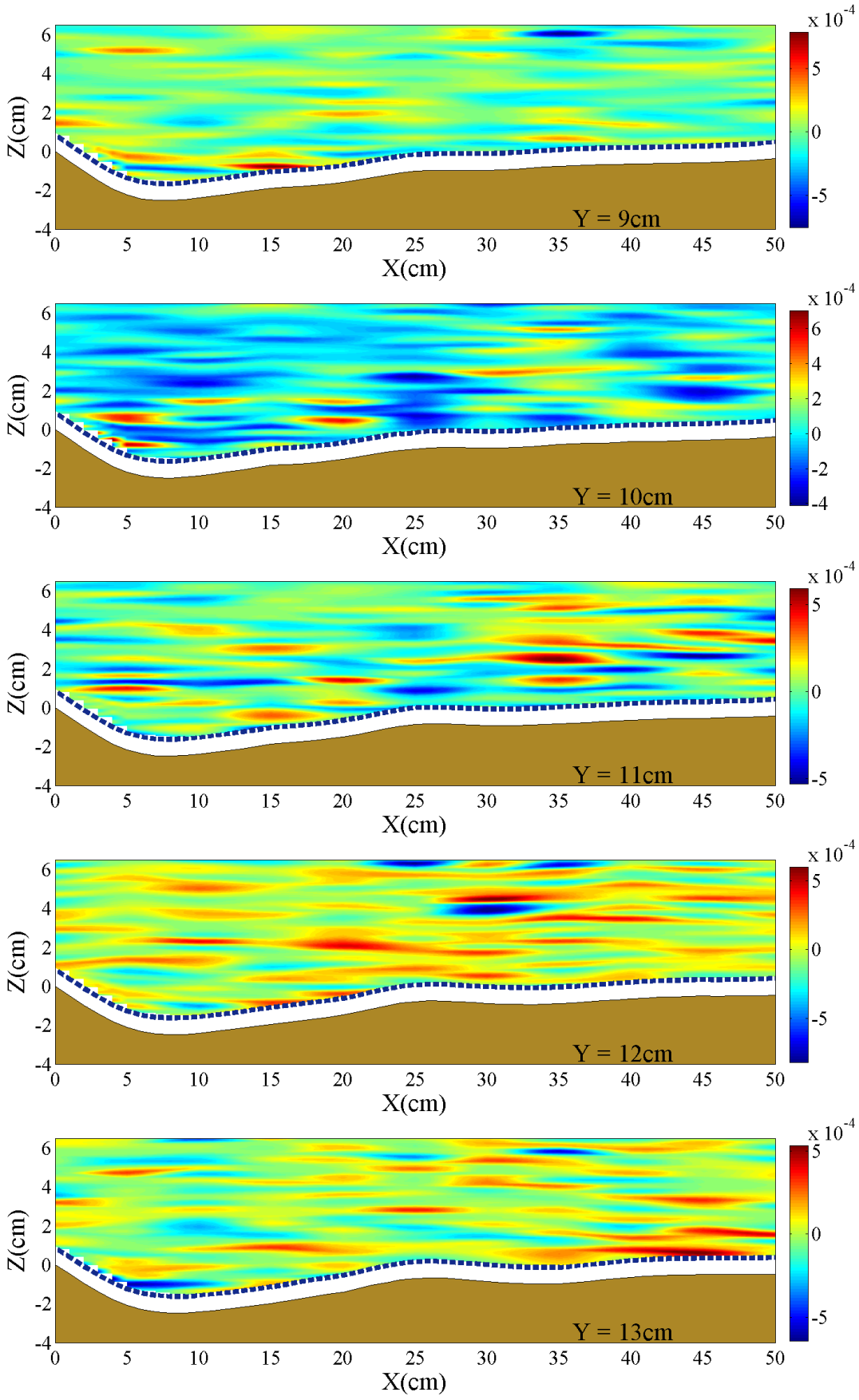

Figure 6.18 – Longitudinal contour maps of $\overline{u'_y u'_z}$ (m^2/s^2): b) 9cm < Y < 13cm.

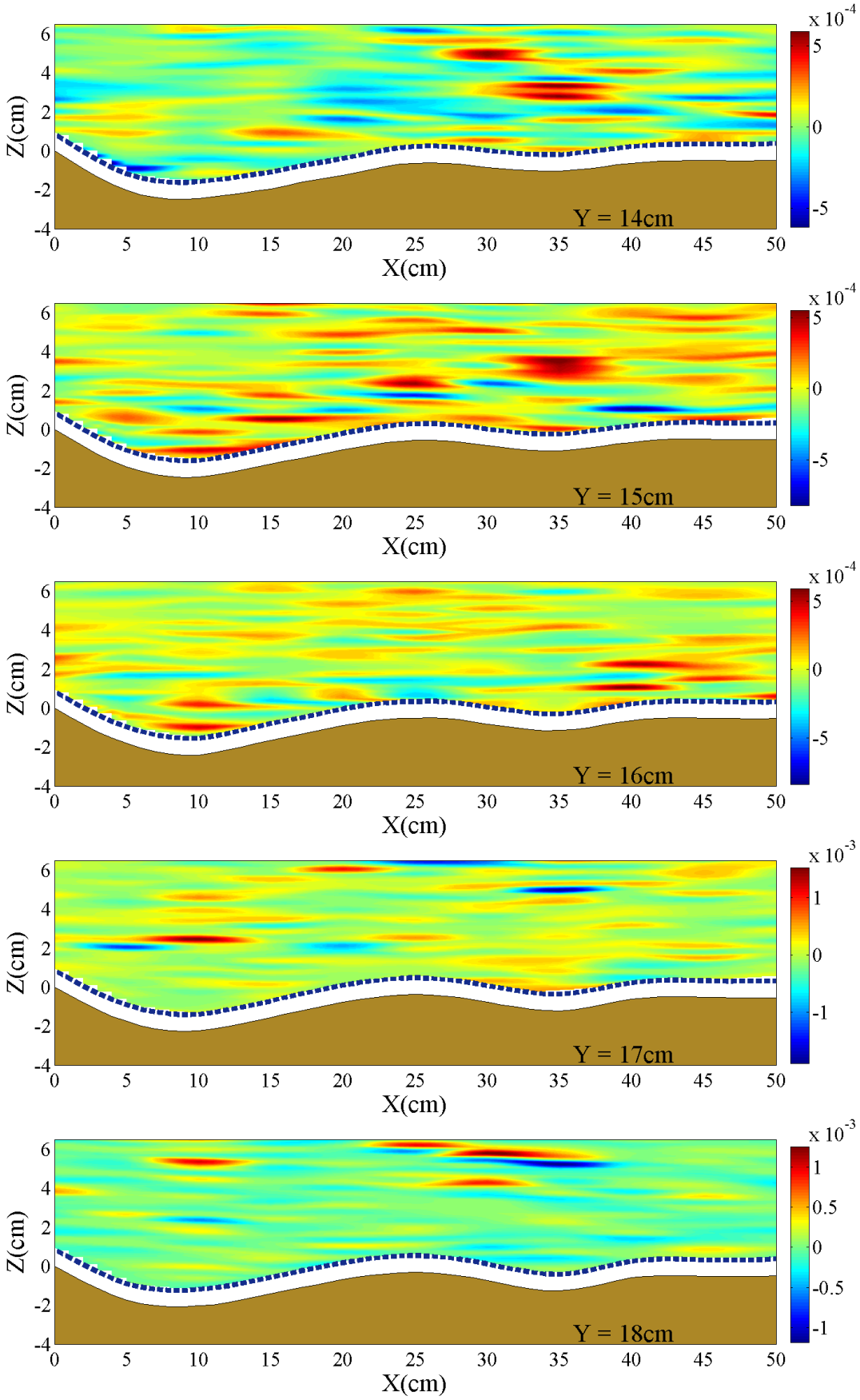

Figure 6.18 – Longitudinal contour maps of $\overline{u'_y u'_z}$ (m^2/s^2): c) 14cm < Y < 18cm.

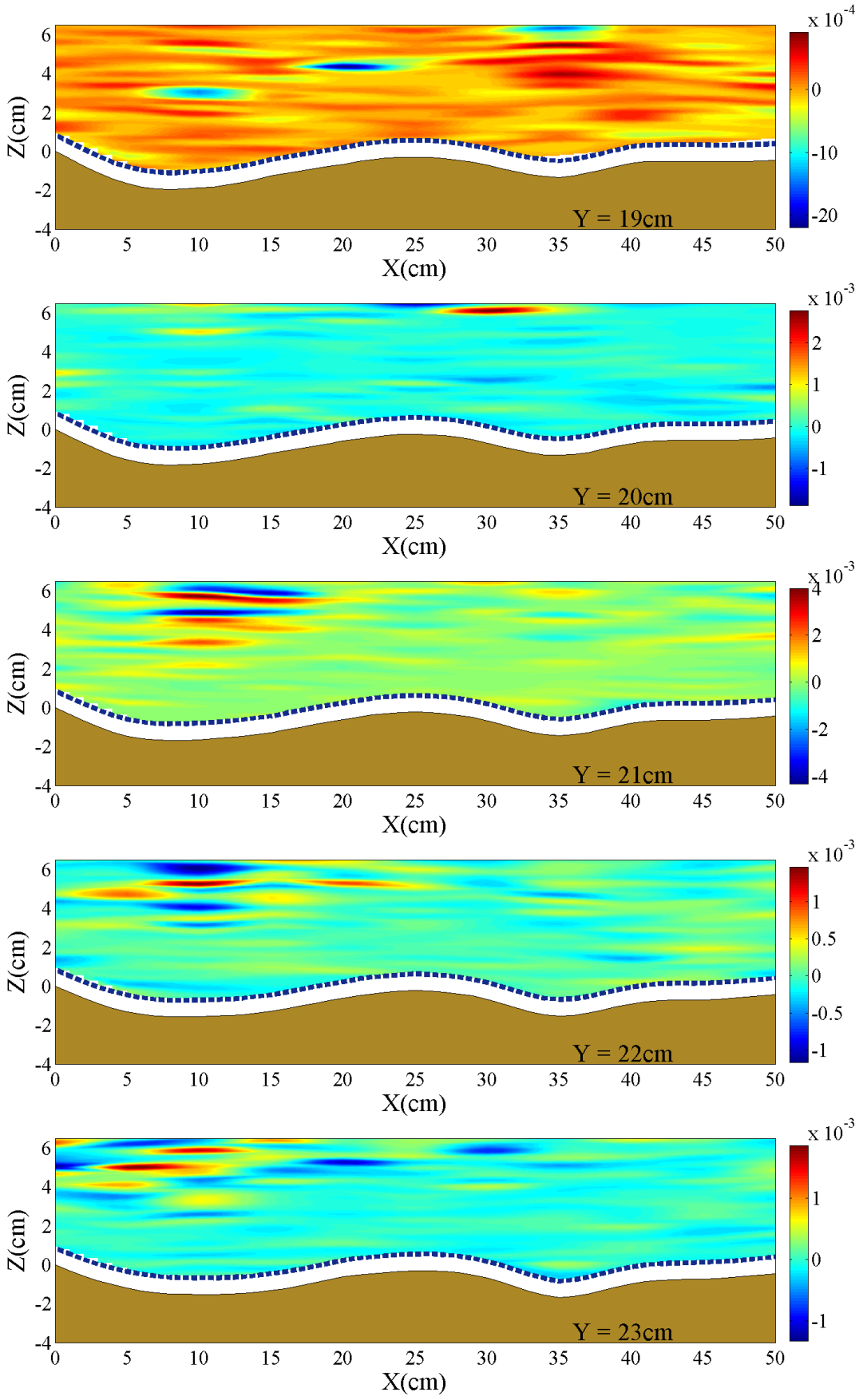

Figure 6.18 – Longitudinal contour maps of $\overline{u'_y u'_z}$ (m^2/s^2): d) 19cm < Y < 23cm.

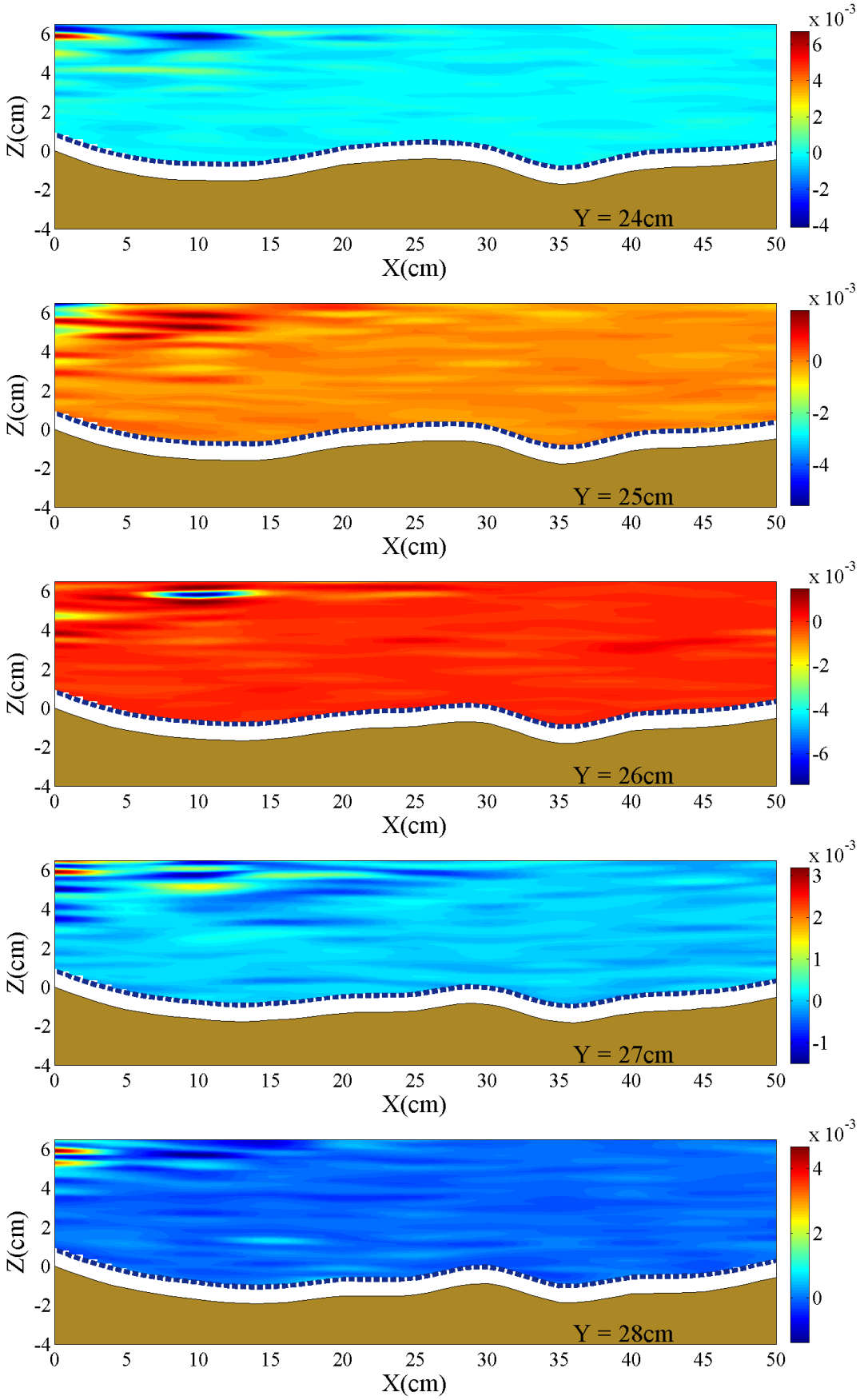

Figure 6.18 – Longitudinal contour maps of $\overline{u'_y u'_z}$ (m^2/s^2): e) 24cm < Y < 28cm.

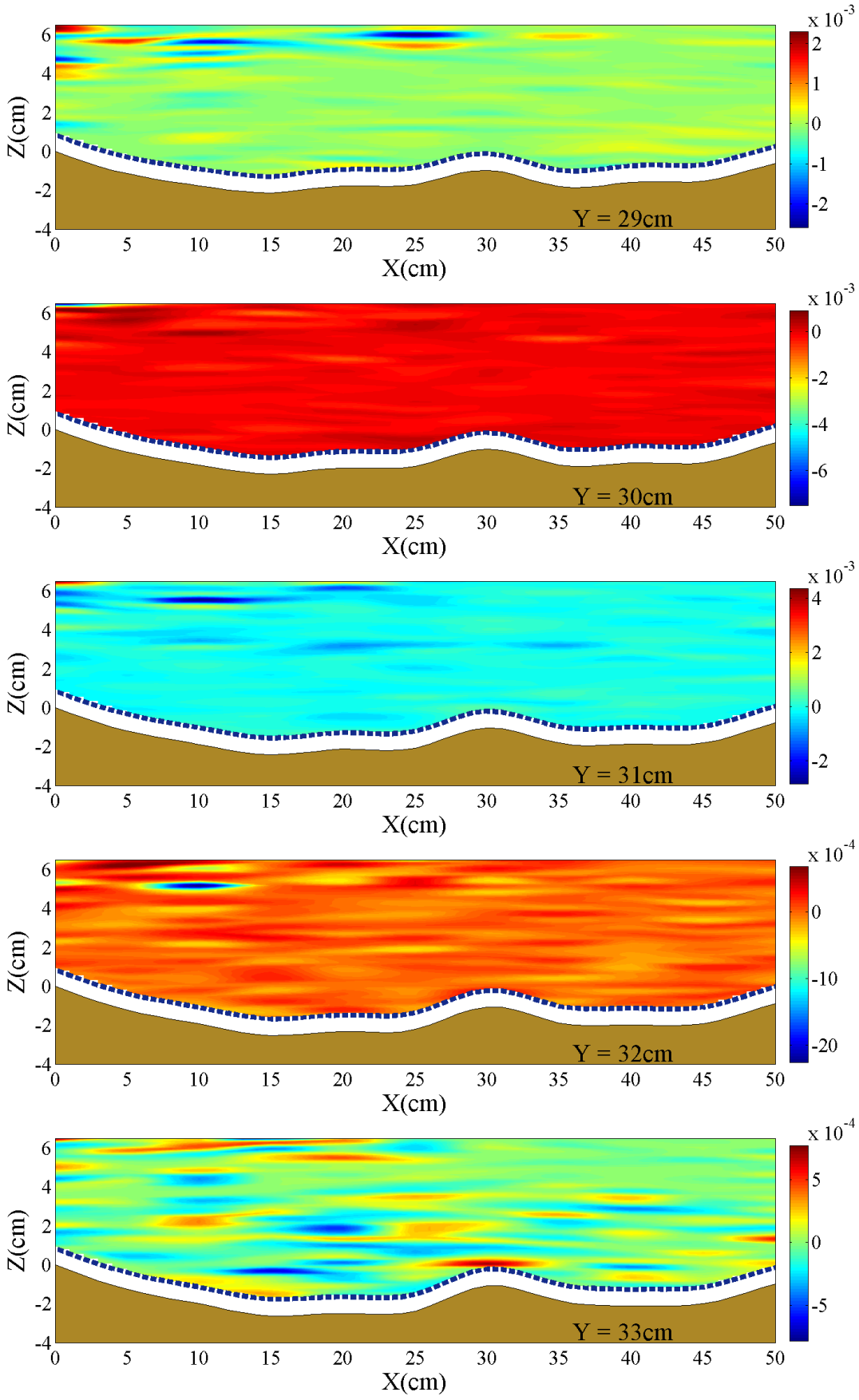

Figure 6.18 – Longitudinal contour maps of $\overline{u'_y u'_z}$ (m^2/s^2): f) 29cm < Y < 33cm.

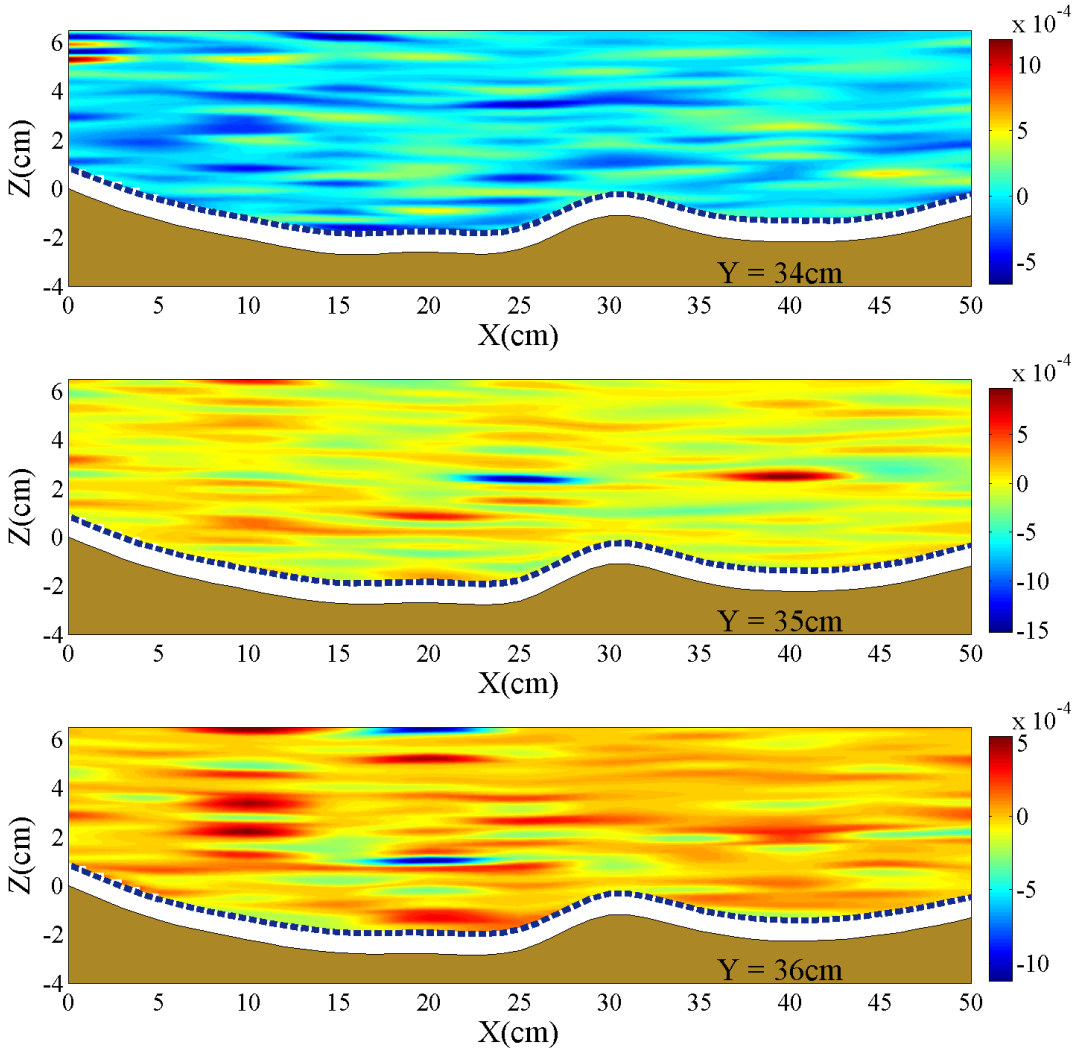

Figure 6.18 – Longitudinal contour maps of $\overline{u'_y u'_z}$ (m^2/s^2): g) 34cm < Y < 36cm.

6.3. Mean flow Kinetic Energy and Turbulent Kinetic Energy

The instantaneous kinetic energy of flow, per unit mass, $E(t)$, can be expressed as:

$$E(t) = \frac{1}{2}\left[\left(u_x(t)\right)^2 + \left(u_y(t)\right)^2 + \left(u_z(t)\right)^2\right] \tag{6.3}$$

By considering the decomposition of equation 6.1, the time average of the kinetic energy of the fluid (per unit mass), E, is given by:

$$E = K + K' = \left[\frac{1}{2}\left(\overline{u_x^2(t)} + \overline{u_y^2(t)} + \overline{u_z^2(t)}\right) + \frac{1}{2}\left(\overline{u_x'^2(t)} + \overline{u_y'^2(t)} + \overline{u_z'^2(t)}\right)\right] \tag{6.4}$$

where K represents the kinetic energy of the mean flow per unit mass and K' is the turbulent kinetic energy. The values of K and K' have been calculated in each measurement point.

6.3.1. Kinetic energy of the mean flow

The contour maps of the kinetic energy K in each considered sections inside the scour hole are reported in Figure 6.19. It can be observed that at section X0, K assumes low values close to the bed and high values near the free surface. From section X5 to section X30 (Figure 6.19a) low values of K occur close to the bed in the near bank regions. At section X30, see Figure 6.19b, an increasing trend of kinetic energy occurs close to the bed. At section X35, K increases at the channel axis, near the bed and it reduces in value close to the left bank, where the scour develops. From section X35 to section X45 (see Figures 6.19b-c) high values of K occur at the channel axis especially near the bed (K = 2.7 m^2/s^2) and an increasing trend of K is also found at the free surface near the left bank (K = 1.5 m^2/s^2). At section X50 the energy pattern is similar to that observed at section X0, but here high kinetic energy values occur at the channel axis near the bed.

The horizontal contour maps of the kinetic energy are reported in Figure 6.20. Near the bed (Z < 1.5cm) the highest value of kinetic energy (K = 3 m^2/s^2) occurs at the channel

axis for X35 < X < X50 (see Figure 6.20a). For Z > 1.5cm the highest values of the mean flow kinetic energy are located near the banks (see Figures 6.20a-b).

The longitudinal distributions of the mean kinetic energy are reported in Figure 6.21. This figure shows that, generally, the kinetic energy assumes high values both near the free surface and to the banks. It can be observed that in the left bank region (4 cm < Y < 18 cm) the kinetic energy of the mean flow has high values near the free surface and for X < X25; low values of K occurs near the bed, particularly inside the scour hole (X5 < X < X15). Moreover low values of K occur downstream of the deposition (X > X30) near the free surface. Approaching to the channel axis (Y = 18cm, see Figure 6.21c) for X > X35, the mean kinetic energy increases near the free surface. At Y = 21cm high values of the mean flow kinetic energy is clearly distinguishable close to the bed for X > X40. At the left bank region, see Figures 6.21d-g, the energy distributions are similar to that observed near the right bank.

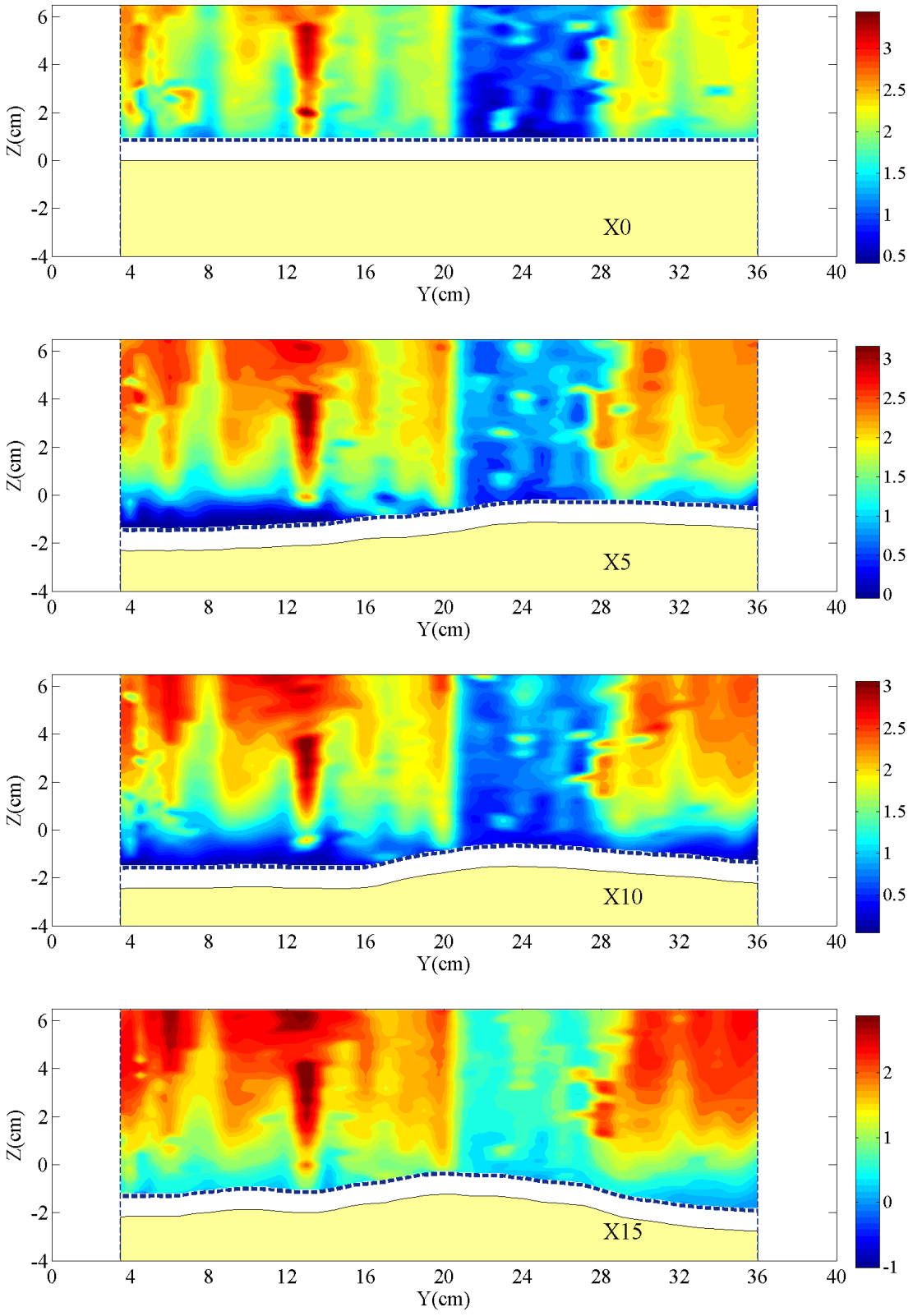

Figure 6.19– Contour maps of K (m^2/s^2): a) X0 < X < X15.

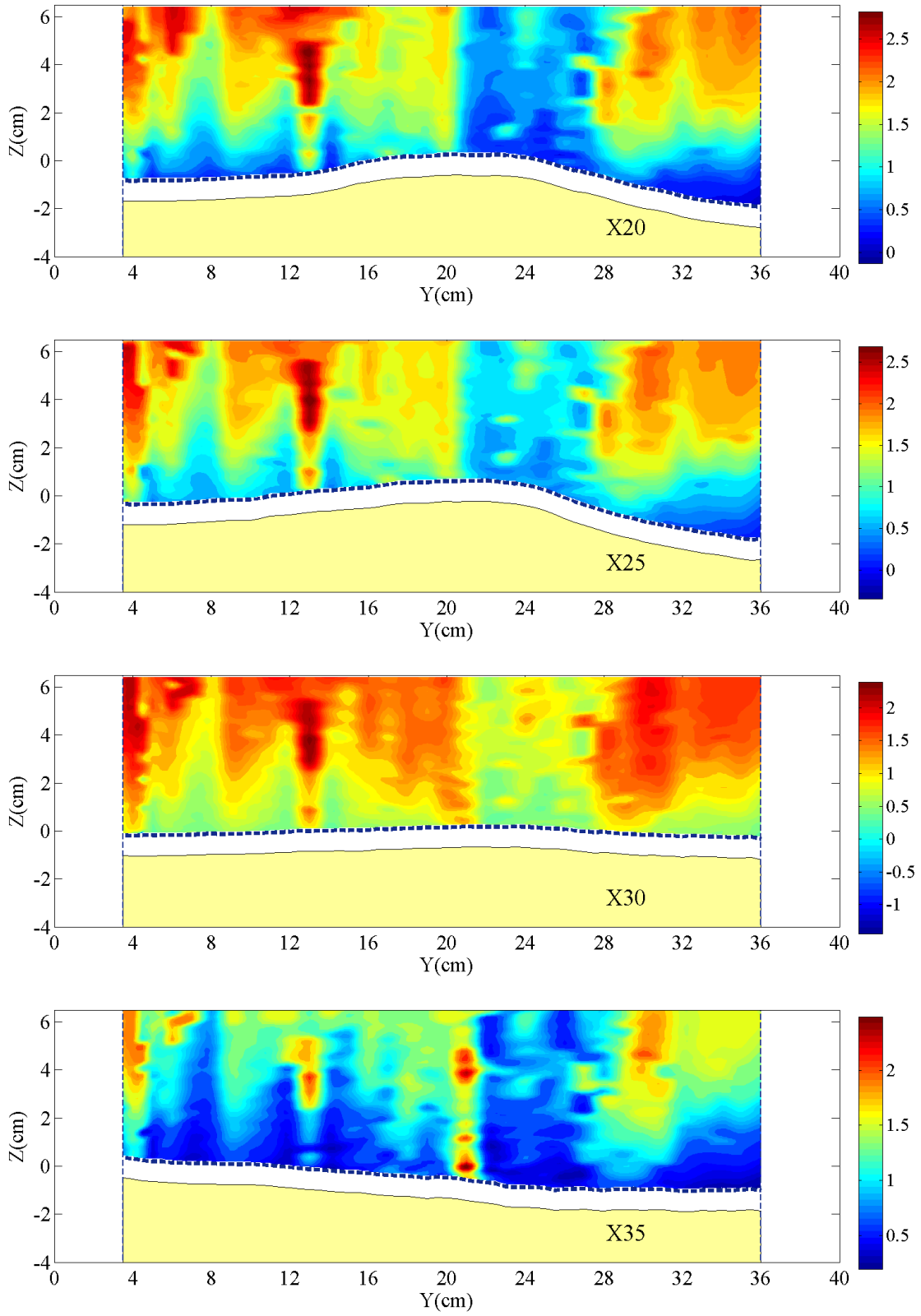

Figure 6.19– Contour maps of K (m^2/s^2): b) X20 < X < X35.

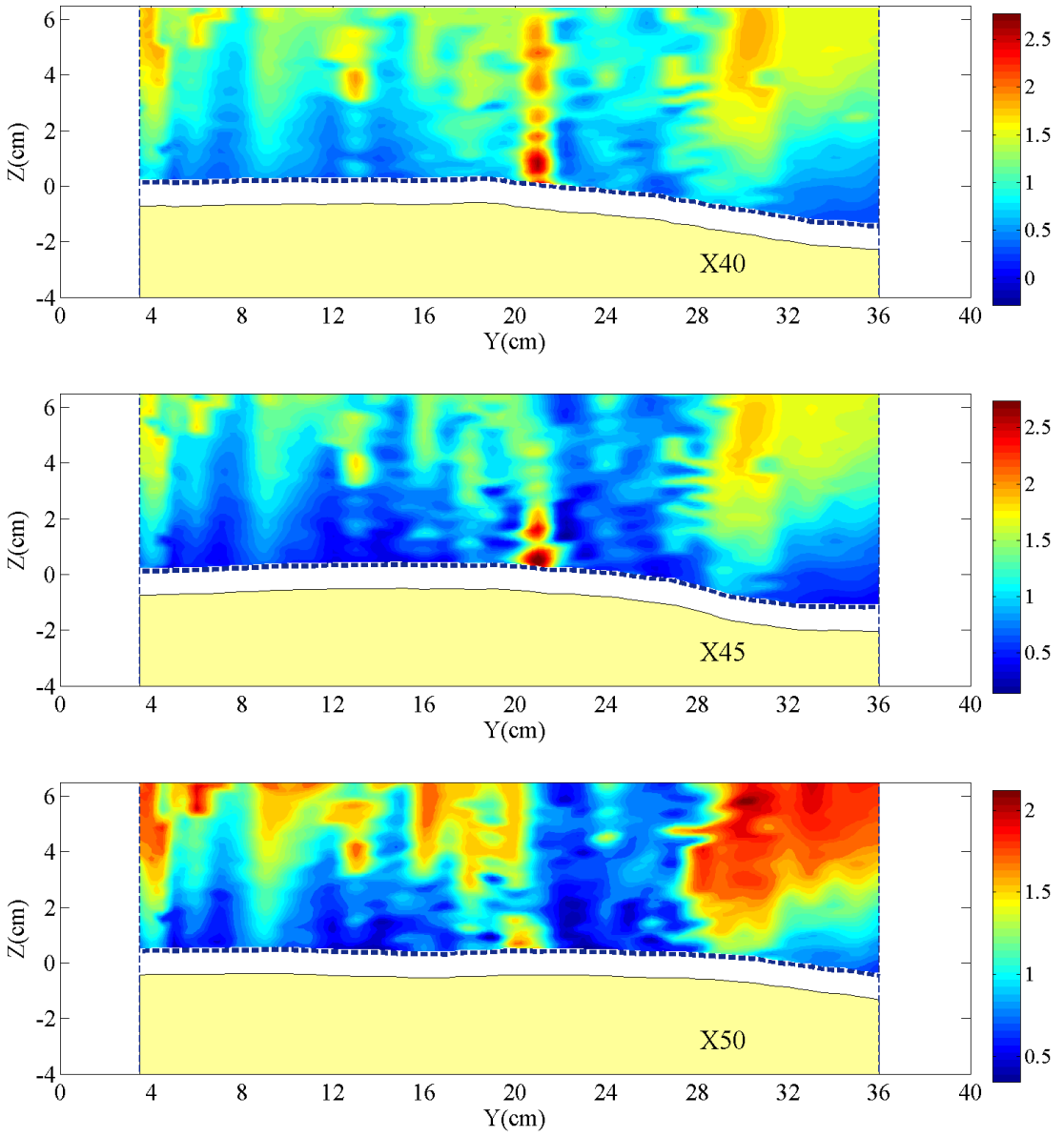

Figure 6.19– Contour maps of K (m^2/s^2): c) X40 < X < X50.

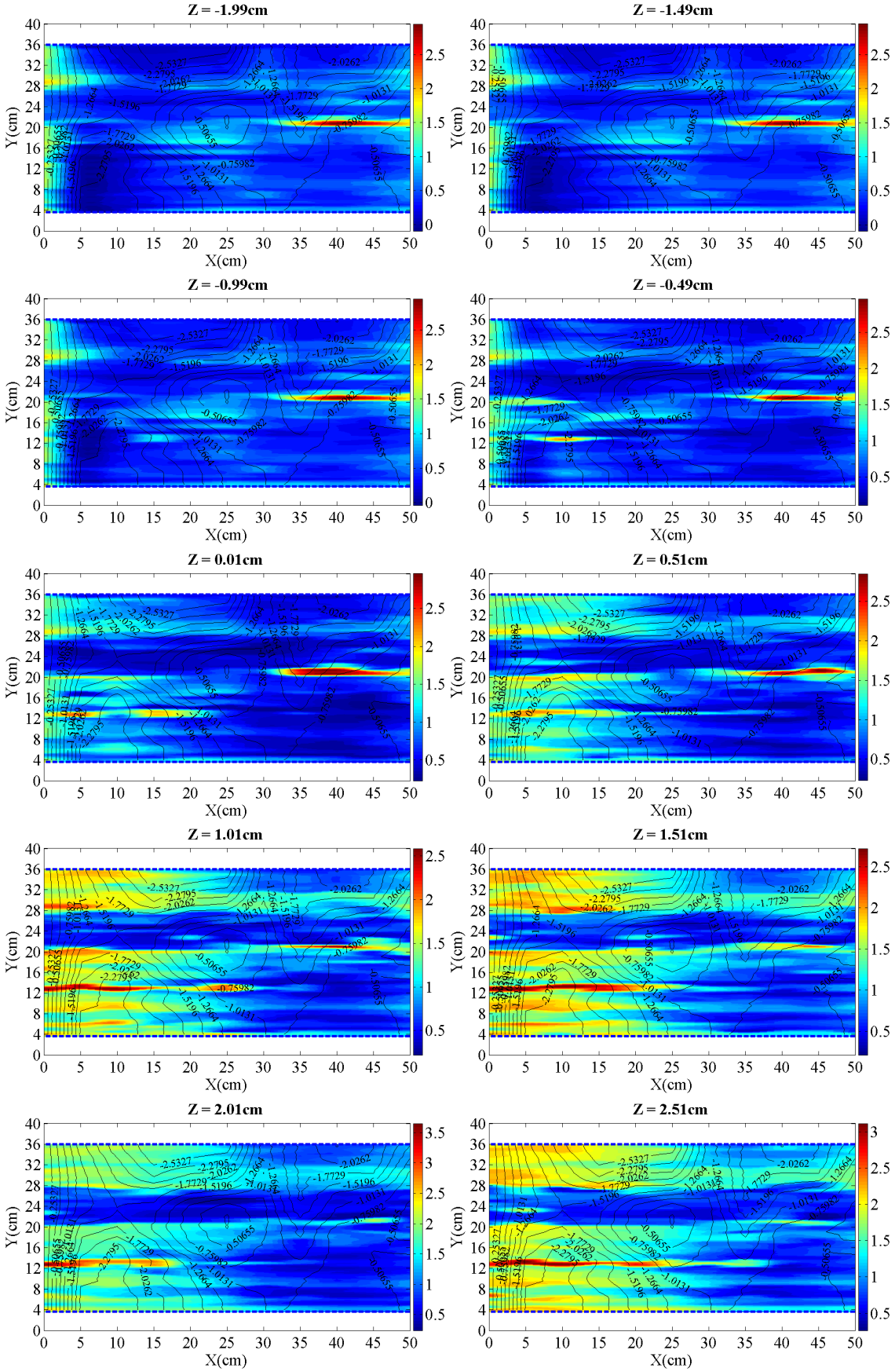

Figure 6.20 – Horizontal contour maps of K (m^2/s^2): a) -1.99cm < Z < 2.51cm.

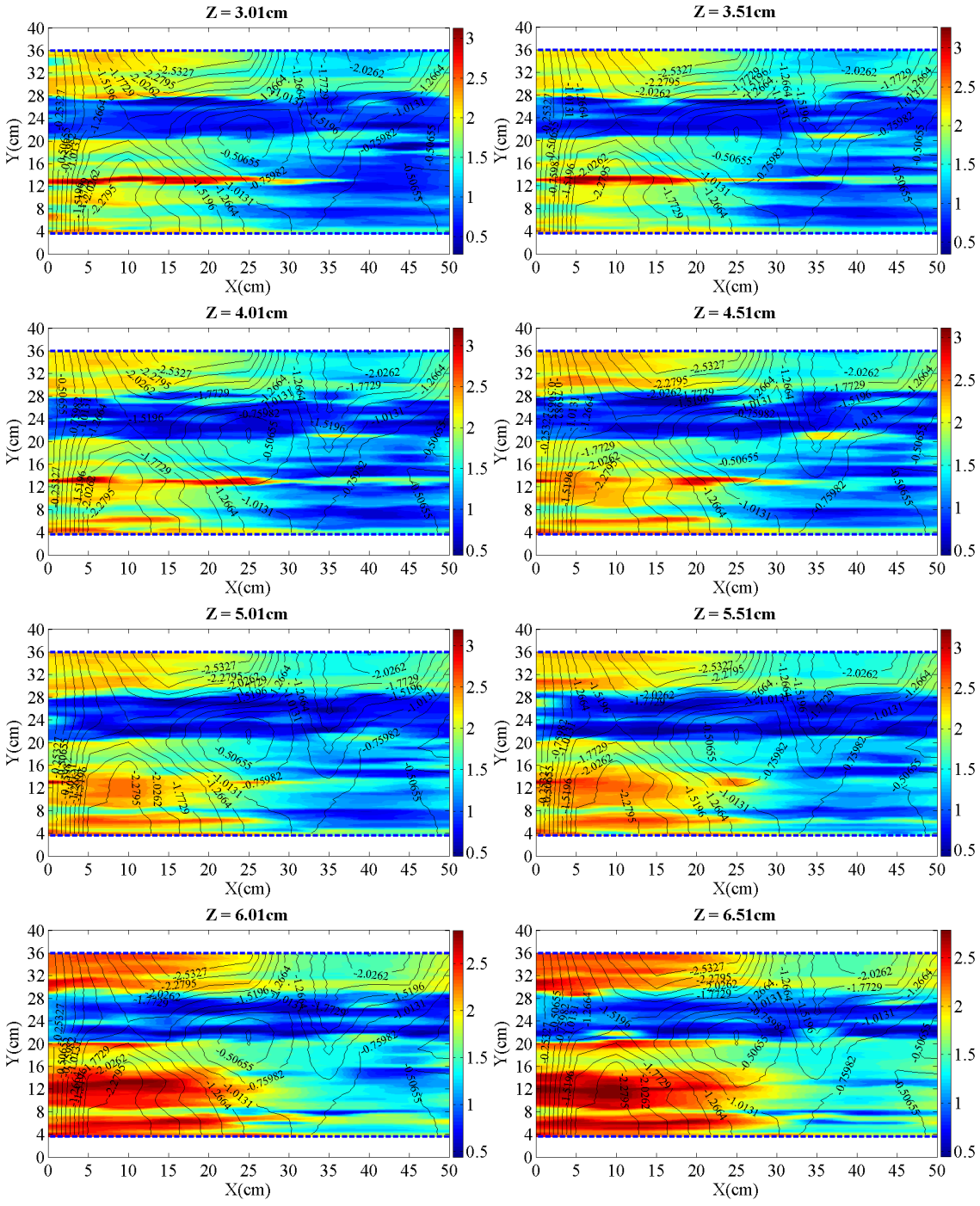

Figure 6.20 – Horizontal contour maps of K (m^2/s^2): b) 3.01cm < Z < 6.51cm.

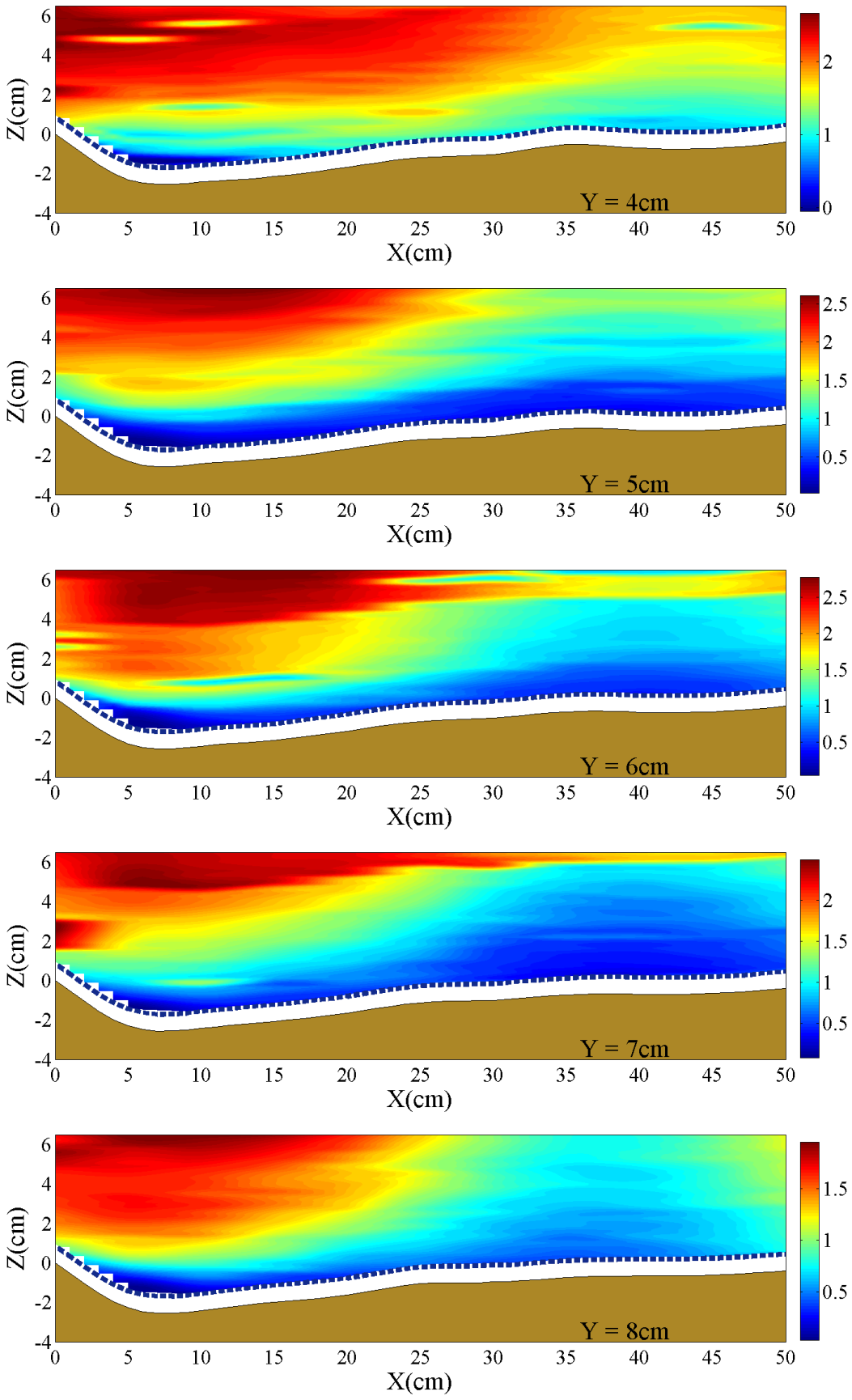

Figure 6.21 – Longitudinal contour maps of K (m^2/s^2): a) 4cm < Y < 8cm.

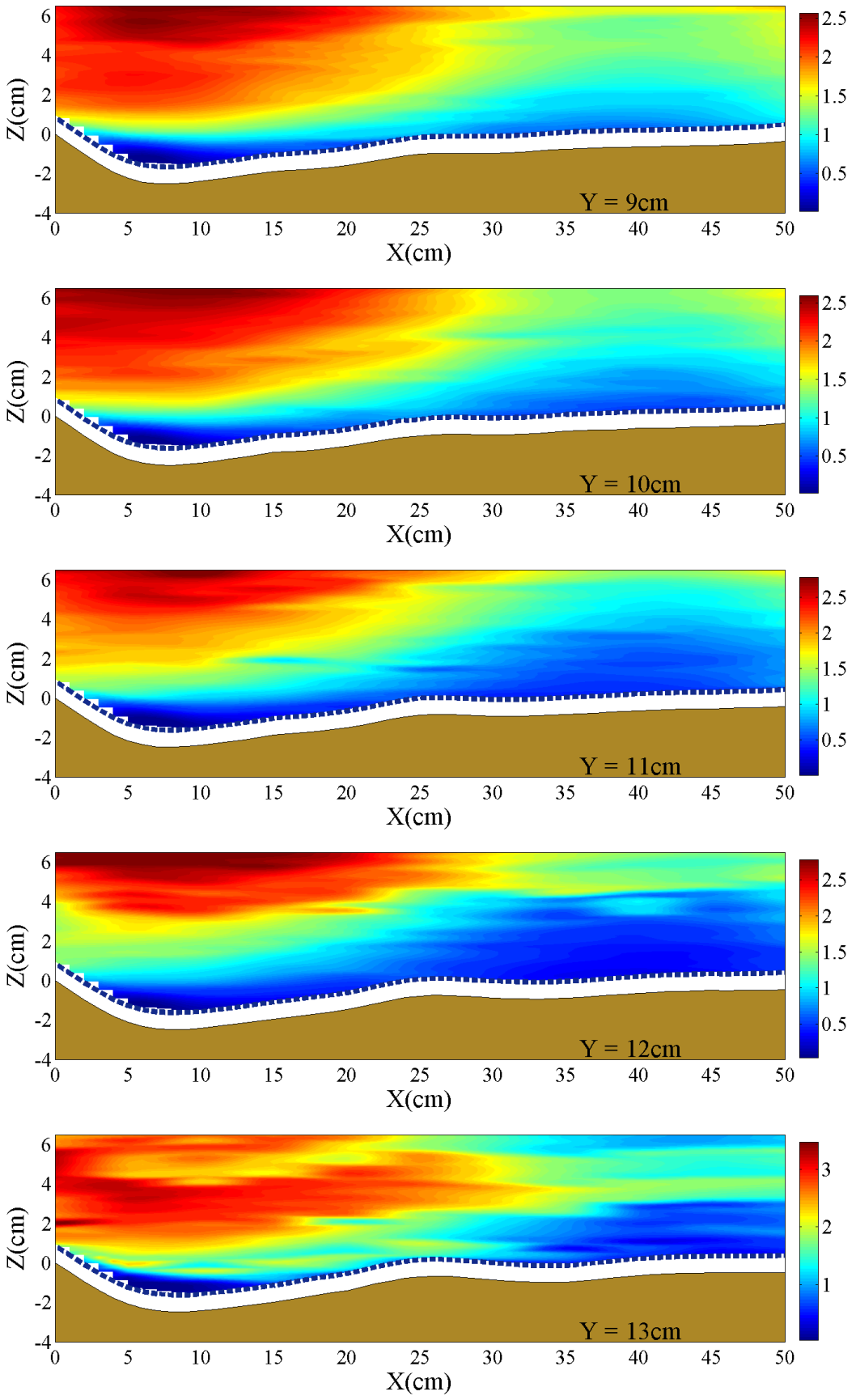

Figure 6.21 – Longitudinal contour maps of K (m^2/s^2): b) 9cm < Y < 13cm.

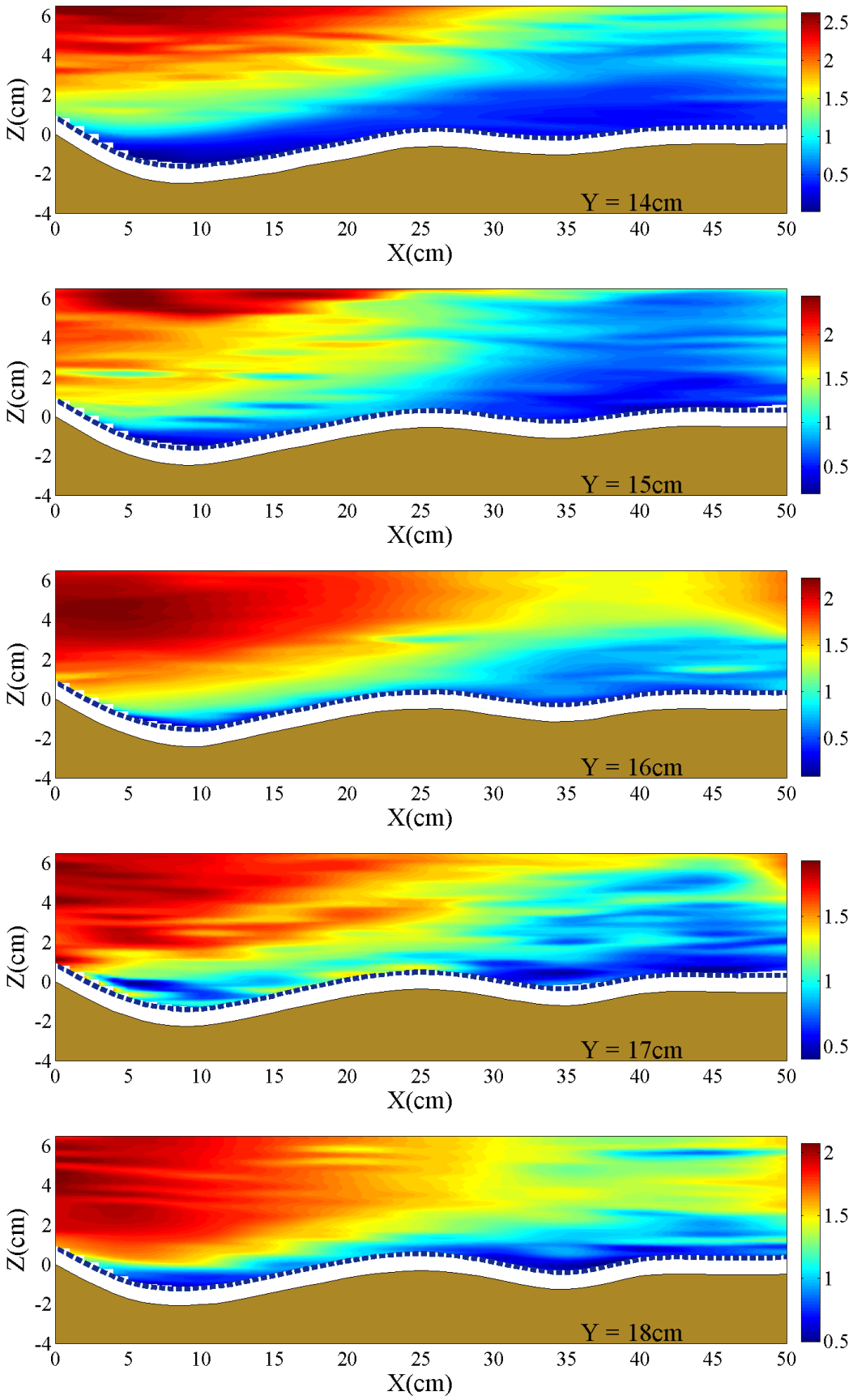

Figure 6.21 – Longitudinal contour maps of K (m^2/s^2): c) 14cm < Y < 18cm.

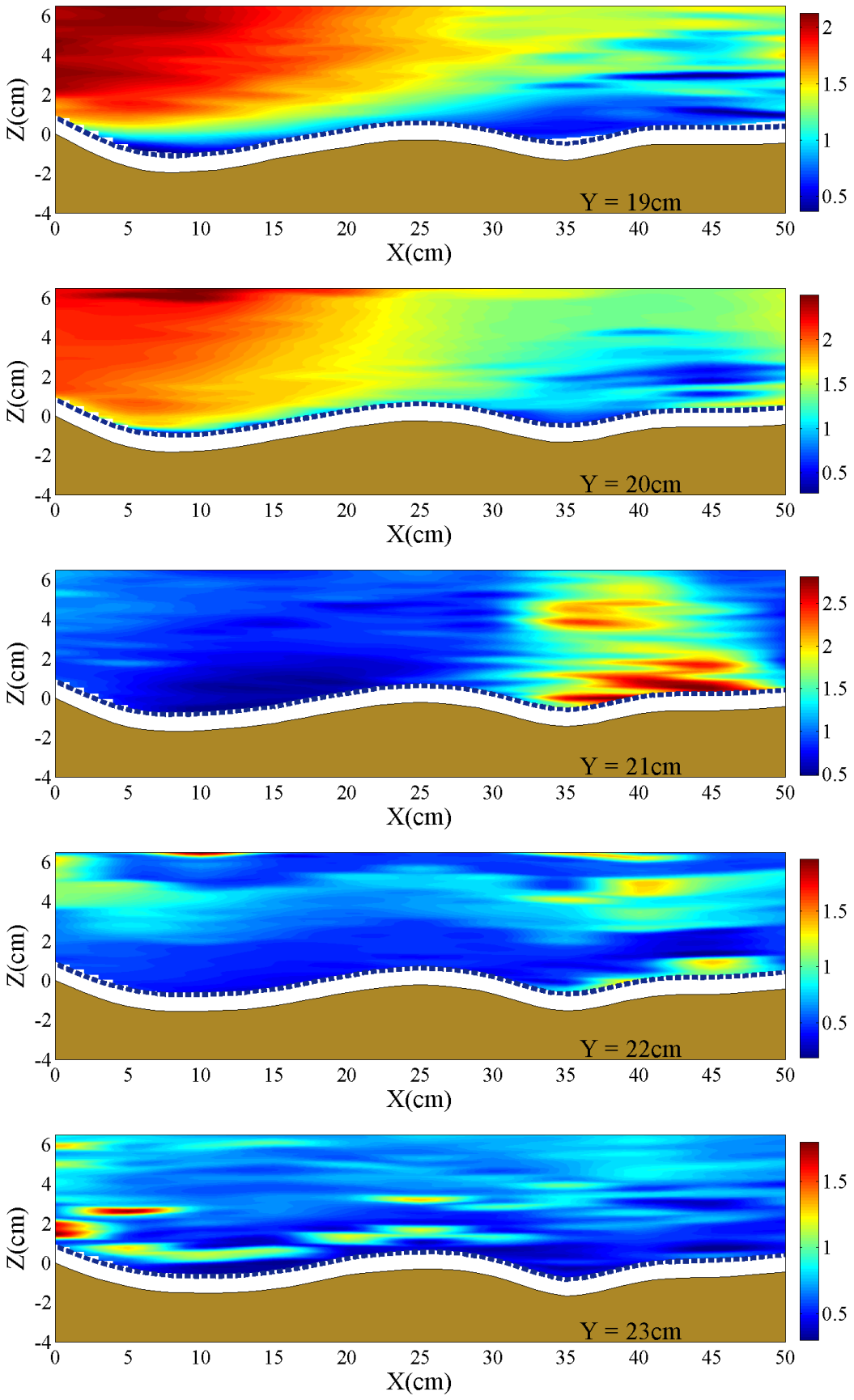

Figure 6.21 – Longitudinal contour maps of K (m^2/s^2): d) 19cm < Y < 23cm.

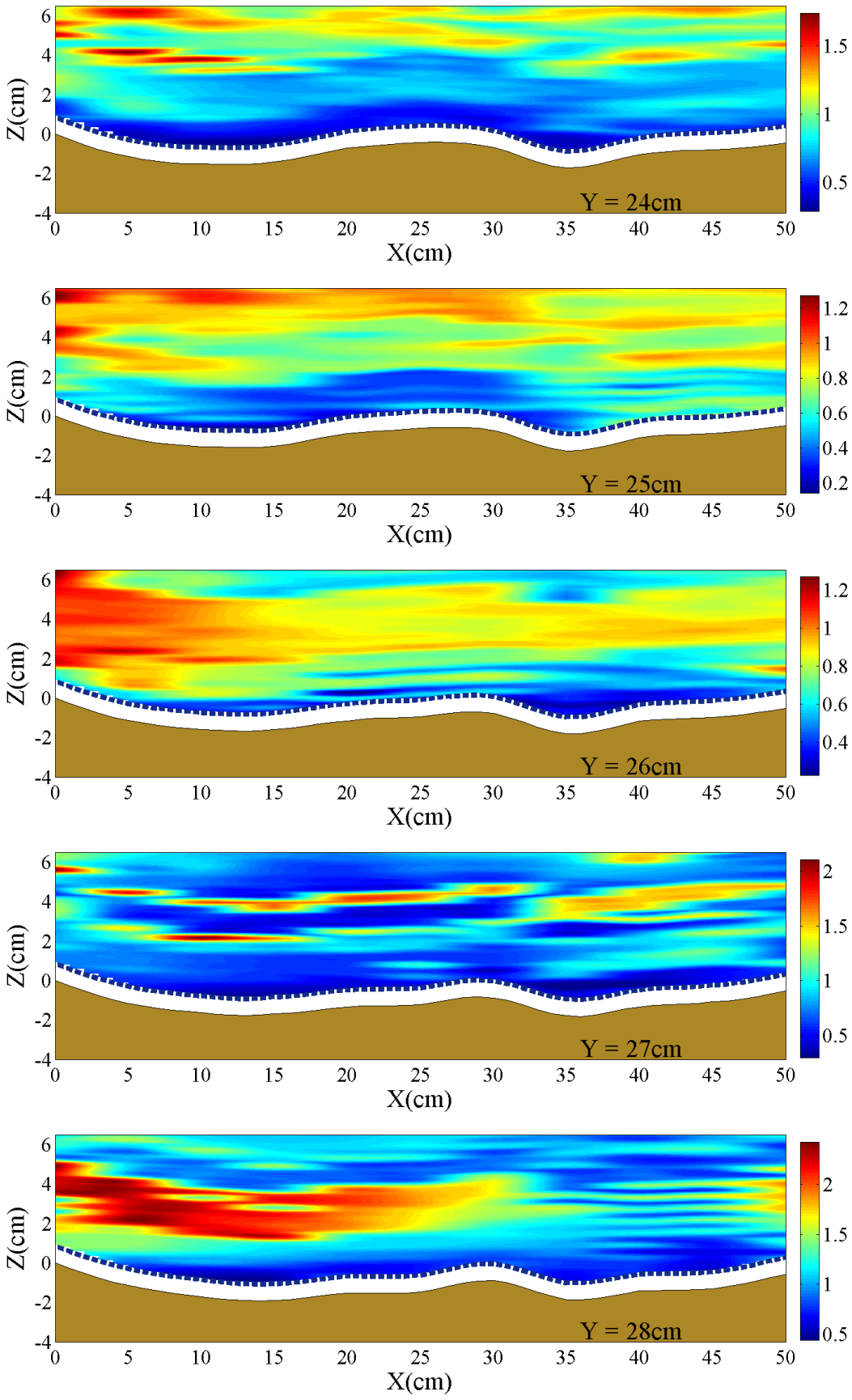

Figure 6.21 – Longitudinal contour maps of K (m^2/s^2): e) 24cm < Y < 28cm.

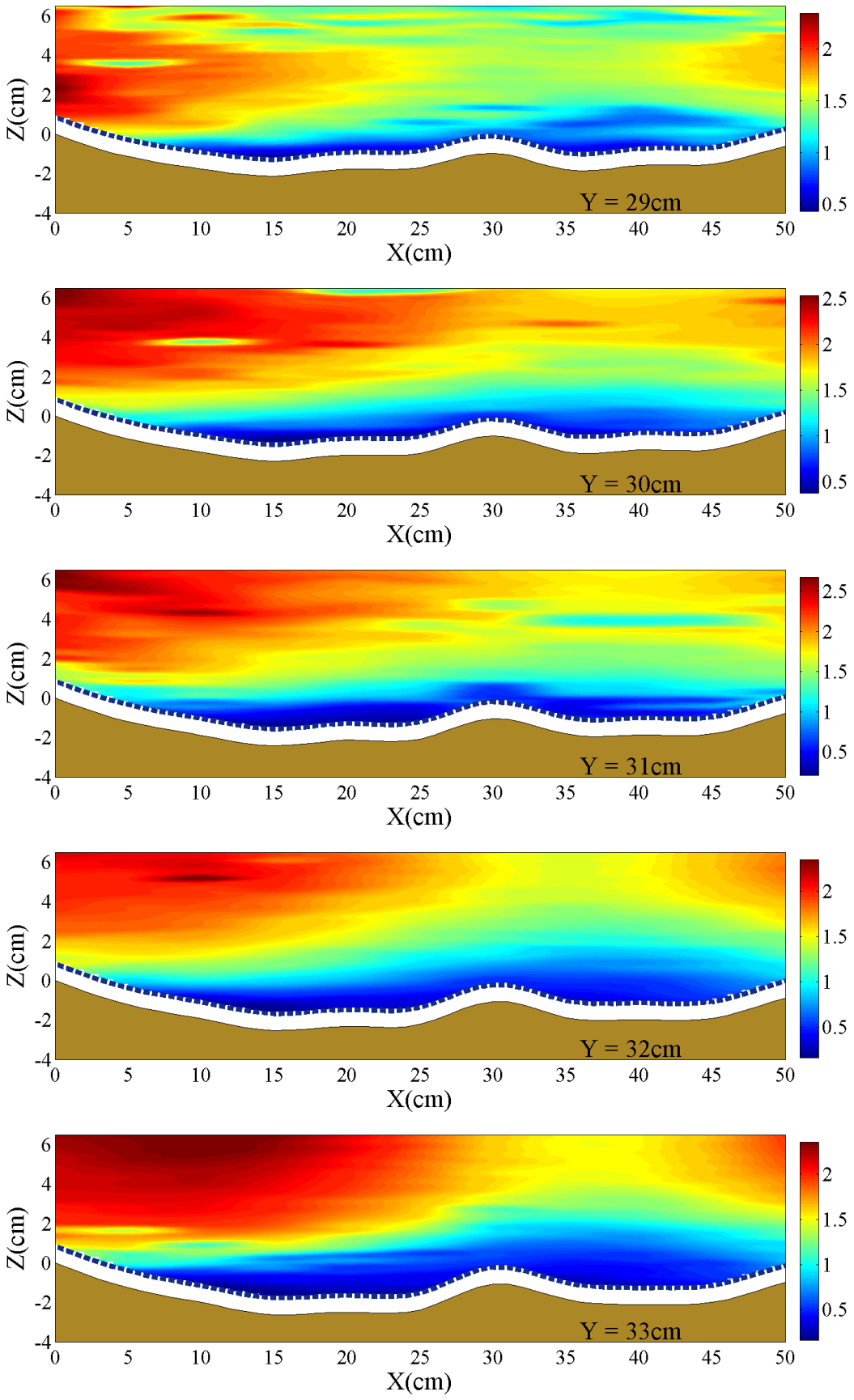

Figure 6.21 – Longitudinal contour maps of K (m^2/s^2): f) 29cm < Y < 33cm.

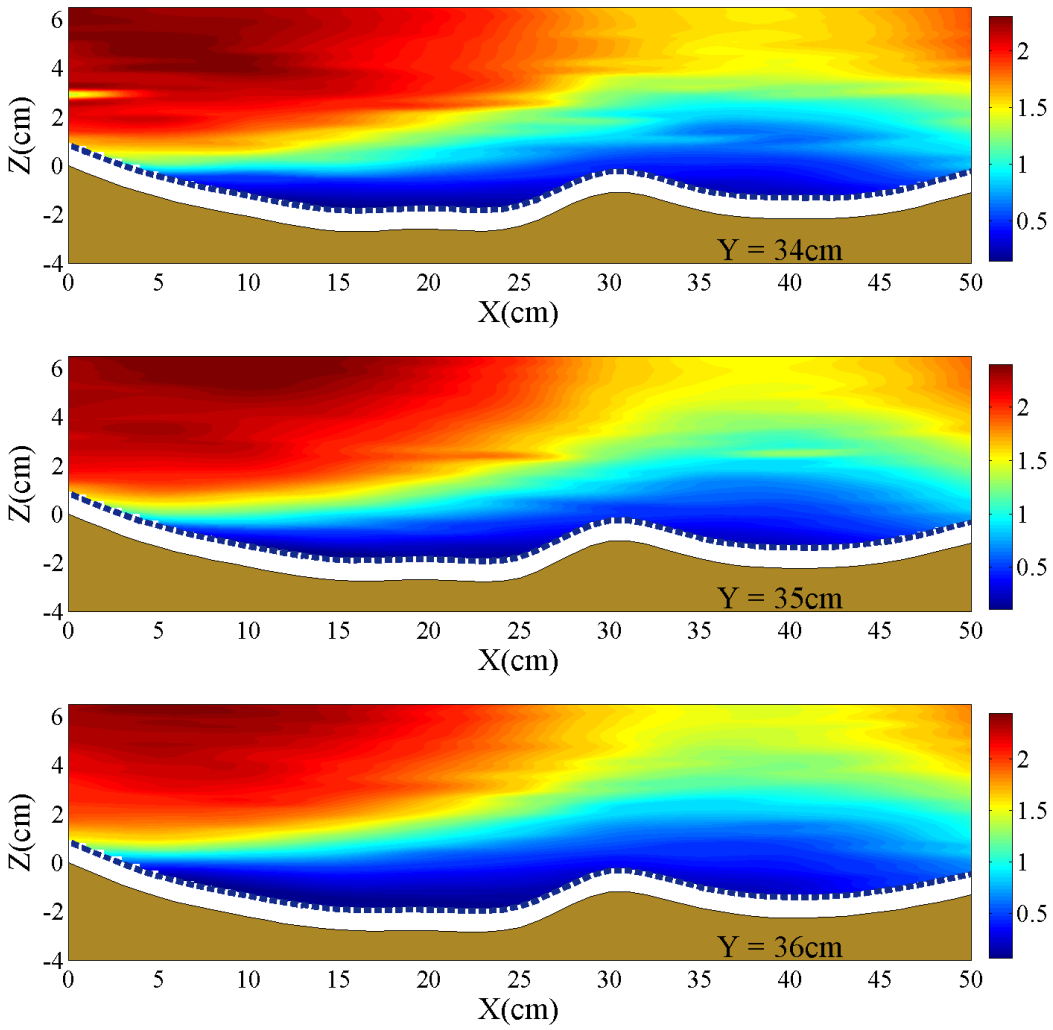

Figure 6.21 – Longitudinal contour maps of K (m^2/s^2): g) 34cm < Y < 36cm.

6.3.2. Turbulent kinetic Energy

The transverse contour maps of the turbulent kinetic energy *K'* for the analyzed sections are reported in Figure 6.22. It can be observed that *K'* assumes high values near the bed, especially in the near bank regions. In particular, at section X5 the turbulent kinetic energy increases near the bed inside the right bank region (for Y < 18cm). At section X10 the turbulent kinetic energy increases in value in both the near bank region (up to = 0.12 m^2/s^2) and near the bed. At section X15 (see Figure 6.22a) the turbulent kinetic energy starts to reduce in value near the bank regions. In the range X30 < X < X50 (see Figures 6.22b-c) *K'* increases in value, up to 1.5 m^2/s^2, at the channel axis (Y = 20cm) near the bed.

The horizontal contour maps of the turbulent kinetic energy *K'* are reported in Figure 6.23. It can be observed that the highest values of *K'* essentially occur at the channel axis and for X > X35 as it has been observed in Figure 6.22b.The longitudinal contour maps of the turbulent kinetic energy are reported in Figure 6.24. Near the banks (Y < 11cm and Y > 27cm) it can be observed that *K'* assumes high values inside the scour hole (X < X30). For X > X30cm high values of the turbulent kinetic energy occur generally at the channel axis. In particular, in Figure 6.24a it can be observed that for Y < 7 cm *K'* assumes high values in the scour hole (X < X30). Streaks of high value are also visible near the free surface, downstream of the scour hole. This pattern of the turbulent kinetic energy is strictly linked with the longitudinal evolution of the kinetic energy observed in Figure 6.21a. The distributions of the turbulent kinetic energy in Figure 6.24b show that it increases in intensity where the mean flow kinetic energy reduces (Figure 6.23b). For 14cm < Y < 23cm (see Figures 6.24c-d) high values of *K'* occur in the whole flow depth downstream of the zone of sand deposit (X40 < X < X50). Moving towards the left bank (Figures 6.24e-g) high values of K' are found in the left scour hole at Y = 36 cm.

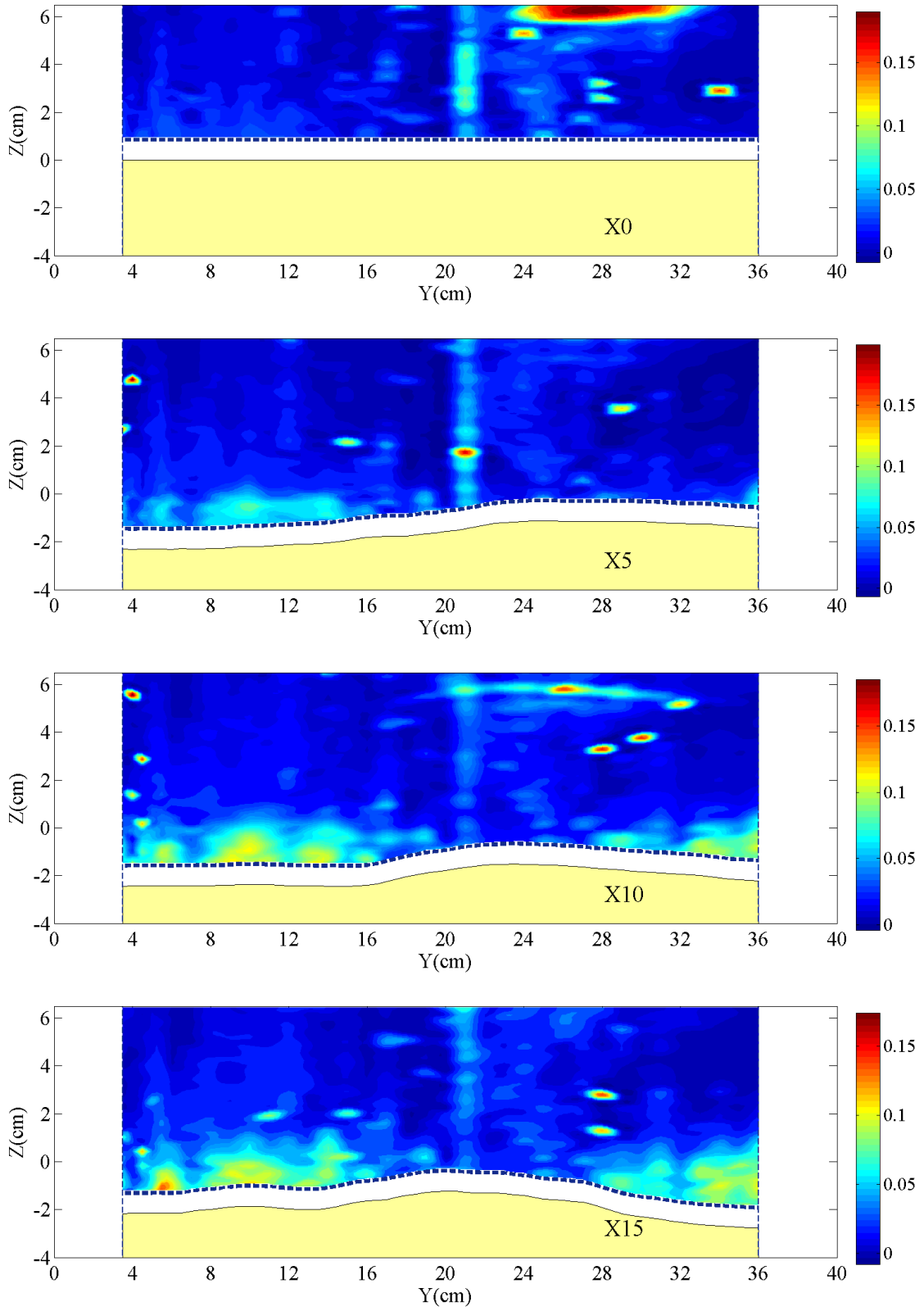

Figure 6.22 – Contour maps of K' (m^2/s^2): a) X0 < X < X15.

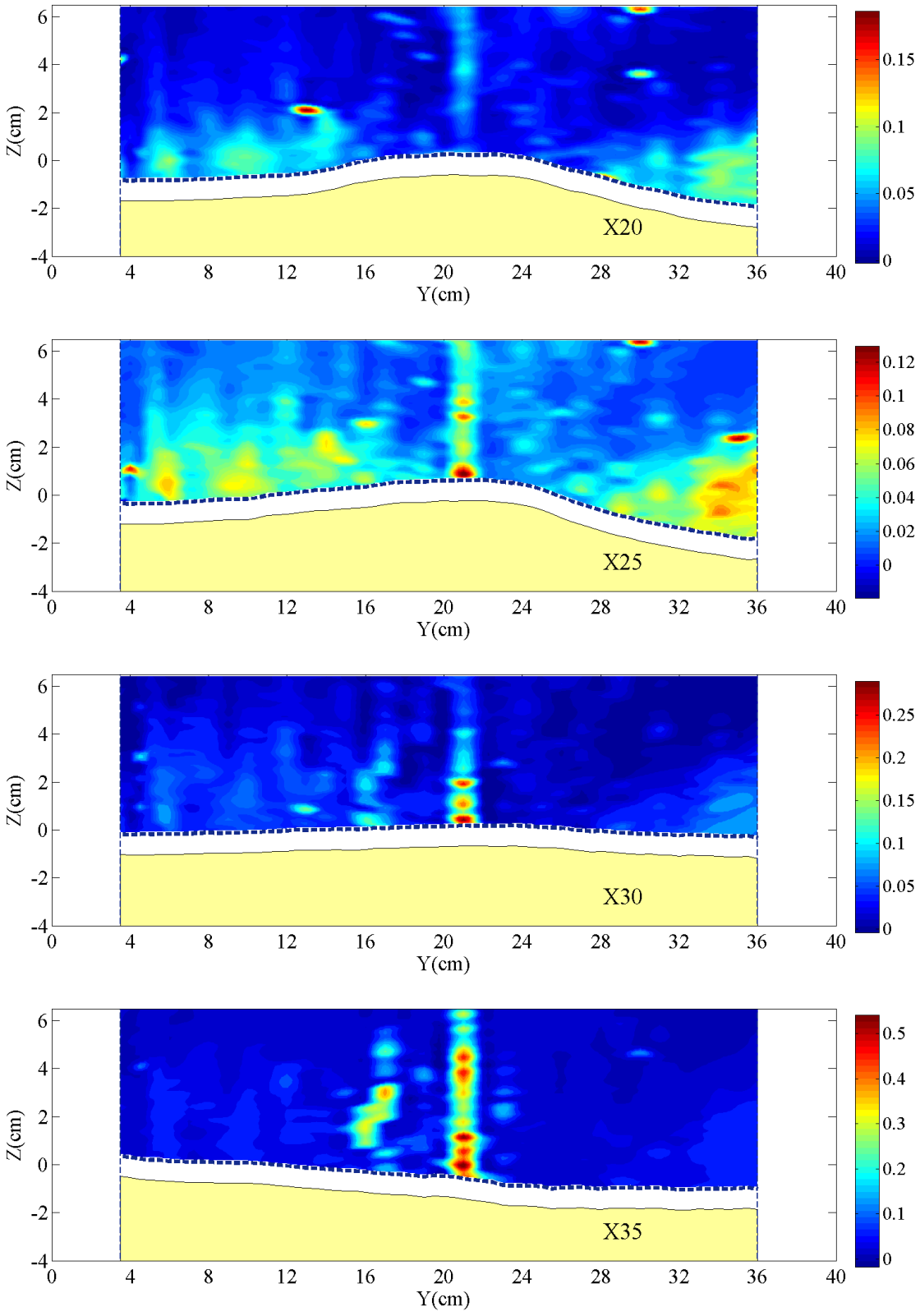

Figure 6.22 – Contour maps of K' (m^2/s^2): b) X20 < X < X35.

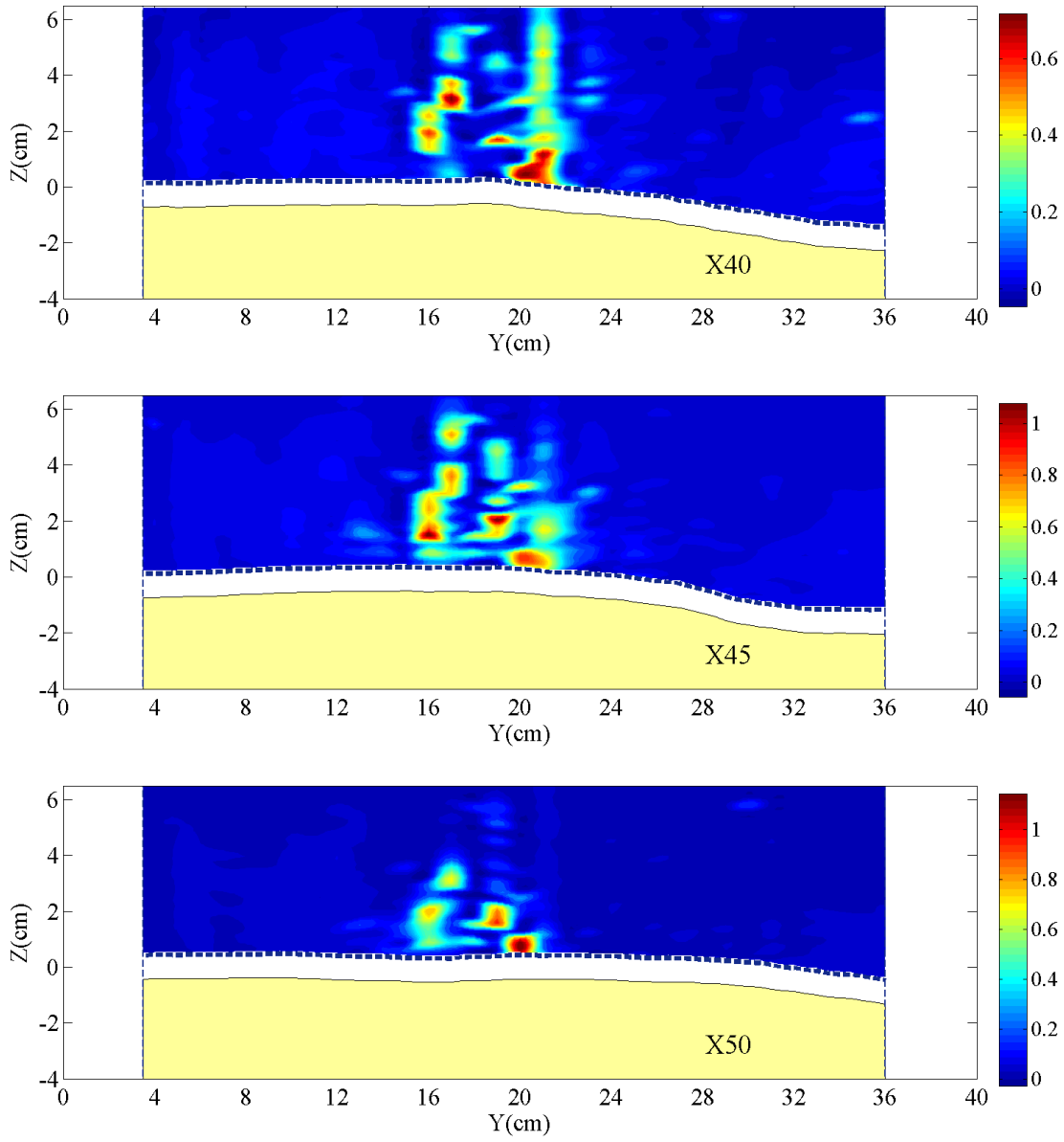

Figure 6.22 – Contour maps of K' (m^2/s^2): c) X40 < X < X50.

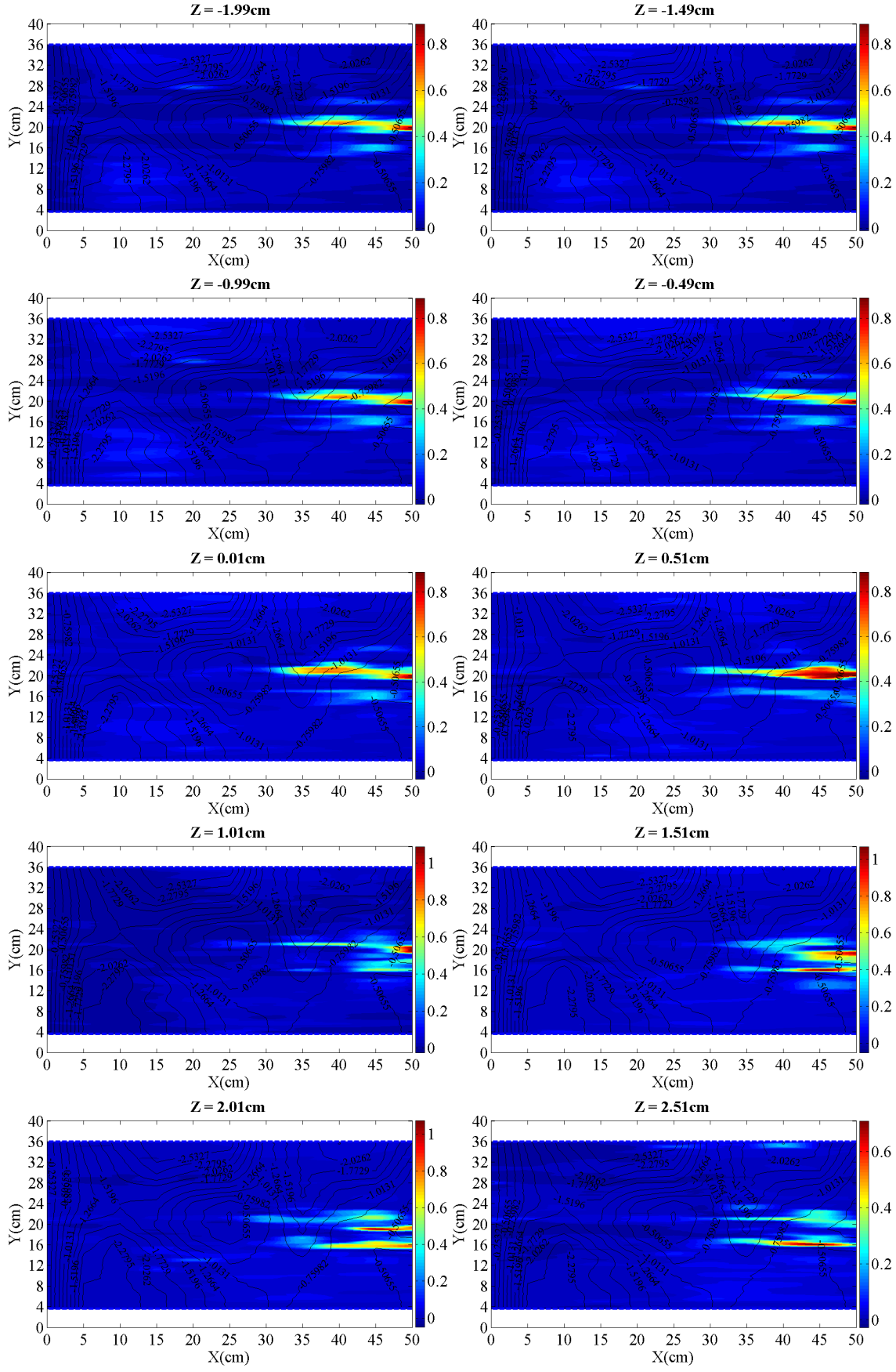

Figure 6.23 – Horizontal contour maps of K' (m^2/s^2): a) -1.99cm < Z < 2.51cm.

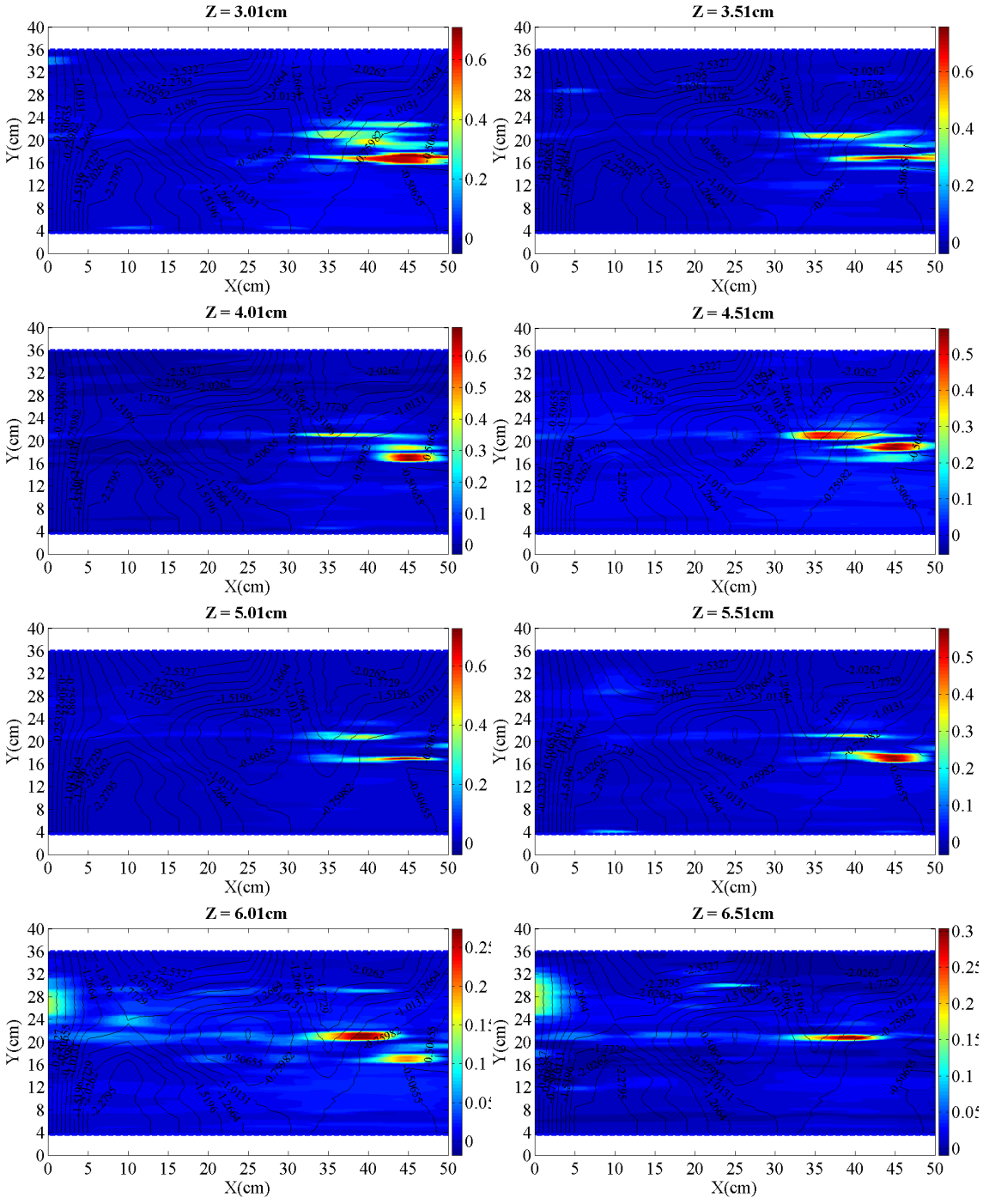

Figure 6.23 – Horizontal contour maps of K' (m^2/s^2): b) 3.01cm < Z < 6.51cm.

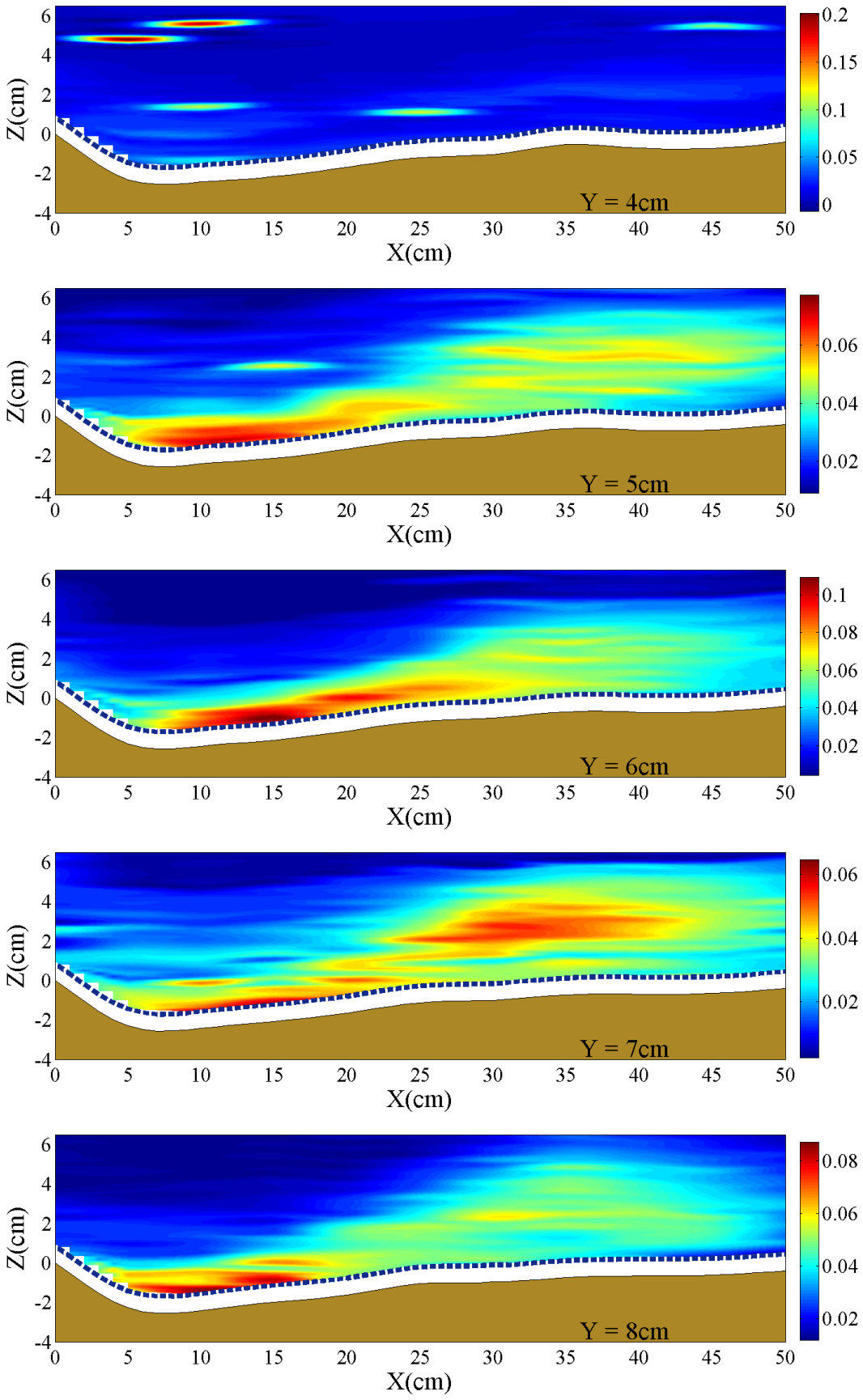

Figure 6.24 – Longitudinal contour maps of *K'* (m^2/s^2): a) 4cm < Y < 8cm.

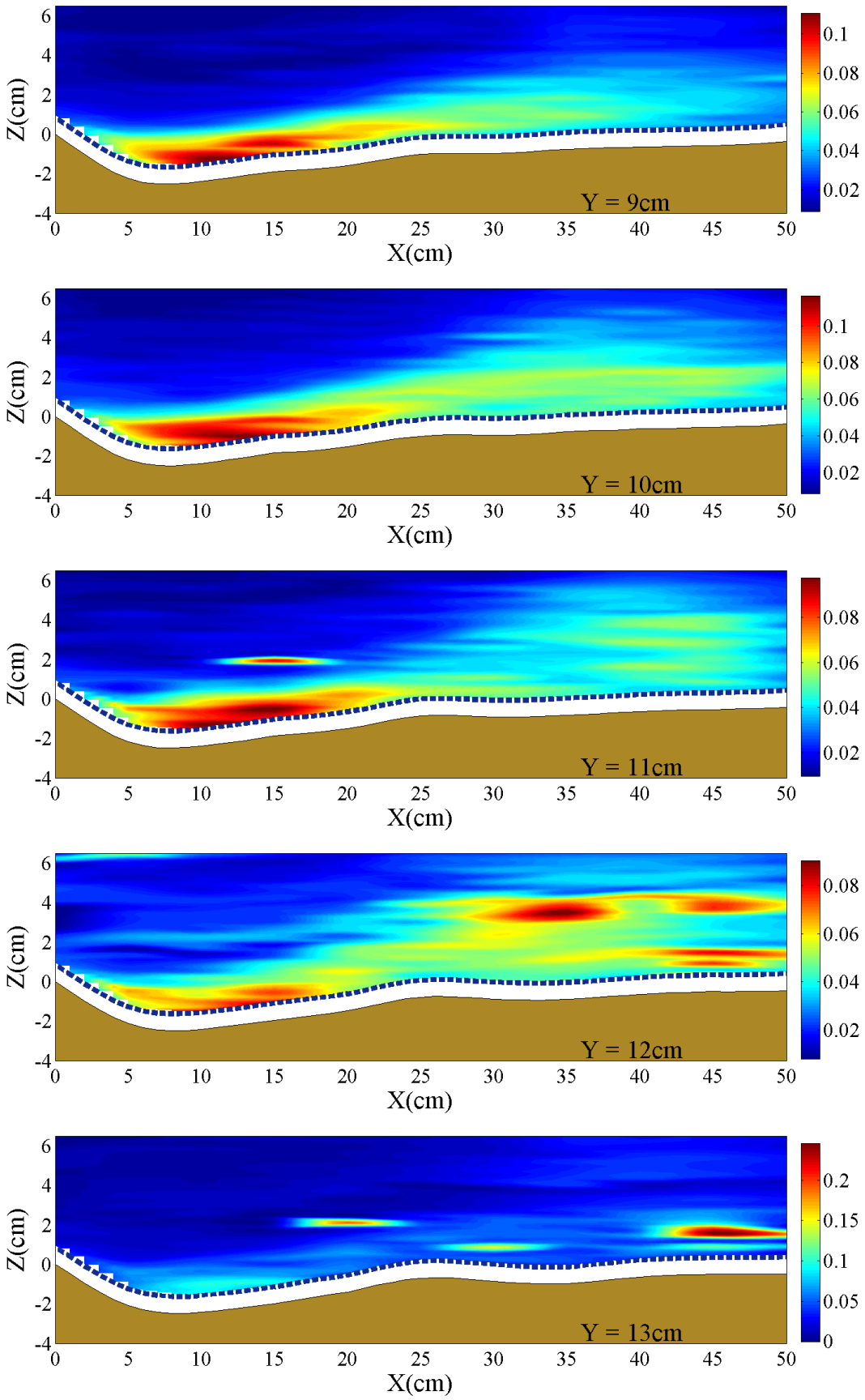

Figure 6.24 – Longitudinal contour maps of K' (m^2/s^2): b) 9cm < Y < 13cm.

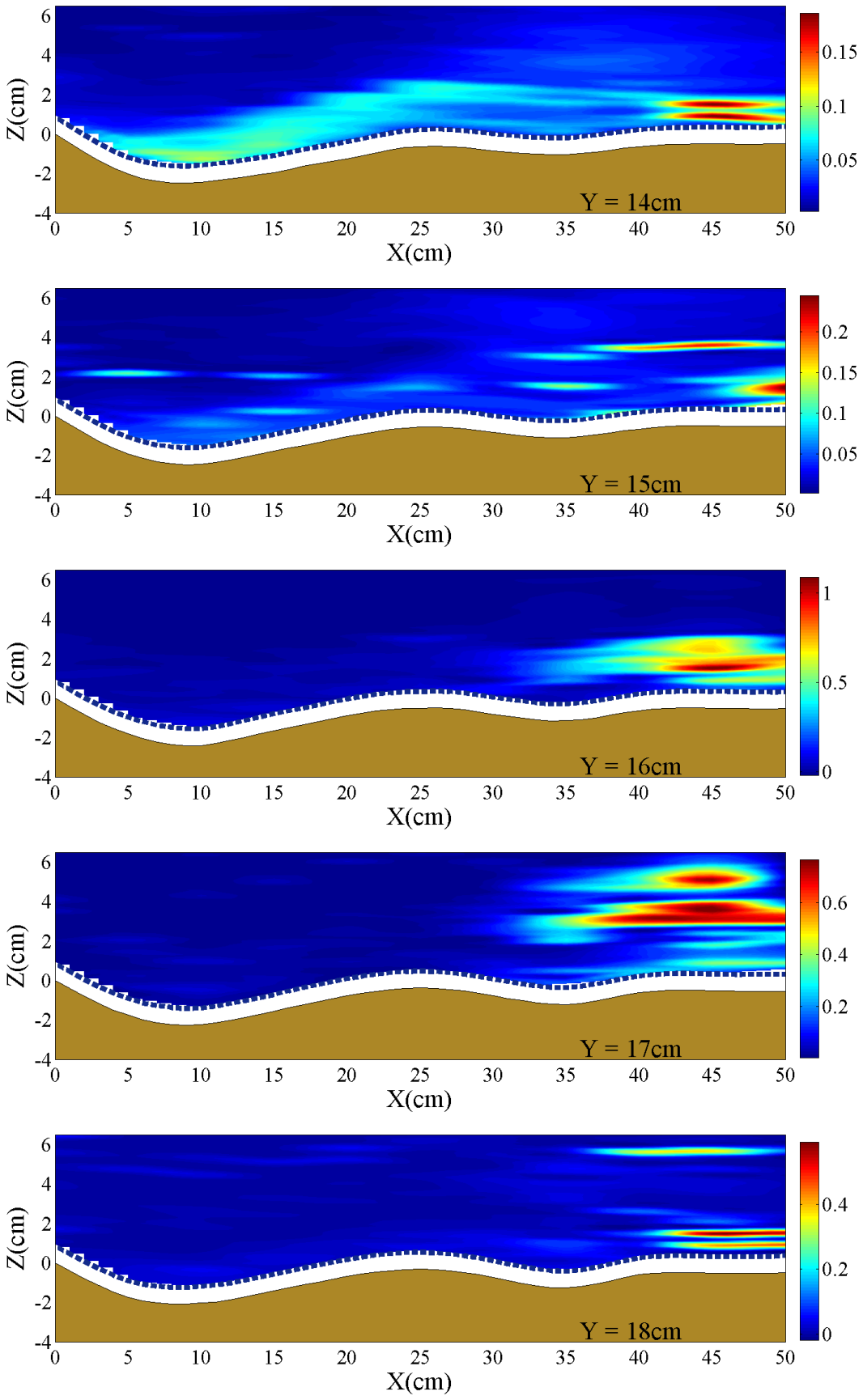

Figure 6.24 – Longitudinal contour maps of K' (m^2/s^2): c) 14cm < Y < 18cm.

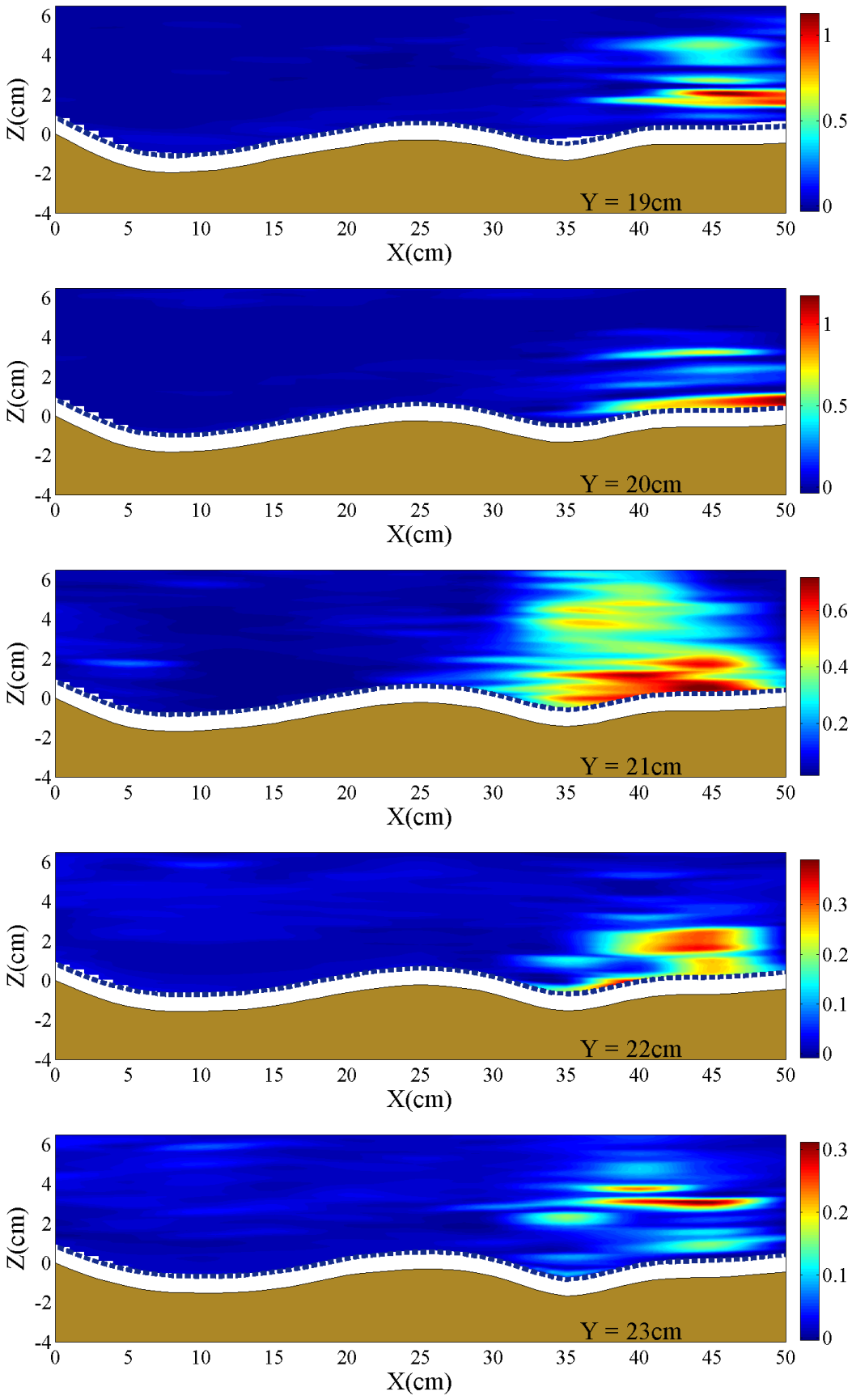

Figure 6.24 – Longitudinal contour maps of K' (m^2/s^2): d) 19cm < Y < 23cm.

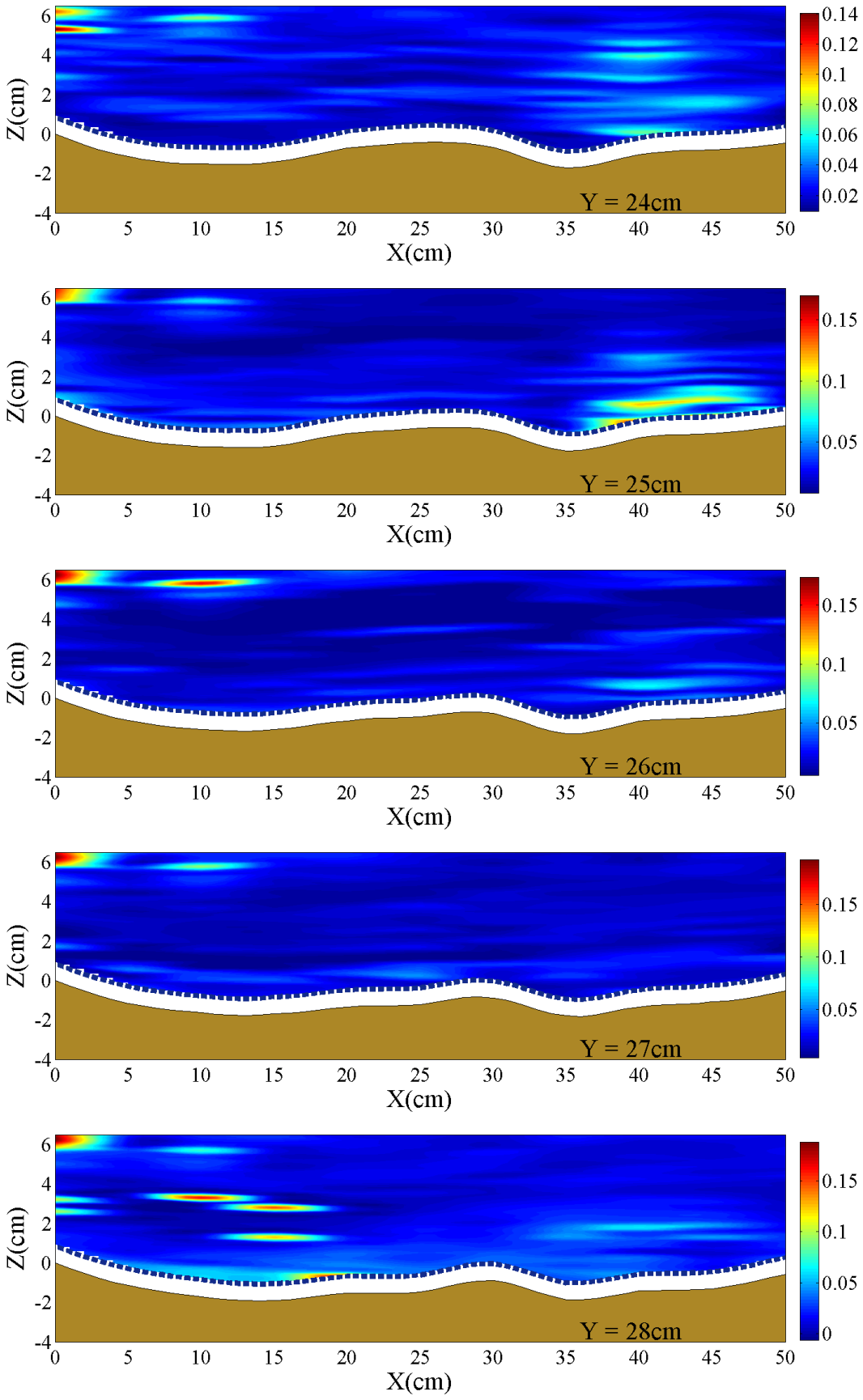

Figure 6.24 – Longitudinal contour maps of K' (m^2/s^2): e) 24cm < Y < 28cm.

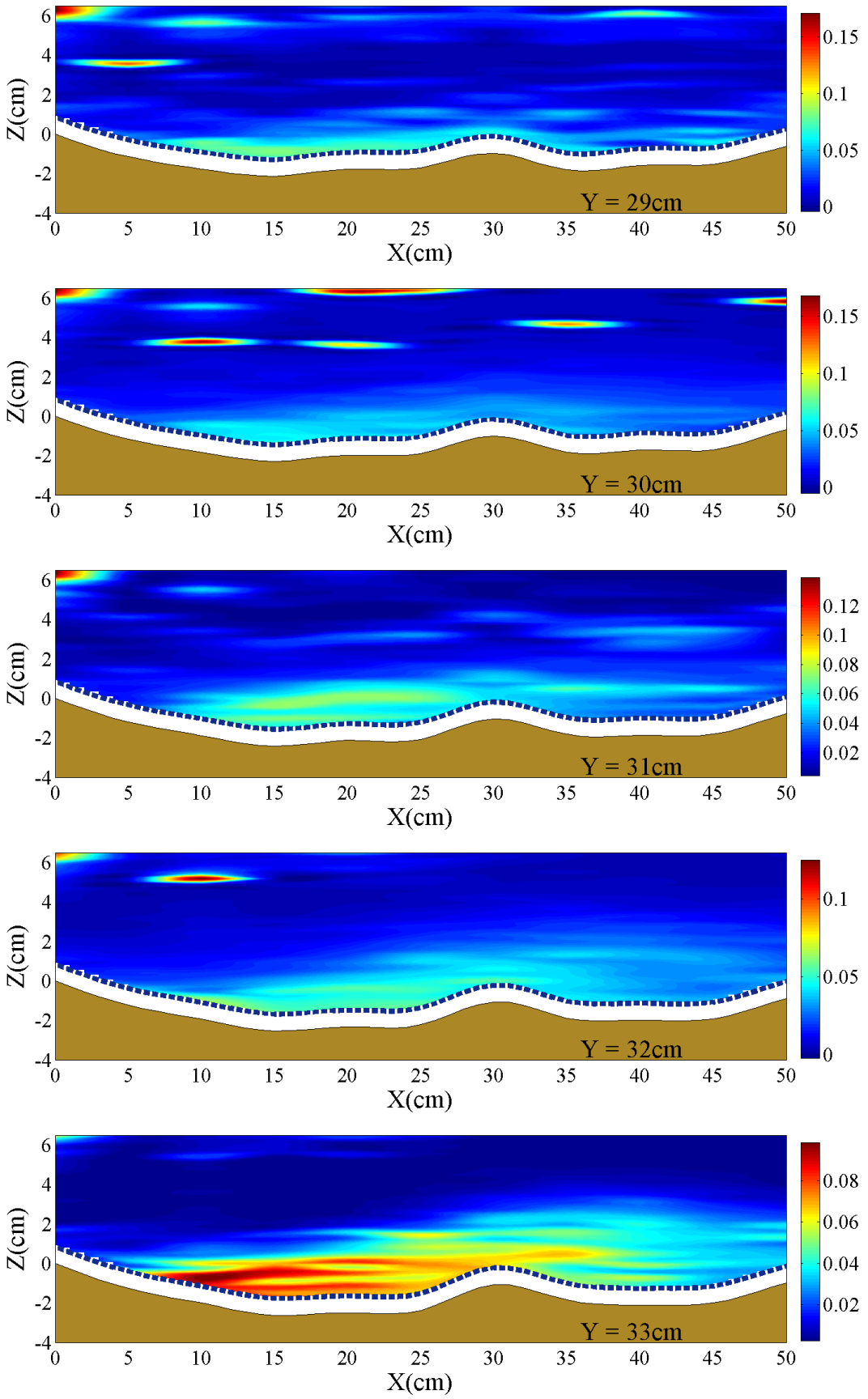

Figure 6.24 – Longitudinal contour maps of K' (m^2/s^2): f) 29cm < Y < 33cm.

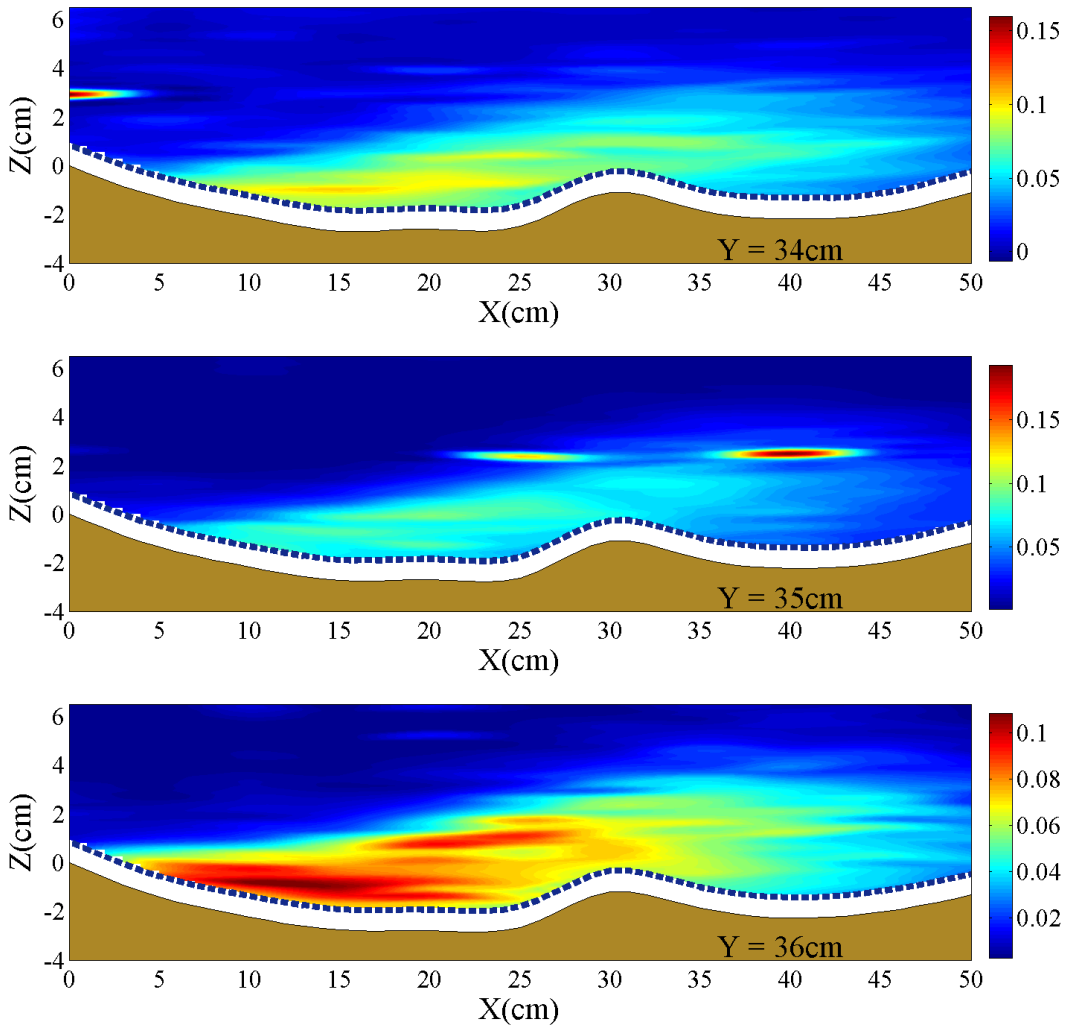

Figure 6.24 – Longitudinal contour maps of K' (m^2/s^2): g) 34cm < Y < 36cm.